

UNIVERSITÄT
BAYREUTH

DOCTORAL THESIS

Surface-Groundwater Interactions and Climate Change Impacts

An Integrated Approach using HydroGeoSphere Model

Muhammad Usman Munir

Faculty of Biology, Chemistry and Geosciences
University of Bayreuth

Bayreuth, 2025

Surface-Groundwater Interactions and Climate Change Impacts

An Integrated Approach using HydroGeoSphere Model

DISSERTATION

zur Erlangung des akademischen Grades eines Doktors der Naturwissenschaften

(Dr. rer. nat.)

an der Fakultät für Biologie, Chemie und Geowissenschaften

der Universität Bayreuth

Vorgelegt von

Muhammad Usman Munir

geboren in Vehari, Pakistan

Bayreuth, 2025

This doctoral thesis was written in the period from Nov 2018 until May 2025 in Bayreuth at the Department of Hydrology under the supervision of PD Dr. Sven Frei.

This is a full reprint of the dissertation submitted to obtain the academic degree of Doctor of Natural Sciences (Dr. rer. nat.) and approved by the Faculty of Biology, Chemistry and Geosciences of the University of Bayreuth.

Form of the thesis: cumulative thesis
Date of submission: 01.07.2025
Date of defence: 18.12.2025

Acting Dean: Prof. Dr. Markus Retsch

Doctoral committee:
PD Dr. Sven Frei (reviewer)
Prof. Dr. Jan Fleckenstein (reviewer)
Prof. Dr. Cyrus Samimi (chairman)
Prof. Dr. Efstathios Diamantopoulos

Dedicated to my beloved parents, my mother and father, whose endless love and unwavering support have made this journey possible.

Abstract

Hydrological connectivity between surface water and groundwater supports the resilience of headwater stream networks, yet this connectivity is increasingly threatened by climate-driven shifts in water availability. This cumulative thesis investigates how environmental change alters surface–groundwater exchange, combining fully integrated numerical modelling with field-based tracer evidence and an innovative data-driven approach. The core study area is the 19.2 km^2 forested Große Ohe catchment in the Bavarian Forest (Germany), whose steep, wetland-fringed headwaters typify many Central European mountain basins; a complementary coastal application extends the analysis to tidally forced systems.

A catchment-scale HydroGeoSphere model was calibrated against observed discharge and then forced with ensembles of RCP-based climate projections. The simulations revealed a pronounced drying trajectory. Mean annual precipitation was projected to decline by 10–20 %, while evapotranspiration remained nearly unchanged, pushing the water balance into persistent deficit. By the late twenty-first century under RCP 8.5, annual deficits increased roughly seven-fold relative to the historical baseline, driving mean streamflow down by up to 34 % and summer baseflow by ~50 %. Falling groundwater heads eroded the hydraulic support that sustains perennial flow: modelled groundwater inputs to upstream reaches contracted by as much as 88 %, and during prolonged dry spells roughly 200 m of the upper channel fell dry, fragmenting the stream network. Thus, even in a humid temperate setting, modest reductions in recharge can trigger a step change from gaining to losing or intermittent conditions.

To examine present-day groundwater influence and its spatial variability, longitudinal surveys of dissolved radon-222 (^{222}Rn) were performed at twelve sites along the headwater tributary on 12 June 2018, 27 September 2018 and 12 June 2019. Measured activities ranged from 83 to 2,888 Bq m^{-3}, with repeated enrichment around HS6–HS7.

Simulated and measured activities were strongly related across sites in all three campaigns (R^2 = 0.86–0.88). Modelled groundwater discharge at HS7 ranged from 25.1 to 30.8 mm d^{-1} on the sampling dates. These results support the location and recurrence of groundwater influence under the sampled low-to-moderate flow conditions. The exact exchange rates remain model estimates, however, because groundwater endmember variability and atmospheric degassing were incompletely constrained. The tracer surveys therefore complement the climate simulations without independently validating future projections.

To test whether a data-driven tool could capture rapid exchange in transient environments, a physics-informed neural network (PINN) was trained on high-resolution sediment-temperature profiles from a sandy tidal creek on the North Sea island of Texel. The network resolved semi-diurnal infiltration/exfiltration cycles with sub-hourly fidelity, reproducing both dominant (M_2) and subsidiary (K_1) tidal components without ancillary hydraulic data. This proof-of-concept underscores the potential of physically constrained machine learning to quantify groundwater fluxes where boundary conditions change too quickly for traditional methods.

Across upland and coastal contexts, the thesis shows that even small climatic or tidal perturbations propagate through the surface–groundwater continuum in a complex way: small shifts in water level redistribute exchange hotspots, modify solute pathways, and ultimately determine whether streams stay flowing or dry up. By combining process-based simulation, natural-tracer monitoring, and next-generation inversion techniques, the work provides a coherent framework for diagnosing and forecasting these dynamics. The results show that headwater wetlands and locations where groundwater enters the stream are key for keeping water flowing; when this groundwater input falls, downstream areas receive less water and shorter habitat corridors. The methods and insights we developed give water-resource managers useful tools to predict, detect, and mitigate hidden but important changes where surface water and groundwater meet.

Zusammenfassung

Die hydrologische Konnektivität zwischen Oberflächen- und Grundwasser stützt die Resilienz von Quellbach-Netzwerken, wird jedoch zunehmend durch klimabedingte Veränderungen der Wasserverfügbarkeit gefährdet. Diese kumulative Arbeit untersucht, wie Umweltänderungen den Austausch zwischen Oberfläche und Grundwasser beeinflussen. Dafür werden voll gekoppeltes numerisches Modelling, feldbasierte Tracer-Messungen und ein innovativer datengetriebener Ansatz kombiniert. Kerngebiet ist das 19,2 km^2 große, bewaldete Einzugsgebiet der Großen Ohe im Bayerischen Wald (Deutschland), dessen steile, moorumsäumte Quellregionen viele mitteleuropäische Gebirgsbecken repräsentieren; eine ergänzende küstennahe Anwendung überträgt die Analyse auf gezeitenbeeinflusste Systeme.

Ein HydroGeoSphere-Modell auf Einzugsgebietsebene wurde gegen gemessene Abflüsse kalibriert und anschließend mit Ensembles klimaprojizierter RCP-Szenarien betrieben. Die Simulationen zeigten einen ausgeprägten Trocknungstrend: Die mittlere Jahresniederschlagsmenge nahm um 10–20 % ab, während die Evapotranspiration nahezu unverändert blieb – dadurch wurde die Wasserbilanz dauerhaft defizitär. Bis zum späten 21. Jahrhundert (RCP 8.5) vergrößerte sich das jährliche Defizit etwa um den Faktor 7 gegenüber der historischen Referenz, wodurch der mittlere Abfluss um bis zu 34 % und die sommerliche Basiswasserführung um ~50 % sanken. Fallende Grundwasserstände schwächten die hydraulische Stütze, die ganzjährigen Durchfluss aufrechterhält: Modellierte Grundwasserzuflüsse zu Oberlaufabschnitten gingen um bis zu 88 % zurück, und in längeren Trockenphasen fielen etwa 200 m des Oberlaufs trocken, was das Bachnetz fragmentierte. Selbst in einem humiden, gemäßigten Klima können also schon moderate Rückgänge der Grundwasserneubildung einen Sprung von gewinnenden zu verlierenden bzw. intermittierenden Bedingungen auslösen.

Zur Untersuchung des gegenwärtigen Grundwassereinflusses und seiner räumlichen Variabilität wurden am 12. Juni 2018, 27. September 2018 und 12. Juni 2019 an zwölf Stellen entlang des Quellbachs Längsprofile der Aktivitätskonzentration von gelöstem Radon-222 (^{222}Rn) aufgenommen. Die gemessenen Aktivitäten lagen zwischen 83 und 2.888 Bq m^{-3}, wobei im Bereich von HS6–HS7 wiederholt erhöhte Werte auftraten. Simulierte und gemessene Aktivitäten waren bei allen drei Kampagnen über die Messstellen hinweg eng korreliert (R^2 = 0,86–0,88). Der modellierte Grundwasserzustrom bei HS7 lag an den Beprobungstagen zwischen 25,1 und 30,8 mm d^{-1}. Diese Ergebnisse stützen die räumliche Lage und das wiederholte Auftreten des Grundwassereinflusses unter den beprobten niedrigen bis mäßigen Abflussbedingungen. Die genauen Austauschraten bleiben jedoch Modellschätzungen, da die räumliche Variabilität des Grundwasser-Endmembers und die atmosphärische Entgasung nur unzureichend bestimmt wurden. Die Traceruntersuchungen ergänzen somit die Klimasimulationen, ohne zukünftige Projektionen unabhängig zu validieren.

Um zu prüfen, ob datengetriebene Werkzeuge schnellen Austausch in transienten Umgebungen erfassen können, wurde ein physics-informed neural network (PINN) mit hochauflösenden Sediment-Temperaturprofilen aus einem sandigen Tidenbach auf der Nordseeinsel Texel trainiert. Das Netzwerk rekonstruierte halbtagestaktige Infiltrations/Exfiltrationszyklen mit substündlicher Genauigkeit und reproduzierte sowohl die dominante M_2- als auch die untergeordnete K_1-Tidenkomponente – ganz ohne zusätzliche hydraulische Randbedingungen. Dieser Proof-of-Concept unterstreicht das Potenzial physikalisch eingeschränkten Machine Learnings, Grundwasserflüsse in Umgebungen zu quantifizieren, in denen sich Randbedingungen zu schnell für traditionelle Methoden ändern.

Über Gebirgs- und Küstenkontexte hinweg zeigt die Arbeit, dass selbst kleine klimatische oder gezeitenbedingte Impulse sich komplex durch das Oberflächen Grundwasser-Kontinuum fortpflanzen: Geringfügige Wasserstandsänderungen verlagern Austausch-

Hot-Spots, verändern Stofftransportwege und entscheiden letztlich, ob Bäche weiterfließen oder trockenfallen. Durch die Kombination von prozessbasierten Simulationen, natürlichen Tracern und inversen Verfahren der nächsten Generation wird ein kohärentes Rahmenwerk zur Diagnose und Prognose dieser Dynamik bereitgestellt. Die Ergebnisse verdeutlichen, dass Quellmoor-Ökosysteme und Grundwassereintrittsstellen entscheidend sind, um den Durchfluss zu sichern; sinken diese Zuflüsse, erhalten stromabwärts gelegene Abschnitte weniger Wasser und kürzere Habitatkorridore. Die entwickelten Methoden und Erkenntnisse liefern Wasserressourcenmanagern praxisnahe Instrumente, um versteckte, aber bedeutende Veränderungen an der Schnittstelle von Oberflächen- und Grundwasser vorherzusagen, zu erkennen und abzumildern.

Acknowledgments

I would first like to express my deepest gratitude to **PD Dr. Sven Frei**. Your steady guidance, incisive feedback, and above all your confidence in my ability to pursue ideas independently shaped every stage of this thesis. When I reached my lowest you reminded me that I could finish; this thesis exists because you stood by me.

My sincere thanks also go to **Prof. Dr. Stefan Peiffer** for fostering an inspiring, welcoming atmosphere in the Department of Hydrology and for offering me the opportunity to join it. I am also grateful to **Dr. Benjamin Gilfedder** for his advice during manuscript preparation.

To the entire Hydrology Department technicians, administrative staff, and fellow researchers, thank you for your daily encouragement, and for ensuring that the coffee machine never stood idle. In particular, I cherish the friendship of my PhD cohort and colleagues and my friends: **Jan-Pascal Boos**, **Laura Wegner**, **Dr. Hassan Elagami**, **Xingyu Liu**, **Karel As**, **Marco La Capra**, **Dr. Johanna Schmidmann**, **Natasha Gariremo**, **Alexey Kuleshov**, **Xiaoqiao Tang**, **Dr. Saeed A. Khan**, **Dr. Faisal Hayat** and **Muhammad Nabeel**. Special thanks to **Katharina Balurock**, whose assistance in the field, made data collection possible, and to **Lisa Kaule**, who guided me through unfamiliar software.

I would also like to thank **Dr. Anees Qamar Abbasi**, **Dr. Muhammad Bilal**, and **Vikram Das** for making my stay in Germany unforgettable. Their support turned these moments into memories I will always cherish, and the experiences we shared enriched this entire journey.

Finally, none of this would have been feasible without the unwavering love of my family. To my parents, my mother and father: thank you for always being just one phone call away despite the thousands of miles between us. To my brothers **Adil** and

Abid, your quiet confidence sustained me. And to **Mariam**, your steady emotional support during the final stretch meant more than words can say.

Contents

Abstract . . . . . **i**

Zusammenfassung . . . . . **iii**

Acknowledgments . . . . . **vii**

List of Figures . . . . . **xiii**

List of Tables . . . . . **xv**

List of Acronyms . . . . . **xvii**

Part I · Overview and Synthesis

1 Extended Summary **3**

1.1 Introduction 3

1.1.1 Interaction between Surface Water and Groundwater . . 4

1.1.2 Importance of Headwater Catchments for Regional Water Availability 6

1.1.3 Climate Change Effects on Hydrological Processes in Headwaters 7

1.1.4 Coastal Aquifers and Submarine Groundwater Discharge 8

1.1.5 Groundwater-Surface Water Interactions: Linking Modeling and Tracers 9

1.2 Hypotheses and Objectives 10

1.3 Methods 12

1.3.1 Study Sites and Experimental Design 12

1.3.2 Hydrological Modeling 14

1.3.3 Transport Modeling 20

1.3.4 Heat Tracer Inversion Using Physics-Informed Neural Networks 22

1.4 Key Findings and Discussion 25
1.4.1 Climate Change Impacts on Surface Water–Groundwater Interactions 25
1.4.2 Groundwater Contributions to Streamflow Revealed by ^{222}Rn Tracing. 27
1.4.3 Using Physics-Informed Neural Networks to Quantify Submarine Groundwater Discharge 30
1.5 Synthesis and Outlook 32
References 37

Part II · Publications and Manuscripts

Declaration of Contributions 45

2 Manuscript 1 47
Understanding the Vulnerability of Surface-Groundwater Interactions to Climate Change: Insights from a Bavarian Forest Headwater Catchment

Abstract 48
2.1 Introduction 48
2.2 Methods 52
2.3 Results 60
2.4 Discussion 70
2.5 Conclusions and Implications 73
References 76
Supplementary Material 82

3 Manuscript 2 83
Runoff Generation and Groundwater Interactions in a Central European Headwater Catchment: Using Process-Based Modelling and Radon-222 as a Natural Tracer

Abstract 85
3.1 Introduction 85
3.2 Materials and Methods 89
3.3 Results 96
3.4 Discussion 101
3.5 Conclusions 108

References 110
Supplementary Material 116

4 Manuscript 3 119
Using Physics-Informed Neural Networks to Quantify Submarine Groundwater Discharge under High-Frequency Tidal Dynamics Using Heat as a Tracer

Abstract 120
4.1 Introduction 120
4.2 Materials and Procedures 125
4.3 Assessment 128
4.4 Discussion 144
4.5 Comments and Recommendations 146
References 148

Part III · Appendix

List of Publications 155

Eidesstattliche Versicherung 157

List of Figures

1.1 Conceptual diagrams of losing (A, B) and gaining (C, D) stream reaches. 5
1.2 Map of the Große Ohe headwater catchment (Bavarian Forest, Germany) and its sub-catchment Hinterer Schachtenbach. 13
1.3 Hinterer Schachtenbach sub-catchment and 222Rn sampling design. . 14
1.4 Flowchart diagram of the hydrological model 17
1.5 Simulated and observed discharge for the calibration and validation . 19

2.1 Topographical map and location of the Grosse Ohe catchment and its sub-catchment Hinterer Schachtenbach, along with the downstream river network. 53
2.2 Model discretization of the A) Grosse Ohe catchment and B) the sub-catchment Hinterer Schachtenbach. 57
2.3 Simulated and observed discharge for the calibration (11/01/2017 – 10/31/2018) and validation (11/01/2004 – 10/31/2017) period. . . . 61
2.4 Mean water balance components for the Hinterer Schachtenbach sub-catchment, presented seasonally for both the near future (2021-2050) and far future (2071-2099), across all Representative Concentration Pathway (RCP) projections. 65
2.5 Seasonally-averaged total exfiltration rates between the groundwater and stream (exfiltration = inflow of groundwater to the stream) for the near and far future simulations and reference period. 66
2.6 Illustrates the projected flux exchange between the stream and aquifer in m/d during baseflow conditions in late summer. 68
2.7 Projected surface water depths for the stream during baseflow conditions in late summer. 69

3.1 Location map of the Grosse Ohe catchment and its sub-catchment Hinterer Schachtenbach. 90
3.2 Simulated and observed river discharge (1 November 2017 – 31 October 2019), with sampling dates also marked. 96
3.3 Longitudinal measured and simulated stream-water ^{222}Rn concentration and modelled streambed exchange flux at HS1–HS12 for (a) 12 June 2018, (b) 27 September 2018 and (c) 12 June 2019. 99
3.4 Modelled daily streambed exchange flux and ^{222}Rn concentration at HS7, together with observed daily precipitation used as model forcing (grey), from 1 November 2017 to 31 October 2019. 101

4.1 PINN architecture using Piecewise-Feedforward Neural Networks with two separate sub-nets to predict the temperature field T(z,t) and the Darcy fluxes q(t). 128
4.2 Training progress for Case Study 1 represented by the loss function and its contributions from λPDE, λGRAD, and λOBS. 132
4.3 Observed temperature timeseries at the observation depths and predicted variations of the Darcy flux in time in comparison to the known reference flux. 133
4.4 Training progress for Case Study 2 represented by the loss function and its contributions from λPDE, λGRAD, and λOBS. 137
4.5 Observed temperature timeseries at the observation depths and predicted variations of the Darcy flux in time in comparison to the known reference flux. 138
4.6 Training progress for Case Study 3 represented by the loss function and its contributions from λPDE, λGRAD, and λOBS. 140
4.7 Measured temperature timeseries at the observation depths and predicted variations of the Darcy flux in time in comparison to the known reference flux. 141
4.8 Power spectra of the tidal level variations observed for the study area and shown in Fig. 4.7. 142
4.9 Power spectra of the Darcy fluxes predicted by the PINN for the Texel data set. 143

List of Tables

2.1 Overview of the average annual temperature and total annual precipitation for the applied climate change scenarios. 59
2.2 Average annual components of the water balance of the sub-catchment for the different RCP ensembles and the historical reference period. . 64

3.1 Model parameters for the Grosse Ohe catchment. 95

4.1 Results of the hyperparameter optimization. 130
4.2 Thermal properties, training parameters and data for Case Study 1. 131
4.3 Root Mean Squared Error (RMSE) and Mean Absolute Error (MAE) between estimated and observed Darcy flux. 134
4.4 Thermal properties, training parameters and data for Case Study 2. 135
4.5 Root Mean Squared Error (RMSE) and Mean Absolute Error (MAE) between estimated and observed Darcy flux. 136
4.6 Thermal properties, training parameters and data for Case Study 3. 138

List of Acronyms

^{222}Rn	Radon-222
ADAM	Adaptive moment estimation (optimiser)
AET	Actual evapotranspiration
BC	Boundary condition
BFNP	Bavarian Forest National Park
DEM	Digital elevation model
EKF	Extended Kalman filter
ERTSS	Extended Rauch–Tung–Striebel smoother
FAO	Food and Agriculture Organization of the United Nations
GCM	Global climate model
GPU	Graphics processing unit
HEC	Higher Education Commission of Pakistan
HGS	HydroGeoSphere
IPCC	Intergovernmental Panel on Climate Change
IQR	Interquartile range
L-BFGS-B	Limited-memory Broyden–Fletcher–Goldfarb–Shanno algorithm with bounds
LFU	Bavarian State Office for Environment (Bayerisches Landesamt für Umwelt)
MAE	Mean absolute error
MSE	Mean squared error
NSE	Nash–Sutcliffe efficiency
PBIAS	Percent bias
PDE	Partial differential equation
PET	Potential evapotranspiration
PFNN	Piecewise-feedforward neural network
PINN	Physics-informed neural network
QDM	Quantile delta mapping
RCM	Regional climate model
RCP	Representative Concentration Pathway
RDF	Root distribution function

RMSE	Root mean squared error
SGD	Submarine groundwater discharge
SUTRA	Saturated–Unsaturated Transport model (USGS)
USGS	United States Geological Survey

PART I

Overview and Synthesis

1 Extended Summary

1.1 Introduction

Water resources are critical to sustaining ecosystems, agriculture, and human settlements alike (Baron et al. 2002). As precipitation-driven processes move water across the Earth's surface and subsurface, a network of interconnected compartments, rivers, soils, aquifers, wetlands, lakes, and coastal margins collectively forms the hydrological cycle (Safeeq and Fares 2016). Central to this cycle is hydrological connectivity, which describes the water-mediated linkages between different domains, including surface water, unsaturated zones, groundwater, nearshore, and marine environments (Leibowitz et al. 2018). This connectivity becomes even more apparent when looking at specific ecosystems: headwater streams that flow through forested catchments (Freeman et al. 2007), coastal aquifers that discharge submarine groundwater into the ocean (Douglas and Murgulet 2025), and transitional zones such as wetlands and estuaries, where the mixing of groundwater and surface water fosters unique biogeochemical transformations (Hofmann 2017; Reid et al. 2016).

A key reason for studying these interconnected systems is that global environmental change (climate change, land-use intensification, water extractions, and contamination) can disrupt the water balances that sustain these aquatic environments. For example, in a forested headwater catchment, a shift in precipitation or warming temperatures can reduce groundwater recharge, causing perennial streams to become intermittent (Halloran et al. 2023). Similarly, in coastal zones, sea-level rise and altered precipitation patterns can influence tidal amplitudes, groundwater levels, and ultimately the magnitude of submarine groundwater discharge (SGD)(McKenzie et al. 2021; Taniguchi et al. 2019). Understanding and quantifying these processes, especially the movement of groundwater to/from surface waters, remains a fundamental challenge in hydrology.

1.1.1 Interaction between Surface Water and Groundwater

A clear understanding of how river water interacts with regional groundwater is essential for effective water management and sustainable resource use. These interactions significantly influence ecosystem health, solute transport and the availability. They also affect the availability and quality of water used for household, agricultural, and recreational purposes. Despite their importance groundwater contributions to river systems are often less studied compared to surface water processes (Sophocleous 2002). Streams and aquifers are strongly connected components of the hydrologic cycle involving in two-way exchanges of water and dissolved solutes (Bencala 2011). The intensity and nature of these exchanges are influenced by a complex interplay of meteorological conditions, river dynamics, subsurface hydrology, geological formations, and human activities (Santos et al. 2012; Murgulet et al. 2016; Moosdorf et al. 2021). Nearly all surface water features (e.g., streams, lakes, wetlands, estuaries) interact with groundwater (Winter et al. 1998). Water movement from groundwater into streams or vice versa, creating a continuous hydrological connection between surface and subsurface systems (Gooseff 2010).

This exchange is not constant; it varies spatially along a river and temporally with hydrologic conditions such as precipitation and seasonal changes (Anibas et al. 2016). The hyporheic zone, the interface where stream water and groundwater mix, plays a crucial role in nutrient cycling and water quality as it facilitates biogeochemical reactions during subsurface transit (O'Connor and Harvey 2008; Boulton et al. 1998). Foundational studies have highlighted how both physical factors, such as channel morphology and geologic heterogeneity, and hydrologic drivers govern these exchanges (Valett et al. 1997). For example, Fleckenstein et al. (2006) demonstrated that heterogeneity in alluvial aquifers can cause uneven stream-aquifer exchange patterns and impact low-flow conditions. Likewise, O'Connor and Harvey (2008) showed that the rate and scale of

hyporheic exchanges influence nutrient processing in streams, underscoring that water exchange is as much about solute dynamics as water quantity.

Surface/groundwater interactions are traditionally classified into three categories: gaining, losing, or disconnected streams (Sophocleous 2002). In a gaining stream (effluent condition), groundwater flows upward into the stream, increasing its discharge. This occurs where the hydraulic head in the adjacent aquifer is higher than the stream stage (Banerjee and Ganguly 2023). Gaining reaches typically prevail in humid regions or downstream portions where groundwater recharge from surrounding lands raises the water table. In contrast, a losing stream (influent condition) has a channel above the surrounding water table, so water seeps downward through the streambed, recharging the aquifer. Such reaches are common in arid climates or upper watershed areas; they can induce a net loss of streamflow to groundwater except during high flows (Sophocleous 2002). Figure 1.1C and Figure 1.1D depict the gaining stream scenario in cross-section and plan view, respectively, while Figure 1.1A and Figure 1.1B below illustrates a losing stream.

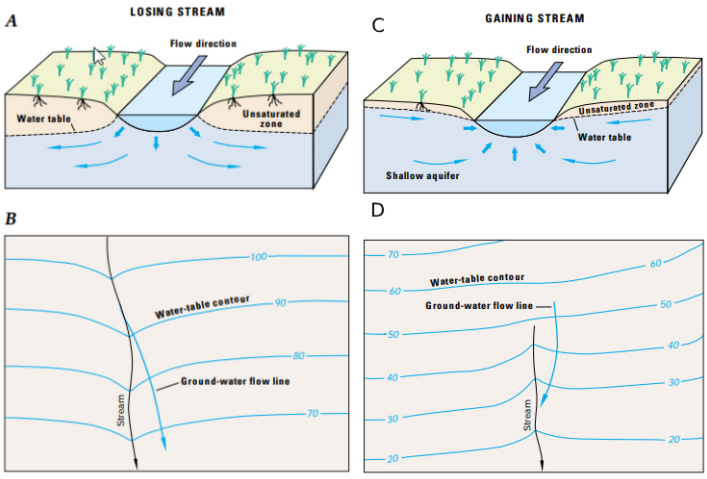


Figure 1.1. Conceptual diagrams of losing (A, B) and gaining (C, D) stream reaches. Gaining streams receive groundwater discharge, with water-table contours forming upstream-facing "V"s. Losing streams lose water to the subsurface, with contours bending downstream

In disconnected streams, the streambed is separated from the phreatic water table by an intervening unsaturated zone. In this case, the stream is essentially perched above the true water table it still loses water, but the percolating water forms a local mound

in the water table that does not connect back to the stream (Brunner et al. 2011). Disconnected conditions often occur when water tables drop substantially (e.g., during prolonged drought or heavy groundwater pumping) such that even baseflow infiltration cannot sustain a connection (Winter et al. 1998).

These three types (gaining, losing-connected, and disconnected) are not fixed states a given river segment can shift from one to another with changing seasons or management. For instance, reaches of a river may gain groundwater in wet seasons but become losing or disconnected as water tables decline in dry months (Brunner et al. 2011). Niswonger and Fogg (2008) showed that low-permeability streambed layers can create perched aquifers that sustain temporary baseflow even as the regional water table drops, a process bridging connected and disconnected conditions.

Groundwater inflows to streams (i.e. baseflow) are hydrologically and ecologically crucial. During rain-free periods, when runoff ceases, groundwater discharge becomes the dominant source of streamflow, maintaining perennial habitats (Barlow and Leake 2012). In gaining streams, this groundwater sustains flow volume, cools stream temperatures, and delivers nutrients and dissolved oxygen that can be vital for aquatic life (Boulton et al. 1998). In losing reaches, stream water percolating into aquifers can recharge groundwater and support down-gradient springs or wetlands (Patten et al. 2008; Nigate et al. 2020).

1.1.2 Importance of Headwater Catchments for Regional Water Availability

Headwater catchments typically first to third-order streams make up roughly 70-90 % of the cumulative length of the global river network (Downing et al. 2012; Wohl 2017). Their small size has a large impact on hydrological role: they intercept precipitation, generate runoff, and deliver water, sediments, nutrients, and organic matter to downstream rivers, lakes, and coastal zones (Biggs et al. 2017). In Central Europe, most headwaters lie within forested, steep terrain underlain by shallow, stony soils that

encourage rapid yet spatially variable ground/surface water exchange (Křeček et al. 2021). During seasonal low-flow periods typically late summer in temperate climates groundwater contributions can rise from $< 20\%$ of daily flow to $> 70\%$ (Kaule and Gilfedder 2021). Such baseflow is necessary for sustaining aquatic habitat connectivity and maintaining suitable water temperatures and dissolved-oxygen concentrations (Choi et al. 2018). Consequently, any changes of recharge, storage, or discharge in headwater aquifers generates throughout the fluvial network, influencing regional water security, biodiversity, and ecosystem service delivery (Biggs et al. 2017).

1.1.3 Climate Change Effects on Hydrological Processes in Headwaters

Projected warming and shifting precipitation regimes pose a particular threat to headwater hydrology. Continental scale modelling shows that, under 1.5-3 °C global warming scenarios, European low flows decline noticeably due to earlier snowmelt, reduced snow storage, and higher evaporative demand (van Vliet et al. 2013; Marx et al. 2018). Regional simulations for Germany indicate that summer drought frequency and duration will intensify over the twenty-first century, driving groundwater levels and baseflows downward especially in the Bavarian Forest and Black Forest (Wunsch et al. 2022; Kaule and Frei 2022). Similar contractions of stream networks have already been observed under recent droughts in the Oregon Cascades (Ward et al. 2020) highlighting the probability of future shifts in temperate Europe.

Reduced summer flows not only jeopardize aquatic biota that depend on permanent cold-water refugia but also impair downstream water quality by amplifying temperature peaks, concentrating nutrients and contaminants, and diminishing dilution capacity (Whitehead et al. 2009). Riparian wetlands, springs, and groundwater-dependent ecosystems are likewise vulnerable; prolonged drawdown can desiccate soils, alter vegetation composition, and reduce carbon sequestration (Dwire et al. 2018). By integrating fine scale hydrological observations with climate-scenario modelling, researchers and wa-

ter managers can better safeguard the ecological integrity and water supply functions of Europe's headwater networks under a changing climate.

1.1.4 Coastal Aquifers and Submarine Groundwater Discharge

Coastal aquifers and their discharge into the ocean mark the downstream terminus of the hydrological continuum, linking terrestrial water cycles to marine ecosystems. Although submarine groundwater discharge (SGD) typically represents only around 0.6–1% of the total global freshwater input to the oceans, it can deliver concentrated pulses of nutrients, trace metals, and organic matter that have outsized ecological effects in nearshore zones (Luijendijk et al. 2020; Zhou et al. 2019). For example, on coral reefs, SGD-borne nitrate and phosphate may alleviate nutrient limitation, supporting coral and algal growth and creating localized "hotspots" of biodiversity (Paytan et al. 2006; Duarte and Cebrián 1996). Conversely, in eutrophication-prone estuaries and lagoons, particularly those adjacent to agricultural or urbanized coastlines, elevated nitrogen loads from SGD can trigger harmful algal blooms, hypoxia, and cascading declines in water quality (Howarth and Marino 2006).

Quantifying SGD fluxes reliably remains a major challenge, especially in tidally influenced settings where tidal pumping drives rapid, bidirectional exchange at sub-daily frequencies. Traditional heat tracer methods, most notably the MATLAB-based VFLUX2 package (Gordon et al. 2012) and the 1DTempPro finite-difference inversion model (Koch et al. 2016), infer vertical water fluxes by analyzing diurnal temperature oscillations in the sediment. While effective under relatively steady conditions, these approaches often smooth out or lag sharp infiltration/exfiltration transitions when fluxes change on timescales shorter than about one tidal cycle (McAliley et al. 2022; LeRoux et al. 2021).

This methodological gap has motivated the interest in physics-informed neural networks (PINNs), which embed the governing heat-transport partial differential equation directly into the training of a neural model (Karniadakis et al. 2021; Raissi et al. 2019).

By coupling data-driven fitting to measured temperature profiles with a PDE-residual loss that enforces the advection–diffusion equation, PINNs can flexibly adapt to arbitrary temporal flux patterns whether abrupt step-changes or multi-frequency tidal signals, without requiring external hydraulic measurements (He and Tartakovsky 2021). Early applications in synthetic and controlled laboratory scenarios have demonstrated that PINNs can recover both diurnal and semidiurnal flux components with negligible phase lag and substantially lower error than classical inversion methods (LeRoux et al. 2021). In the field, PINNs promise to deliver high-resolution, physically consistent estimates of SGD, even in the highly dynamic intertidal zone by leveraging the full spatiotemporal information contained in multi depth temperature time series.

1.1.5 Groundwater-Surface Water Interactions: Linking Modeling and Tracers

Accurate predictions of how climate change will affect small headwater systems or coastal discharge zones hinge on capturing the exchange processes at the interface between surface water and groundwater. Variably saturated flow, heterogeneous geological structures, and localized seepage zones all contribute to the complexity of these interactions, whether in mountainous forests or tidal environments.

Empirical tracers help validate the conceptual and numerical models used to study these processes. Radon-222 (^{222}Rn), for instance, has been widely adopted in freshwater and marine settings to pinpoint and quantify groundwater contributions. In one of the presented studies (Paper 2), ^{222}Rn served as a natural tracer in a Central European headwater stream, verifying model-predicted hotspots of groundwater discharge and strengthening confidence in the model's representation of flow generation mechanisms.

Meanwhile, **heat** is another powerful tracer that has been extensively used to identify bidirectional fluxes across the sediment-water interface. Yet, conventional heat-based inversion methods (e.g., VFLUX, 1DTempPro) can struggle in dynamic environments where fluxes vary sharply over hours or days such as during tidal cycles, flood

pulses, or abrupt hydrological shifts in ephemeral headwater streams. This is where new computational methods, like Physics-Informed Neural Networks (PINNs), come into play. By embedding the governing partial differential equations of heat transport directly into a deep learning framework, PINNs can invert temperature data to estimate fluxes at high temporal resolution under rapidly changing hydraulic conditions. This novel approach is the focus of Paper 3.

1.2 Hypotheses and Objectives

Building on the context above, this thesis is driven by the central hypothesis that climate change will significantly alter surface–groundwater interactions in headwater catchments, leading to reduced groundwater contributions and lower streamflow during critical low-flow periods. This overarching hypothesis can be broken down into more specific conjectures corresponding to each component of the research:

H1 (Climate Change Impacts): In a small forested headwater catchment, projected climate warming and shifts in precipitation will cause decreases in groundwater recharge and storage, resulting in measurably lower baseflows and more frequent streamflow intermittency in summer and autumn compared to historical conditions. We expect pronounced reductions in streamflow and stream network length by the late 21st century under high-emission scenarios, driven by declining precipitation.

H2: Present-day streamflow in the headwater catchment is sustained by spatially variable groundwater inputs, with discrete reaches acting as persistent discharge. These patterns can be reproduced and forecast with a HydroGeoSphere (HGS) model that is rigorously set up and calibrated against our field observations. We expect the HGS-simulated exchange fluxes to correlate positively with ^{222}Rn derived groundwater inflows, confirming both the model setup and ^{222}Rn's value as an indicator of groundwater–surface-water interaction intensity.

H3 (Advancing Flux Estimation Methods): By leveraging physics-informed machine learning, specifically a PINN trained on heat tracer data, it is possible to infer high-

frequency groundwater discharge rates in environments with rapidly varying boundary conditions more accurately than conventional heat-tracing methods. We anticipate that the PINN approach will capture multi-scale tidal signals in flux (both diurnal and semi-diurnal) without the latency and damping issues of traditional analysis, thereby providing new insight into transient flow processes that sustain surface waters.

To address these hypotheses, the research was structured around three primary objectives:

1. **Assess climate change effects on headwater hydrology**: This objective aim to quantify changes in seasonal and annual water availability, identify periods of water deficit or surplus, and evaluate impacts on stream–aquifer exchange (gaining vs. losing conditions) and stream network connectivity (flowing length) in the future relative to historical baseline.

2. **Quantify runoff generation mechanisms and groundwater flux**: This objective includes correlating observed ^{222}Rn activities with modeled exchange fluxes to validate ^{222}Rn as a tracer, verify persistent groundwater discharge zones and their flux rates, and examine how different hydrologic conditions influence groundwater–surface water exchange.

3. **Develop and test a physics-informed neural network for flux estimation**: We applied the PINN to both synthetic scenarios and field data from a tidal creek system. The goal is to demonstrate the PINN's ability to recover high-resolution flux dynamics (infiltration and exfiltration) and to compare its results with those from established analytical models (e.g. VFLUX/1DTempPro) under the same conditions.

By meeting these objectives, the first chapter of this thesis provides a comprehensive synthesis: from future projections of hydrologic change in headwaters, to present-day process understanding via tracers, to methodological advancements for exchange flux

quantification. The ultimate aim is to improve our predictive capability and process-level understanding of surface/groundwater interactions in headwater catchments.

1.3 Methods

1.3.1 Study Sites and Experimental Design

The primary study area is the Große Ohe catchment, a 19.2 km^2 forested headwater basin located in the Bavarian Forest National Park, southeast Germany. This catchment drains towards the Ilz River (a Danube tributary) and ranges in elevation from ~770 m to 1453 m above sea level. The climate is temperate humid, with mean annual precipitation of ~1350–1600 mm and mean discharge around 2.66 mm d^{-1} observed at the outlet gauge (Taferlruck). Geologically, the area is underlain by crystalline rocks (biotite granite and cordierite-sillimanite gneiss), overlain by Cambisol as the dominant soil type with patches of shallow Lithosol and organic Histosols in wetland pockets. Land cover is mainly mixed montane forest (about 70% Norway Spruce) with some high-elevation bogs and a small natural lake (Rachelsee at 1070 m a.s.l.). A sub-catchment of particular interest is the Hinterer Schachtenbach (3.5 km^2), which lies in the upper Große Ohe basin and hosts an instrumented experimental site for groundwater–surface water interaction studies. Figure 1.2 shows the topography of the Große Ohe catchment and the location of the Hinterer Schachtenbach tributary.

For the ^{222}Rn tracer study, sampling and observations focused on the Hinterer Schachtenbach stream, which is roughly 3.5 km in length from its source to the confluence with the main stem. Along this tributary, we established 12 sampling sites (labeled HS1 to HS12, from downstream to upstream) and two monitoring wells (GW1, GW2) in the adjacent aquifer. Figure 1.3 provides a schematic of the sub-catchment and the sampling layout. The sites HS1–HS12 were chosen to capture longitudinal variations in groundwater inflow, particularly across changes in valley slope.

Coastal Tidal Creek; De Slufter, Texel (The Netherlands): To test the PINN approach for heat tracing, field data were collected from a tidal creek known as De Slufter

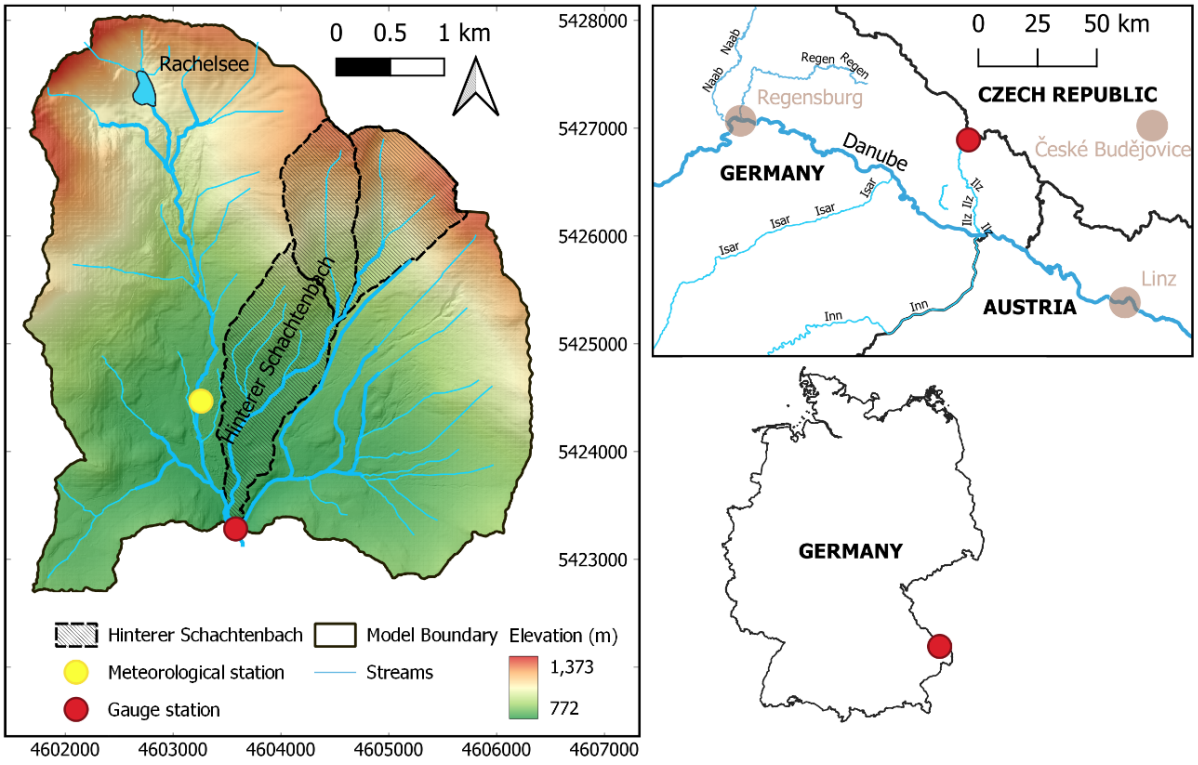


Figure 1.2. Map of the Große Ohe headwater catchment (Bavarian Forest, Germany) and its sub-catchment Hinterer Schachtenbach. Left: Catchment topography (digital elevation model) with stream network (blue lines). The dashed line outlines the Hinterer Schachtenbach ssub-catchment. Yellow circle denotes a meteorological station; the red-bordered circle marks the stream gauging station at the Große Ohe outlet.

on Texel Island. This site is a dynamic coastal lagoon area where seawater tides drive periodic infiltration and exfiltration in creekbed sediments. De Slufter has a sandy creek bed and is part of a nature reserve with both marine and fresh groundwater influences. A 15-day monitoring campaign in June 2024 recorded high-frequency temperature profiles at multiple depths (0 to 0.24 m below bed) in a side channel of the creek. The temperature was measured at 15-minute intervals with precision ~0.003°C. These temperature time series, along with independently measured sediment thermal properties served as input for the PINN model described below. The De Slufter case represents a net losing system overall (marine water pushing into the sediments on flood tides, then draining as tide falls), with complex multi-frequency signals.

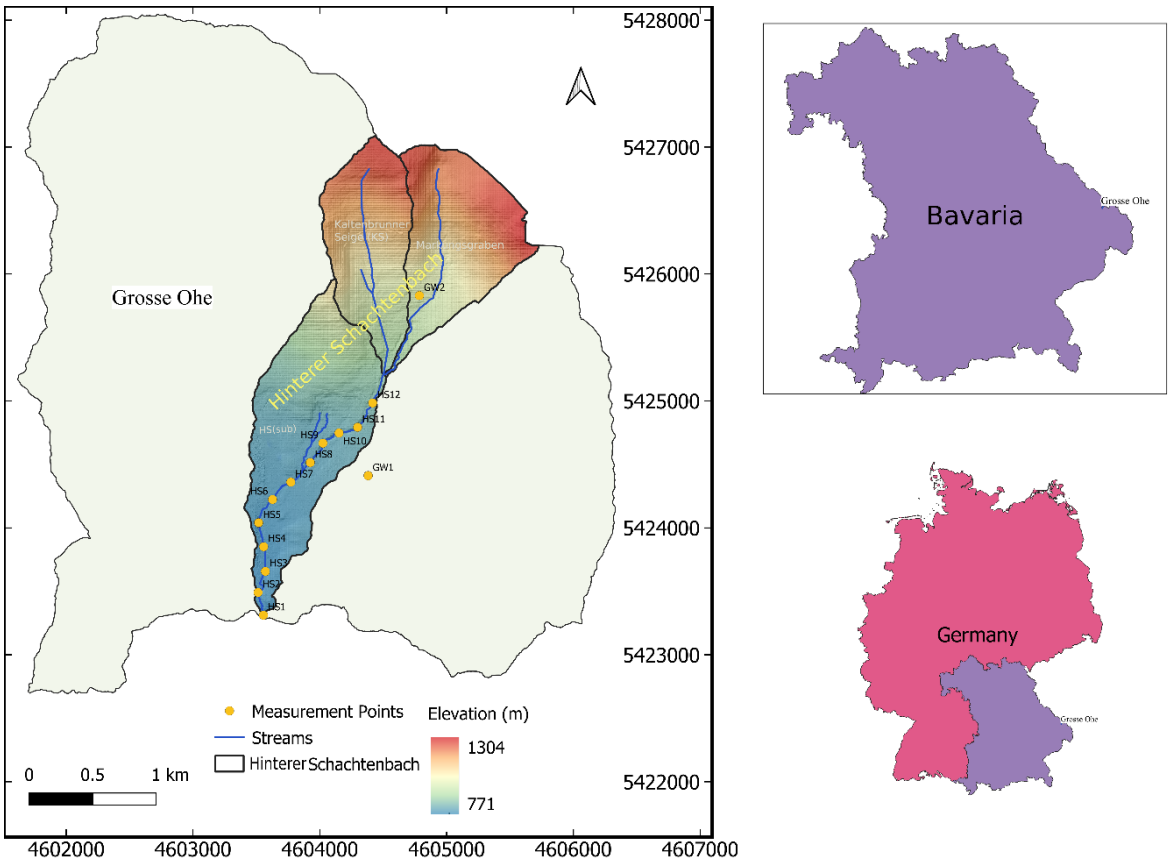


Figure 1.3. Hinterer Schachtenbach sub-catchment and ^{222}Rn sampling design. The stream (blue line) flows ~3.5 km from HS12 (headwaters) to HS1 (outlet). Red circles indicate surface water sampling sites HS1–HS12. Blue circles (GW1, GW2) show groundwater observation wells. Inset map (lower right) situates the sub-catchment within Germany.

1.3.2 Hydrological Modeling

1.3.2.1 HydroGeoSphere Model Setup

We employed the fully-integrated hydrological model HydroGeoSphere (HGS) to simulate 3D variably saturated subsurface flow coupled with 2D surface flow in the study catchments. HGS uses a control volume finite element approach to solve the governing Richards' equation for subsurface water movement and the diffusive-wave approximation of the shallow water equations for surface runoff. The model domain was configured for both the entire Große Ohe catchment (19.2 km^2) and a higher-resolution sub-model for the Hinterer Schachtenbach tributary (3.5 km^2). By nesting these models, we achieved a balance between broader catchment context and fine scale detail in the area of interest.

All major hydrological processes are represented: precipitation and snowmelt inputs, evapotranspiration losses, surface runoff generation, unsaturated-zone flow, groundwater flow, and surface–subsurface interactions. No external routing or baseflow separation schemes are needed, as HGS explicitly simulates exchanges via a dual-node coupling approach (common nodes represent the interface between surface water and groundwater). The model was parameterized with spatially distributed properties derived from soil surveys, geological maps, and literature values, then refined via calibration (Section 1.3.2.4).

1.3.2.2 Mesh Generation and Discretization

We generated an unstructured finite-element mesh for the surface domain using AlgoMesh (HydroAlgorithmics Inc.), which creates Delaunay triangulations optimized for HGS. To improve accuracy in critical zones, we imposed fine discretization along streams and wetlands where surface–groundwater interaction is intense. The final 2D mesh of the entire Große Ohe catchment contains 3399 nodes and 6570 triangular elements. The Hinterer Schachtenbach sub-model, covering the 3.5 km^2 tributary, uses 1824 nodes and 3507 elements in 2D (a somewhat finer spatial resolution within its smaller area). The mesh resolves the 0–3500 m stream length in the subcatchment with increased density of nodes near the channel (element size gradually coarsening with distance from the stream). This allows the model to capture sharp gradients in hydraulic head and soil saturation around the stream margins.

For the subsurface, the 2D mesh was extruded into 3D by layering. We used three principal layers: a 5 m thick topsoil layer, underlain by a 10 m regolith layer and a 10 m deeper bedrock layer. The top 5 m was further subdivided into thin sub-layers of 0.5 m each to better represent the steep moisture gradients in the vadose zone. Thus, the total model depth is ~25 m, encompassing the rooting zone, shallow aquifer, and upper bedrock interface. This discretization yields ~40788 nodes and 78840 elements in the 3D Große Ohe model, and ~21888 nodes/42084 elements in the 3D subcatchment

model. The bedrock base was treated as an impermeable no-flow boundary (consistent with observed low permeability of the granite/gneiss below the regolith).

1.3.2.3 Parameterization and Boundary Conditions

Hydraulic parameters: The model was divided into zones (forest uplands, riparian wetlands, streambed) with distinct hydraulic properties. Initial estimates came from literature and prior studies in similar granite catchments. Saturated hydraulic conductivity K_{sat} is how easily water moves through saturated soil. In riparian wetlands (about 5.6% of the catchment area, characterized by peat and wetlands), we represented the observed sharp decline of permeability with depth by assigning an exponentially decaying K_{sat} profile following the approach of Frei et al. (2010). All such parameters were finetuned during calibration (Section 1.3.2.4); final calibrated values are documented in supplementary Table S2.1 in Chapter 2. Unsaturated soil properties were parameterized with van Genuchten functions and porosity was set to 0.5.

Boundary conditions: No-flow (impermeable) boundary conditions were applied along all lateral extents of the catchment and sub-catchment model, both for surface and subsurface domains, except at the main outlet. The bottom of the model (base of the bedrock layer) was also treated as no-flow, consistent with negligible deep percolation into unmodeled rock. At the outlet, a critical-depth boundary condition was assigned to the surface flow node. This allows water to freely exit the domain when the normal depth condition is met. All lateral and basal faces of the aquifer were left unspecified. In HydroGeoSphere an unspecified exterior face defaults to a zero-normal-flux Neumann condition, so groundwater can exit the subsurface only by crossing the land surface. When simulated heads rise above topography the model's dual-node coupling term transfers water from the porous medium to the overland system within the same nonlinear iteration, where it is then routed to the outlet. This strategy reproduces baseflow without introducing additional calibration parameters at the groundwater boundary and is appropriate for this headwater catchment, whose bedrock forms

a topographically closed basin with no known deep drains. Groundwater outflow was not prescribed with an external Dirichlet boundary. Instead, the land-surface interface was handled internally by HydroGeoSphere's dual-node coupling, which imposes a third-type (Cauchy) boundary where the vertical flux is proportional to the head difference between the saturated zone and the overland water depth. Consequently, when the simulated groundwater head exceeds surface elevation the model automatically produces a positive exchange flux that becomes streamflow; otherwise no flow from ground to surface domain. For initial conditions hydraulic heads at all nodes at t = 0 were imported from the last time step of a year-long spin-up simulation providing an internally consistent late summer water table configuration. Figure 1.4 presents a schematic flowchart of the hydrological modeling framework employed.

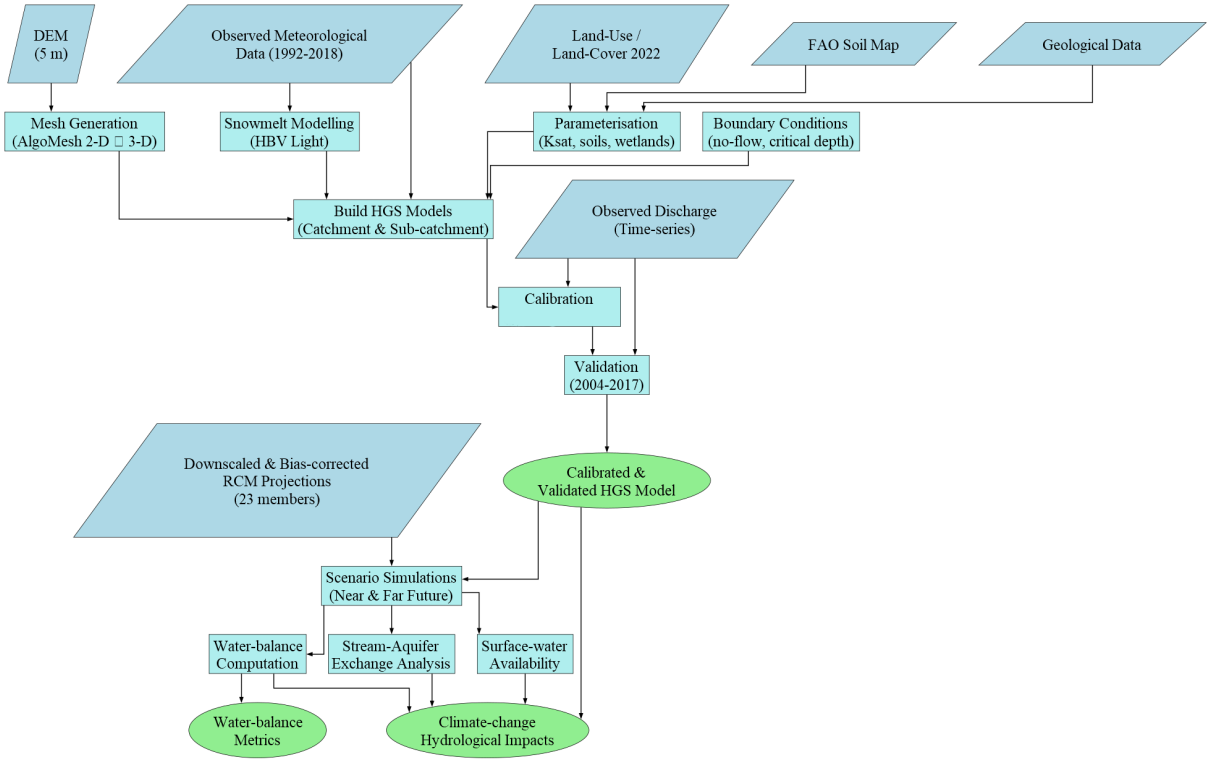


Figure 1.4. Flowchart diagram of the hydrological model

Meteorological forcing: Spatially uniform precipitation was applied over the surface as a flux boundary. We used gauged daily precipitation inputs for the historical calibration period (Section 1.3.2.4) and bias-corrected climate model rainfall for future

scenarios (Section 1.3.2.5). Snow accumulation and melt were accounted for using a degree-day factor approach: a simple snow routine (HBV-light model) was linked to HGS to convert precipitation to snowmelt when temperatures rise above 0°C. This allowed a practical generation of winter runoff from snowmelt, which is important in the study area's climate. Potential evapotranspiration (PET) was calculated outside HGS using the FAO Penman-Monteith equation driven by observed climate data (air temperature, humidity, wind, radiation). The resulting daily PET time series was applied as an upper boundary condition uniformly across the catchment. HGS computes actual evapotranspiration internally based on moisture availability and vegetation cover using the Kristensen and Jensen (1975) model.

1.3.2.4 Calibration and Validation against Streamflow

Model calibration was carried out by manually adjusting parameters to match observed stream discharge at the Große Ohe outlet over a one-year period. Specifically, we calibrated to the hydrological year 2018 (Nov 1, 2017 – Oct 31, 2018) using daily flow data. This year encompassed a range of conditions (winter snowmelt, spring floods, summer low flows) and thus was suitable for parameter tuning. Given the high computational cost of the 3D model, a trial-and-error manual calibration was employed rather than automated optimization. We iteratively adjusted parameters within realistic bounds until an acceptable agreement with the hydrograph was achieved in terms of overall water balance. The fit was evaluated using the Nash–Sutcliffe Efficiency (NSE) and bias metrics. For the calibration year, we obtained NSE = 0.61, indicating a satisfactory match between simulated and observed daily flows. The model reproduces the timing of flow responses, though peak flows were slightly under-estimated and low flows matched closely. Following calibration, we validated the model against an independent multi-year period: 2004–2017. For this validation period, NSE$\approx$0.51, still within an acceptable range for a catchment model of this scale. Nevertheless, overall model performance is comparable to similar studies using integrated models in headwater basins.

The calibrated parameter set thus provides a reasonable starting point to investigate the scenarios and tracer processes of interest.

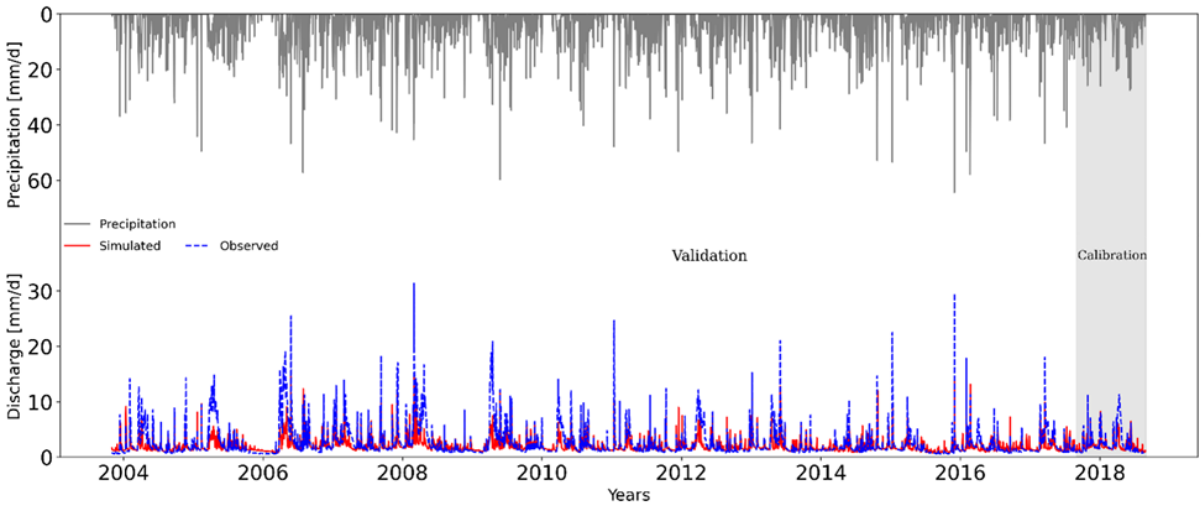


Figure 1.5. Simulated and observed discharge for the calibration and validation

1.3.2.5 Climate Scenario Forcing

To assess climate change impacts, we forced the HGS model with a range of projected climate scenarios. We selected three Representative Concentration Pathways – RCP2.6, RCP4.5, and RCP8.5 representing low, intermediate, and high greenhouse-gas emissions futures, respectively, as defined by IPCC AR5. For each RCP, an ensemble of regional climate model (RCM) outputs was obtained from the EURO-CORDEX and ReKliES-DE downscaling projects. In total, 23 downscaled climate realizations were used (8 members for RCP2.6, 6 for RCP4.5, and 9 for RCP8.5). These RCM simulations provide daily precipitation and temperature (among other variables) at ~5 km resolution over our region. Bias correction was necessary to adjust systematic differences between RCM outputs and local observations (e.g. correcting any tendency to under- or overestimate precipitation). A Quantile Delta Mapping (QDM) approach was used for meteorological parameters. QDM is a widely used bias adjustment method that preserves projected changes in the distribution's quantiles while correcting the baseline biases. We also adjusted potential evapotranspiration accordingly: PET in future scenarios

was recomputed from bias-corrected temperatures and projected radiation/humidity, so that evaporative demand reflects the warmer climate in RCPs.

Each climate scenario was run for two future periods: near-future (2021–2050) and far-future (2071–2099). For baseline comparison, we also ran the model with historical climate (1992–2018) conditions, then driven with each ensemble member's daily sequence for 2021–2050 and 2071–2099. This yields a large set of simulations (23 ensemble members × 3 RCPs × 2 periods, plus baseline) from which we can derive ensemble mean responses and uncertainty ranges. Notably, using the full ensemble without weighting helps address model uncertainty and avoid biases from any single RCM.

1.3.3 Transport Modeling

1.3.3.1 ^{222}Rn as a Natural Tracer

Radon-222 (^{222}Rn) is a radioactive gas with a short half-life of about 3.8 days. It naturally forms in groundwater from the breakdown of uranium in subsurface. As surface water moves underground, it picks up more ^{222}Rn because it comes from the decay of another substance, ^{226}Ra, found in aquifer. How much ^{222}Rn is made depends on parameters like how much ^{226}Ra is in the rocks, where it's located, the size of the rock surfaces, and how water flows through the spaces between grains. In surface water like rivers or lakes, ^{222}Rn levels are usually low because it escapes into the air. But where groundwater flows into a river, ^{222}Rn levels in the river can rise. Underground, ^{222}Rn builds up until it reaches a balance where it's production and decaying at the same rate, this is called steady-state or "endmember activity." This steady-state concentration $E_{q,Rn}$ is determined by the ratio of the aquifer's ^{222}Rn production γ_{Rn}[$T^{-2}L^{-3}$] to the decay constant λ_{Rn} [T^{-1}]of ^{222}Rn:

$$E_{q,Rn} = \frac{\gamma_{Rn}}{\lambda_{Rn}} \tag{1}$$

After about 15 to 20 days, groundwater is said to be in "secular equilibrium," meaning it has stable ^{222}Rn levels. Because of these patterns, ^{222}Rn is very useful for tracking where and how much groundwater is mixing with surface water, which is important in to investigate surface/groundwater interactions.

1.3.3.2 Field Sampling Campaigns

To investigate groundwater surface water exchange using ^{222}Rn as a tracer, we conducted three field sampling campaigns in the Hinterer Schachtenbach catchment: one in early summer June 2018, one at the end of dry season September 2018, and one in early summer June 2019. These campaigns were timed to capture contrasting hydrological conditions, June 2018 following spring rains (higher streamflow), September 2018 during extended baseflow with low stream discharge, and June 2019 after another spring period. Each campaign consisted of longitudinal sampling of stream water for dissolved ^{222}Rn activity. We divided the 3.5 km stream into multiple segments. Overall, these campaigns yielded spatial profiles of ^{222}Rn activity under different flow regimes, which serve as empirical evidence of where groundwater is entering or leaving the stream. Surface water samples were collected from the midstream at 12 locations using 1 L bottles. To prevent the degassing of ^{222}Rn, each sample was filled underwater without leaving any headspace. Measurements of ^{222}Rn in these samples were conducted in the field within 6 hours of collection using multiple RAD-7 detectors (Durridge Company Inc.). Prior to measurement, the air circuit of each detector was dried using Drierite to maintain a relative humidity of approximately 5%. Groundwater samples were obtained from two wells, each of which was purged at least three times before sample collection. The samples were collected in 250 mL bottles by filling from the bottom without leaving any headspace.

1.3.3.3 Initial and Boundary Conditions of the ^{222}Rn Transport Model

Initially, the model was employed to accurately represent endmember activity observed in the catchment's aquifer. This was achieved by applying a zero-order source (γ)

boundary condition uniformly across all model elements, representing the emanation of ^{222}Rn from sediments. To establish secular equilibrium within the system, a simulation incorporating long-term average rainfall as input was conducted. The simulation continued until changes in ^{222}Rn concentrations in the subsurface approached zero, thereby confirming equilibrium conditions. In the surface domain, or overland flow, the longitudinal and transverse dispersivities were uniformly set to 100 meters for all simulations, following recommendations by Liggett et al. (2015). This approach aimed to minimize numerical oscillations related to high Peclet numbers, which are common due to elevated surface flow velocities. Conversely, subsurface dispersion simulations utilized the model's default dispersivity values specific to porous media. A decay constant of 0.18 d^{-1} was applied consistently across both surface and subsurface domains, and various calibrated first-order degassing constants were implemented specifically for the surface flow domain. The transport model was calibrated using ^{222}Rn concentrations measured in surface water samples. Calibration involved manually adjusting the first-order degassing constants within the surface flow domain to account for variations influenced by hydrodynamic conditions (laminar versus turbulent flow) and meteorological factors, including wind speed and rainfall. These varying degassing constants were necessary to reflect the spatial and temporal heterogeneity observed in stream conditions. Due to the high computational demands of the catchment-scale model, calibration was performed manually, based initially on surface water ^{222}Rn concentration measurements collected on June 12, 2018. Further simulations utilized additional ^{222}Rn concentration measurements from surface water samples taken in June 2018 and September 2019, validating and refining the calibration and overall model accuracy.

1.3.4 Heat Tracer Inversion Using Physics-Informed Neural Networks

Heat is another natural tracer used to resolve bidirectional water-exchange fluxes at the sediment water interface under rapidly changing hydraulic forcings. A physics-informed

neural network (PINN) is developed to invert the one-dimensional (1-D) heat-transport equation and to recover transient Darcy fluxes from high-resolution temperature time series. Method development and validation proceeded in three stages: (i) synthetic step-function forcing, (ii) synthetic tidal pumping, and (iii) field observations from a tidal creek on Texel Island. Together these stages test the PINN's ability to reproduce (a) sharp, instantaneous transitions in seepage direction and (b) high-frequency (12–24 h) oscillations typical of macro-tidal environments.

1.3.4.1 Governing Heat-Transport Equation

Vertical heat propagation in fully saturated sediments is described by the 1-D advection conduction equation

$$\frac{k_e}{C_s}\frac{\partial^2 T}{\partial z^2} - \frac{C_w}{C_s}\frac{\partial (Tq)}{\partial z} = \frac{\partial T}{\partial t} \tag{2}$$

where T(z,t) [°C] is temperature, z [m] depth, t [s] time, ke [J s^{-1} m^{-1} °C^{-1}] the effective thermal conductivity, Cs [J m^{-3} °C^{-1}] the bulk volumetric heat capacity, Cw [J m^{-3} °C^{-1}] the volumetric heat capacity of water, and q(t) [m s^{-1}] the vertically averaged Darcy velocity (positive downward).

1.3.4.2 Physics-Informed Neural Network

A piece-wise feed-forward PINN was implemented in Python using the DeepXDE library. The network contains two parallel sub-nets that share the same input pair (z,t). The first sub-network has a single output node that predicts the temperature values T(z,t) for the given input coordinates (z,t). The second sub-network also contains of a single output node, which provides the Darcy flux q(z,t) for each time and spatial coordinate. Both networks are initialized using Glorot Uniform initialization.

1.3.4.3 Composite Loss Function and Optimization

Training minimizes the weighted sum

$$L_{TOTAL} = \lambda_{PDE} L_{PDE} + \lambda_{OBS} L_{OBS} + \lambda_{GRAD} L_{GRAD} \quad (3)$$

LPDE measures how closely the predicted temperature field satisfies the 1-D heat-transport equation at Nr interior collocation points; first and second-order derivatives are evaluated with automatic differentiation. LOBS quantifies how well the predicted temperature field matches observed data, incorporating boundary, initial conditions and observations. LGRAD ensures that the predicted Darcy fluxes q(t) depend only on time. The weighting factors for the individual loss functions:

λ_{PDE}=1, λ_{GRAD}=1, λ_{OBS}=100

1.3.4.4 Application Examples

The PINN framework was demonstrated through three cases: (1) a synthetic scenario by McAliley et al. (2022) with abrupt step-changes in Darcy fluxes to test rapid shifts in hydrological forcings; (2) a synthetic tidal-influenced scenario by LeRoux et al. (2021) assessing the framework's ability to handle high-frequency flux variations; and (3) a real-world tidal creek scenario using field temperature data to demonstrate applicability under realistic conditions. All cases were executed on an NVIDIA A100 GPU via Colab's cloud computing platform, highlighting efficient and scalable cloud-based training.

1.3.4.4.1 Synthetic Step-Function

A 10-day domain combined diurnal (5 °C) and weekly (3 °C) surface temperature oscillations with a 0.3 °C d^{-1} warming trend. Darcy flux was forced through four instantaneous step changes ranging from -0.42 m d^{-1} (discharge) to +0.84 m d^{-1} (infiltration). Temperature records at seven depths (0-1.22 m) were used for inversion. The trained PINN reproduced each step within minutes of occurrence and yielded an RMSE of 0.08 m d^{-1} relative to the synthetic truth. Performance equaled or exceeded an extended Kalman filter benchmark while avoiding explicit covariance tuning.

1.3.4.4.2 Synthetic Tidal Pumping

The tidal pumping scenario is based on a synthetic dataset published in LeRoux et al. (2021). Using the SUTRA groundwater simulator, a 7.47-day time series of M2 (12.25 h) tidal pumping with amplitudes of 2.5 m water level and –0.52 to +0.35 m d^{-1} flux was generated. Eight thermistors (0–0.50 m) sampled every 14 min. After 3.5 $\times$ 10^6 ADAM and 104 L-BFGS iterations the PINN reproduced the tidal waveform with mean-squared flux error of 0.06 m d^{-1}, correctly resolving phase and amplitude of successive tides using temperature data alone.

1.3.4.4.3 Field Application: De Slufter Tidal Creek, Texel

The third case study utilizes an unpublished temperature time series obtained from the tidal creek system 'De Slufter' on Texel, a barrier island off the coast of the Netherlands. Temperature measurements were conducted in a small side branch of the tidal creek over 15 days in June 2024, employing a temperature lance equipped with thermistors positioned at depths of z = 0.00, 0.04, 0.08, 0.12, 0.16, 0.20, and 0.24 m. Measurements were recorded every 15 minutes with a precision estimated at 0.003 °C. Additionally, thermal properties of the water-saturated sediments were determined in the laboratory from soil samples extracted at the study site. The PINN model was trained using a hybrid optimization strategy, comprising 3.5×10^6 iterations with the ADAM optimizer followed by 12 fine-tuning iterations using the L-BFGS-B algorithm. Consistent with previous cases, the initial total loss (L_{TOTAL}) was predominantly driven by the observation loss (L_{OBS}), reflecting discrepancies between predicted and observed temperatures.

1.4 Key Findings and Discussion

1.4.1 Climate Change Impacts on Surface Water–Groundwater Interactions

The first study examined how regional climate change may alter the balance between surface water and groundwater in a small forested headwater catchment. Annual water deficits (net negative storage change in the catchment) are projected to increase

dramatically, on the order of four to seven times higher than the historical baseline, indicating a severe reduction in available water. This drying trend is driven primarily by *decreases in precipitation inputs* (up to ∼–22% in mean annual precipitation under the most extreme scenario) while mean evapotranspiration remains roughly unchanged relative to the past. In essence, significantly less rain and snow are expected to replenish the catchment, yet plant water use does not drop commensurately, resulting in a pronounced water shortfall.

A direct consequence of these prolonged deficits is a decline in groundwater storage within the catchment. With diminished subsurface reserves, groundwater contributions to streamflow (baseflow) weaken, which in turn leads to markedly lower surface flow in the stream. Model results indicate that mean annual stream discharge could decrease by approximately 8–34% compared to present-day conditions, depending on the emission scenario, with larger reductions under higher warming pathways. Crucially, the greatest streamflow reductions are projected during late summer and early autumn, periods that historically rely on baseflow, reflecting the fact that groundwater will be less able to sustain the stream during dry seasons. The spatial pattern of stream–aquifer exchange is also altered. Under reference climate conditions, most reaches of the headwater stream are simulated as gaining reaches fed by groundwater, ensuring year-round flow continuity, with only minor localized losing sections due to topographic breaks. In the future scenarios, all reaches experience diminished exchange fluxes, and the uppermost stream sections become particularly vulnerable. Upstream headwater reaches that are currently perennial are predicted to run dry intermittently in summer as their connection to the aquifer is lost. In the far-future RCP 8.5 scenario, for example, the stream network length could shrink by on the order of 200 m during summer low-flow periods as the highest-elevation channels dry out. This represents a substantial contraction of the flowing stream habitat in the catchment. Notably, even

reaches that remain gaining are expected to receive much smaller groundwater inflows than at present, compounding the overall reduction in surface water availability.

These changes indicate that surface/groundwater interactions in the headwaters are highly sensitive to climate-driven moisture deficits. Less recharge from precipitation means lower water tables and weaker baseflow to streams, pushing the system toward disconnection especially at its headwater extremes. The seasonal timing of these effects in the mid/late summer through autumn coincides with when ecosystems are already stressed by heat and low water, which potentially makes the ecological impacts worse. The study's findings suggest that under future climate scenarios te headwater catchment will experience more frequent or prolonged periods of zero-flow in its upper reaches, a condition rarely observed historically. Such intermittent flow could degrade aquatic and riparian habitats that depend on perennial groundwater input. These results underscore the tight linkage between climate, groundwater recharge, and surface water availability, highlighting that future hydroclimatic shifts could fundamentally weaken the connectivity between aquifers and streams in such mountain headwaters.

1.4.2 Groundwater Contributions to Streamflow Revealed by ^{222}Rn Tracing

The second study focused on quantifying how groundwater feeds into streamflow under current conditions, using a natural tracer ^{222}Rn in conjunction with a process-based hydrological model. By comparing the simulated and observed ^{222}Rn concentrations at multiple locations along the stream, we could assess the model's realism and infer patterns of groundwater–surface water exchange. Model results closely matched the spatial and temporal variability of observed ^{222}Rn across twelve stream observation sites, demonstrating high reliability (with coefficient of determination R^2 up to (0.86-088) between modeled and measured ^{222}Rn). This strong agreement builds confidence that the model can reliably reproduce the key processes governing ^{222}Rn (and thus water) fluxes in the system. In essence, where the model indicates stronger upward

groundwater flow into the stream, higher ^{222}Rn levels are observed, confirming that ^{222}Rn is a sensitive indicator of groundwater discharge zones.

By leveraging the combined tracer–model approach, the study identified distinct "hotspots" of groundwater inflow along the stream. In particular, stream reaches around HS6 and HS7 consistently exhibited elevated ^{222}Rn activities alongside positive modelled exchange fluxes, a pattern evident across all three surveys. This indicates spatially concentrated groundwater influence, although the available observations do not establish whether a particular topographic break, fracture or spring controls the discharge. For example, at two sampling sites (HS6 and HS7), measured ^{222}Rn activities reached 1,797 and 1,549 Bq m^{-3} on 12 June 2018, and the model indicated corresponding groundwater inflow rates of +12.8 and +30.8 mm d^{-1}. At HS7, measured activities reached 2,888 Bq m^{-3} in September 2018 and 1,678 Bq m^{-3} in June 2019, with modelled exchange fluxes of +25.1 and +27.6 mm d^{-1}, respectively. These repeatedly high ^{222}Rn levels and positive modelled fluxes pinpoint zones where groundwater augmented the stream during the three sampled low-to-moderate flow conditions. In contrast, upstream reaches generally showed much lower ^{222}Rn activities and, in some cases, negative exchange fluxes in the model, meaning those sections were simulated as losing reaches where stream water infiltrates into the subsurface. For instance, site HS11 in the upper catchment had a measured ^{222}Rn activity of 166 Bq m^{-3} and a modelled flux of −3.75 mm d^{-1} on 12 June 2018, consistent with simulated infiltration at that location. These observations support recurring groundwater influence around HS6–HS7, whereas the upstream reaches show more variable exchange patterns that cannot be inferred from radon concentrations alone.

Enhanced ^{222}Rn degassing may help explain the low ^{222}Rn concentrations measured in some stream reaches. For instance, at site HS9 the model simulated positive groundwater fluxes of +24.5, +24.7 and +19.5 mm d^{-1} during the three campaigns, yet the observed ^{222}Rn activities remained lower than those at HS4–HS7. This mismatch may

reflect degassing, upstream transport, mixing, groundwater-source variability or unresolved local flow paths. The model used a higher effective ^{222}Rn degassing constant at HS9 and the other sites within HS8–HS12 (44.82 d^{-1}) than at HS1–HS7 (4.82 d^{-1}). However, these calibrated constants are effective reach parameters rather than direct measurements of atmospheric gas loss, because gas-transfer rates and the hydraulic conditions controlling them were not measured. Accounting for such processes is important; otherwise one might wrongly infer low groundwater input simply from a low ^{222}Rn reading, when groundwater inflow may still be substantial but its tracer signal is reduced by gas exchange or mixing. This finding highlights the value of using a coupled modelling approach to interpret tracer data, while also showing that the available observations cannot fully distinguish between low groundwater input and stronger input whose radon signal has been modified by other processes.

Overall, the ^{222}Rn tracer study provides a spatially resolved picture of groundwater–surface water interactions in the headwater catchment, with quantitative exchange estimates supplied by the model. It supports the conclusion that even in a relatively small mountainous basin, groundwater inputs are heterogeneously distributed, with certain reaches showing consistently stronger groundwater influence. These groundwater "hotspots", identified around HS6–HS7, may be important for sustaining baseflow, especially during dry summer periods when direct rainfall/runoff is limited. The approach—combining in-situ tracer measurements with 3D modelling—proved useful for detecting recurring groundwater-discharge zones and evaluating the simulated spatial pattern of groundwater influence. The results underscore the contribution of groundwater to streamflow in this headwater system, although three discrete surveys cannot establish continuous year-round discharge or independently confirm exact local flux rates. Given the vulnerability of headwater catchments to climatic and land-use changes, understanding these interactions is vital. The tracer-based methodology demonstrated here offers a practical means to monitor spatial patterns of groundwater influence and guide

further measurements, which can improve water balance assessments and help evaluate how changes in groundwater storage may affect surface flows. Additional groundwater endmember samples, direct gas-transfer measurements and independent hydraulic observations would be needed to constrain discharge magnitudes more closely. In summary, this study's findings highlight that the surface water in headwater streams is tightly coupled to groundwater inputs, and maintaining those inputs is essential for the resilience of stream ecosystems and downstream water supply in the face of environmental change.

1.4.3 Using Physics-Informed Neural Networks to Quantify Submarine Groundwater Discharge

The third study shifted the focus from rivers and headwater to a tidally forced coastal setting, exploring groundwater/surface water interactions that oscillate on sub-daily scales and are notoriously hard to quantify. Traditional heat-tracer inversions such as VFLUX, 1DTempPro or Kalman-filter routines smooth or lag sharp transitions, require several days of data before resolving even a daily signal, and remain blind to the semi-diurnal component. To overcome this limitation the study introduced a physics-informed neural network (PINN) that set up the one-dimensional advection–conduction heat equation directly into its loss function. Two coupled subnetworks ingest depth and time: one learns the full spatiotemporal temperature field, the other learns the time-dependent Darcy flux that reconciles those temperatures with the governing physics. Validation against two synthetic benchmarks, a step-change test and a sinusoidal tidal-pumping scenario showed that the PINN recovered the prescribed fluxes without phase lag or numerical smoothing, snapping instantly to abrupt transitions and cleanly separating the diurnal (K1, ~24 h) and semi-diurnal (M2, ~12.4 h) harmonics. In stark contrast, conventional tools blurred the step and needed roughly two and a half days of record before beginning to identify the daily tide, never resolving the sub-daily wave. Armed with this proof, the PINN was applied to a 15-day field record from the tidal

creek "De Slufter" on the barrier island of Texel, the Netherlands. Temperature probes implanted to 24 cm depth captured the full 1 m tidal range, and the network converged after 3.5 million ADAM iterations followed by brief L-BFGS-B refinement; the total loss stabilised at 1.8×10^{-2} with observation misfit well below sensor precision, confirming that the inferred fluxes rest on a robust physical data compromise. The resulting hourly flux series revealed a coherent yet highly dynamic exchange. Over the fortnight the creek behaved as a net losing reach, with marine water infiltrating into the sandy bed; yet within each cycle the direction flipped in tune with stage. During high water, especially the K1 peak, infiltration spikes reached their maxima, forcing saline creek water downward; as the tide receded the gradient weakened or reversed and short exfiltration pulses vented stored pore water back to the creek. These reversals were brief and could not offset the cumulative infiltration, but they vividly illustrate the bidirectional nature of the interface. Spectral analysis of the PINN-derived flux confirmed that both K1 and M2 constituents were captured at the correct amplitudes and phases something no previous temperature based inversion had achieved in situ. When the same data were processed with an extended Kalman-filter approach, the resulting flux record appeared almost flat, lacking any tidal modulation, underscoring the unique resolving power of the PINN. Independent field evidence corroborated the inference: pore-water salinity samples showed marine signatures to about 20 cm depth, consistent with the predicted penetration of creek water during high tides. Integrated over the deployment, cumulative infiltration exceeded exfiltration by roughly thirty per cent, demonstrating that modest net marine inflow can be delivered through a multitude of high frequency pulses whose timing and magnitude were previously invisible. Crucially, the entire analysis required no hydraulic head data and ran in under two hours on a standard GPU, making the method practical for routine deployments. By embedding physical law inside a flexible deep-learning architecture, the study demonstrated that short-period, high-amplitude exchanges step changes, multi-frequency tides, even si-

multaneous diurnal and semi-diurnal drivers can now be resolved in real time rather than averaged out. The resulting picture is one of a coastal interface that alternates between gaining and losing conditions over a few hours, governed by distinct tidal constituents whose influence can finally be disentangled and quantified, a methodological breakthrough with direct implications for nutrient budgets, salinity intrusion and the ecological functioning of coastal aquifers. This capability opens new paths for managing coastal resources and for designing monitoring networks that can respond adaptively to rapidly changing hydrologic conditions.

1.5 Synthesis and Outlook

The studies presented above collectively advance our understanding of how surface and subsurface water systems interact across different environments and scales. Despite focusing on distinct settings a forested headwater catchment under climate change, a mountainous stream analyzed with environmental tracers, and a coastal aquifer influenced by tides they converge on a central theme: surface water and groundwater are intimately connected, and their interplay is dynamic and critically important for hydrological resilience. By examining these interactions under varied conditions, the research highlights common principles as well as unique challenges, offering a more unified perspective of hydrologic processes. One overarching insight is the vital role of groundwater in sustaining surface water flows. In the headwater catchments, groundwater discharge serves as a natural regulator that maintains streamflow during dry periods. Model simulations and ^{222}Rn measurements in the Bavarian Forest streams showed that reaches with strong groundwater influx remained flowing even as precipitation declined, whereas sections with weak groundwater support were prone to drying. Groundwater essentially acts as a buffer, smoothing out climatic variability a fact underscored by observed ^{222}Rn hotspots that pinpoint perennial upwelling zones feeding the stream. Similarly, in the coastal tidal creek, groundwater exchange (both inflow and outflow) was found to modulate water levels and fluxes in the sediment on a daily basis, con-

trolling when and where water emerges to the surface. These findings echo the broader hydrological understanding that groundwater contributions are often the backbone of surface water availability (Winter et al. 1998). When that contribution diminishes, surface systems become far more vulnerable to intermittency and drought. A second key theme is vulnerability under environmental change. The studies collectively illustrate that changes in climate and other external drivers can significantly disrupt the surface–subsurface equilibrium. In the climate change scenario for the headwater catchment, reduced precipitation and shifts in seasonality led to groundwater recharge declines, which in turn caused stream baseflows to drop sharply. By the late 21st century, summer and autumn flows could decrease by one-third or more, and upstream portions of the stream network may cease to flow for months. Such projections align with concerns that warming and prolonged drought will contract river networks and intensify low-flow conditions in many regions (Ward et al. 2020). On shorter timescales, the tracer study demonstrated how even individual storm events or dry spells can momentarily upset the balance: heavy rainfall produced quick pulses of runoff that diluted ^{222}Rn and temporarily overwhelmed groundwater inputs, whereas extended dry conditions allowed ^{222}Rn (and thus groundwater influence) to build up in the stream, reinforcing baseflow dominance. In the coastal context, the results suggest that rising sea levels and altered tidal regimes would likewise shift infiltration/exfiltration patterns in coastal aquifers, potentially enhancing saline intrusion or altering discharge rates. Across all scenarios, the message is that surface–groundwater interactions are sensitive to external pressures, whether gradual (e.g. multi-decade climate trends) or abrupt (e.g. floods or tidal surges). Managing water resources under future conditions will require accounting for these sensitivities for example, anticipating reduced baseflows in headwaters during droughts, or increased groundwater flooding in coastal zones during storm tides. Another significant insight is the importance of examining these interactions at appropriate temporal and spatial scales. Each study targeted a different scale of observation,

from sub-daily fluctuations to multi-decadal trends, yet together they emphasize that hydrologic connectivity drives as a continuum across scales. Short-term processes and long-term outcomes are linked. The high frequency tidal analysis in the coastal study revealed how oscillatory forcing drives continuous exchange between groundwater and surface water on timescales of hours; analogous high-frequency variability exists in terrestrial systems (e.g. diel snowmelt or evapotranspiration cycles), even if less pronounced than tides. Over longer periods, these myriad small exchanges accumulate and manifest as seasonal patterns or climate-driven shifts. The headwater modeling study, for instance, indicated major seasonal redistribution of water (with wetter winters but drier summers), which can be viewed as a long-term integration of many event-scale imbalances. This underscores a key methodological point: to truly understand and predict surface–subsurface interactions, one must integrate information across scales. Traditional measurements (like infrequent stream gauges or monthly groundwater readings) might miss critical transient behavior, whereas high-resolution monitoring (^{222}Rn sampling, temperature sensing) paired with advanced models can capture both the "fast" and "slow" dynamics. Together, these studies urge hydrologists to use multi-scale methods such as models that capture single storms and long-term trends, and sensor networks that track hourly changes as well as seasonal patterns. Crucially, the studies showcase innovative tools and methods that push the boundaries of how we analyze surface and groundwater interactions. The first two investigations employed fully coupled numerical models (e.g. HydroGeoSphere) to simulate the complex physics of water flow through subsurface and stream channels, allowing exploration of scenarios (like future climates) and interpretation of tracer data. The second study combined the natural tracer ^{222}Rn with flow and transport modelling to identify recurring groundwater influence, while showing that stream-water activity is not a direct measure of the local groundwater flux. The third study introduced a cutting-edge PINN approach effectively blending physical laws with machine learning to infer fluxes from temperature observa-

tions with unprecedented temporal detail. Each technique overcame certain limitations of conventional approaches: the integrated model provided spatially distributed insight that simple lumped water-balance models cannot; the ^{222}Rn tracer method detected groundwater pathways invisible to standard streamflow measurements; and the PINN succeeded where classical analytical solutions failed by handling highly dynamic forcing without requiring explicit head gradient data. This methodological diversity under a unifying theme suggests a future direction for hydrological research: combining field observations, tracer evidence, process-based simulation, and data-driven algorithms in complementary ways. By leveraging the strengths of each the realism of physically based models, the sensitivity of tracers, and the adaptability of AI, scientists can obtain a more complete and nuanced picture of hydrologic systems than ever before. Together, the three studies showed that using several methods at once reveals insights none of them could provide on their own. Both the upland and coastal systems exhibited alternating phases of gaining and losing conditions driven by the direction of hydraulic gradients. In the headwater stream, certain segments gained flow from groundwater during base-flow periods, whereas others lost water to the subsurface during dry spells; similarly, the tidal creek alternated between net losing (surface water infiltrating into the aquifer at high tide) and briefly gaining (groundwater discharging at low tide). Thus, despite differences in scale and forcing, the underlying physics of surface/subsurface exchange has commonalities across environments. Techniques proven in one domain can often be adapted to another for example, ^{222}Rn tracing to quantify groundwater inputs has been used in both rivers and coastal aquifers (Burnett et al. 2003), and the PINN approach developed for tidal fluctuations could be applied to riverine flood waves or reservoir releases. Recognizing such parallels encourages a more integrated view of the hydrologic cycle, eroding traditional barriers between “surface water” and “groundwater” studies. From a practical standpoint, the unified insights carry important implications for water resource management and ecosystem health. Headwater catchments like the Bavarian

Forest site are often crucial water sources for downstream communities and sustain unique aquatic ecosystems. The projected reduction in baseflow and contraction of stream networks under climate change raise concerns about water security and habitat connectivity. Low flows concentrate pollutants and raise stream temperatures (Whitehead et al. 2009), degrading water quality, while intermittent flow disrupts aquatic life cycles. Possible adaptation strategies include protecting or restoring wetlands and forest cover to enhance groundwater recharge and bolster baseflows. Coastal aquifers and wetlands likewise regulate near-shore water quality. Submarine groundwater discharge delivers nutrients (and contaminants) to coastal waters so understanding when groundwater enters the ocean (e.g. during specific tide phases or after heavy rain) helps in timing pollution control and nutrient management. The advanced methodologies demonstrated (e.g. PINNs and integrated models) can serve as predictive tools. They enable scenario testing for example, simulating how a 20% drop in summer rainfall might affect baseflows, or how a storm surge might induce groundwater flooding thus guiding proactive adaptation. In summary, these studies reinforce that truly sustainable water management requires treating rivers, aquifers, and coastal waters as an interconnected system. A change in any one part; climate, land use, or sea level echoes through the rest. Careful analysis and new tools let each study explain a different piece of the puzzle, from climate impacts on headwaters to tidal effects on groundwater, while together building a full picture of water connectivity. This integrated perspective is crucial in an era of rapid environmental change: it calls for breaking down disciplinary silos and embracing holistic monitoring and modeling. The combined insights from the heightened vulnerability of headwater streams to the effectiveness of new tracer and machine-learning tools point the way forward for hydrological science and water resource management. By continuously innovating and deepening our understanding of surface/subsurface linkages, we will be better equipped to predict and mitigate the challenges facing global water resources in the 21st century.

References

Anibas, Christian; Schneidewind, Uwe; Vandersteen, Gerd; Joris, Ingeborg; Seuntjens, Piet; Batelaan, Okke (2016): From streambed temperature measurements to spatial-temporal flux quantification: using the LPML method to study groundwater-surface water interaction. In *Hydrol. Process.* 30 (2), pp. 203–216.

Banerjee, Dolon; Ganguly, Sayantan (2023): A Review on the Research Advances in Groundwater–Surface Water Interaction with an Overview of the Phenomenon. In *Water* 15 (8), p. 1552.

Barlow, Paul M.; Leake, Stanley A. (2012): Streamflow depletion by wells–Understanding and managing the effects of groundwater pumping on streamflow. Circular 1376. Reston, VA: U.S. Geological Survey.

Baron, J. S.; Poff, N. L.; Angermeier, P. L.; Dahm, C. N.; Gleick, P. H.; Hairston, N. G. et al. (2002): Meeting ecological and societal needs for freshwater. In *Ecological Applications* 12, pp. 1247–1260.

Bencala, K. E. (2011): Stream–Groundwater Interactions. In Treatise on Water Science, vol. 2: Elsevier, pp. 537–546.

Biggs, J.; von Fumetti, S.; Kelly-Quinn, M. (2017): The importance of small waterbodies for biodiversity and ecosystem services: implications for policy makers. In *Hydrobiologia* 793 (1), pp. 3–39.

Boulton, Andrew J.; Findlay, Stuart; Marmonier, Pierre; Stanley, Emily H.; Valett, H. Maurice (1998): The functional significance of the hyporheic zone in streams and rivers. In *Annual Review of Ecology and Systematics* 29 (1), pp. 59–81.

Brunner, Philip; Cook, Peter G.; Simmons, Craig T. (2011): Disconnected surface water and groundwater: from theory to practice. In *Ground Water* 49 (4), pp. 460–467.

Burnett, William C.; Cable, Jaye E.; Corbett, D. Reide (2003): Radon Tracing of Submarine Groundwater Discharge in Coastal Environments. In M. Taniguchi, K. Wang, T. Gamo (Eds.): Land and Marine Hydrogeology: Elsevier, pp. 25–43.

Choi, Byungwoong; Kang, Hyeongsik; Lee, Woong Hee (2018): Baseflow Contribution to Streamflow and Aquatic Habitats Using Physical Habitat Simulations. In *Water* 10 (10), p. 1304.

Douglas, A. R.; Murgulet, D. (2025): Groundwater-Surface Water Interactions in the Coastal Zone. In P. A. Montagna, A. R. Douglas (Eds.): Freshwater Inflows to Texas Bays and Estuaries. Estuaries of the World: Springer, Cham.

Downing, John A.; Cole, J. J.; Duarte, C. M.; Middelburg, J. J.; Melack, J. M.; Prairie, Y. T. et al. (2012): Global abundance and size distribution of streams and rivers. In *Inland Waters* 2 (4), pp. 229–236.

Duarte, Carlos M.; Cebrián, Just (1996): The fate of marine autotrophic production. In *Limnology and Oceanography* 41 (8), pp. 1758–1766.

Dwire, Kathleen A.; Mellmann-Brown, Sabine; Gurrieri, Joseph T. (2018): Potential effects of climate change on riparian areas, wetlands, and groundwater-dependent ecosystems in the Blue Mountains, Oregon, USA. In *Climate Services* 10, pp. 44–52.

Fleckenstein, Jan H.; Niswonger, Richard G.; Fogg, Graham E. (2006): River-Aquifer Interactions, Geologic Heterogeneity, and Low-Flow Management. In *Groundwater* 44 (6), pp. 837–852.

Freeman, Mary C.; Pringle, Catherine M.; Jackson, C. Rhett (2007): Hydrologic Connectivity and the Contribution of Stream Headwaters to Ecological Integrity at Regional Scales. In *JAWRA Journal of the American Water Resources Association* 43 (1), pp. 5–14.

Frei, S.; Lischeid, G.; Fleckenstein, J. H. (2010): Effects of micro-topography on surface–subsurface exchange and runoff generation in a virtual riparian wetland—A modeling study. In *Advances in Water Resources* 33 (11), pp. 1388–1401.

Gooseff, Michael N. (2010): Defining Hyporheic Zones-Advancing Our Conceptual and Operational Definitions of Where Stream Water and Groundwater Meet. In *Geography Compass* 4 (8), pp. 945–955.

Gordon, Ryan P.; Lautz, Laura K.; Briggs, Martin A.; McKenzie, Jeffrey M. (2012): Automated calculation of vertical pore-water flux from field temperature time series using the VFLUX method and computer program. In *Journal of Hydrology* 420-421, pp. 142–158.

Halloran, Landon J. S.; Millwater, Jeremy; Hunkeler, Daniel; Arnoux, Marie (2023): Climate change impacts on groundwater discharge-dependent streamflow in an alpine headwater catchment. In *Science of The Total Environment* 902, p. 166009.

He, QiZhi; Tartakovsky, Alexandre M. (2021): Physics-Informed Neural Network Method for Forward and Backward Advection-Dispersion Equations. In *Water Resources Research* 57 (7), Article e2020WR029479.

Hofmann, Harald (2017): Understanding connectivity within groundwater systems and between groundwater and rivers.

Howarth, Robert W.; Marino, Roxanne (2006): Nitrogen as the limiting nutrient for eutrophication in coastal marine ecosystems: Evolving views over three decades. In *Limnology and Oceanography* 51 (1part2), pp. 364–376.

Karniadakis, George Em; Kevrekidis, Ioannis G.; Lu, Lu; Perdikaris, Paris; Wang, Sifan; Yang, Liu (2021): Physics-informed machine learning. In *Nature Reviews Physics* 3 (6), pp. 422–440.

Kaule, Lisa; Frei, Sven (2022): Analysis of drought conditions and their impacts in a headwater stream in the Central European lower mountain ranges. In *Regional Environmental Change* 22 (3), p. 82.

Kaule, Robin; Gilfedder, Benjamin S. (2021): Groundwater Dominates Water Fluxes in a Headwater Catchment During Drought. In *Frontiers in Water* 3, p. 706932.

Koch, Franklin W.; Voytek, Emily B.; Day-Lewis, Frederick D.; Healy, Richard; Briggs, Martin A.; Lane, John W.; Werkema, Dale (2016): 1DTempPro V2: New Features for Inferring Groundwater/Surface-Water Exchange. In *Ground Water* 54 (3), pp. 434–439.

Křeček, Josef; Nováková, Jana; Palán, Ladislav; Pažourková, Eva; Stuchlík, Evžen (2021): Role of forests in headwater control with changing environment and society. In *International Soil and Water Conservation Research* 9 (1), pp. 143–157.

Kristensen, K. J.; Jensen, S. E. (1975): A model for estimating actual evapotranspiration from potential evapotranspiration. In *Hydrology Research* 6 (3), pp. 170–188.

Leibowitz, S. G.; Wigington, P. J.; Schofield, K. A.; Alexander, L. C.; Vanderhoof, M. K.; Golden, H. E. (2018): Connectivity of streams and wetlands to downstream waters: An integrated systems framework. In *JAWRA Journal of the American Water Resources Association* 54 (2), pp. 298–322.

LeRoux, N. K.; Kurylyk, B. L.; Briggs, M. A.; Irvine, D. J.; Tamborski, J. J.; Bense, V. F. (2021): Using Heat to Trace Vertical Water Fluxes in Sediment Experiencing Concurrent Tidal Pumping and Groundwater Discharge. In *Water Resources Research* 57 (2), Article e2020WR027904.

Liggett, J. E.; Partington, D.; Frei, S.; Werner, A. D.; Simmons, C. T.; Fleckenstein, J. H. (2015): An exploration of coupled surface–subsurface solute transport in a fully integrated catchment model. In *Journal of Hydrology* 529, pp. 969–979.

Luijendijk, Elco; Gleeson, Tom; Moosdorf, Nils (2020): Fresh groundwater discharge insignificant for the world's oceans but important for coastal ecosystems. In *Nature Communications* 11 (1), p. 1260.

Marx, Andreas; Kumar, Rohini; Thober, Stephan; Rakovec, Oldrich; Wanders, Niko; Zink, Matthias et al. (2018): Climate change alters low flows in Europe under global warming of 1.5, 2, and 3°C. In *Hydrology and Earth System Sciences* 22 (2), pp. 1017–1032.

McAliley, W. Anderson; Day-Lewis, Frederick D.; Rey, David; Briggs, Martin A.; Shapiro, Allen M.; Werkema, Dale (2022): Application of Recursive Estimation to Heat Tracing for Groundwater/Surface-Water Exchange. In *Water Resources Research* 58 (6), Article e2021WR030443.

McKenzie, Tristan; Dulai, Henrietta; Fuleky, Peter (2021): Traditional and novel time-series approaches reveal submarine groundwater discharge dynamics under baseline and extreme event conditions. In *Scientific Reports* 11 (1), p. 22570.

Moosdorf, N.; Böttcher, M. E.; Adyasari, D.; Erkul, E.; Gilfedder, B. S.; Greskowiak, J. et al. (2021): A state-of-the-art perspective on the characterization of subterranean estuaries at the regional scale. In *Frontiers in Earth Science* 9, p. 601293.

Murgulet, Dorina; Murgulet, Valeriu; Spalt, Nicholas; Douglas, Audrey; Hay, Richard G. (2016): Impact of hydrological alterations on river-groundwater exchange and water quality in a semi-arid area: Nueces River, Texas. In *Science of The Total Environment* 572, pp. 595–607.

Nigate, Fenta; van Camp, Marc; Yenehun, Alemu; Belay, Ashebir Sewale; Walraevens, Kristine (2020): Recharge–Discharge Relations of Groundwater in Volcanic Terrain of Semi-Humid Tropical Highlands of Ethiopia: The Case of Infranz Springs, in the Upper Blue Nile. In *Water* 12 (3), p. 853.

Niswonger, Richard G.; Fogg, Graham E. (2008): Influence of perched groundwater on base flow. In *Water Resources Research* 44 (3), Article W03405.

O'Connor, Ben L.; Harvey, Judson W. (2008): Scaling hyporheic exchange and its influence on biogeochemical reactions in aquatic ecosystems. In *Water Resources Research* 44 (12), Article W12423.

Patten, Duncan T.; Rouse, Leigh; Stromberg, Juliet C. (2008): Isolated Spring Wetlands in the Great Basin and Mojave Deserts, USA: Potential Response of Vegetation to Groundwater Withdrawal. In *Environmental Management* 41 (3), pp. 398–413.

Paytan, Adina; Shellenbarger, Gregory G.; Street, Joseph H.; Gonneea, Meagan E.; Davis, Kristen; Young, Megan B.; Moore, Willard S. (2006): Submarine groundwater discharge: An important source of new inorganic nitrogen to coral reef ecosystems. In *Limnology and Oceanography* 51 (1), pp. 343–348.

Raissi, M.; Perdikaris, P.; Karniadakis, G. E. (2019): Physics-informed neural networks: A deep learning framework for solving forward and inverse problems involving nonlinear partial differential equations. In *Journal of Computational Physics* 378, pp. 686–707.

Reid, M. A.; Reid, M. C.; Thoms, M. C. (2016): Ecological significance of hydrological connectivity for wetland plant communities on a dryland floodplain river, MacIntyre River, Australia. In *Aquatic Sciences* 78 (1), pp. 139–158.

Safeeq, M.; Fares, A. (2016): Groundwater and surface water interactions in relation to natural and anthropogenic environmental changes. In A. Fares (Ed.): Emerging Issues in Groundwater Resources: Springer, Cham, pp. 289–326.

Santos, I. R.; Eyre, B. D.; Huettel, M. (2012): The driving forces of porewater and groundwater flow in permeable coastal sediments: a review. In *Estuarine, Coastal and Shelf Science* 98, pp. 1–15.

Sophocleous, Marios (2002): Interactions between groundwater and surface water: the state of the science. In *Hydrogeology Journal* 10 (1), pp. 52–67.

Taniguchi, Makoto; Dulai, Henrietta; Burnett, Kimberly M.; Santos, Isaac R.; Sugimoto, Ryo; Stieglitz, Thomas et al. (2019): Submarine Groundwater Discharge: Updates on Its Measurement Techniques, Geophysical Drivers, Magnitudes, and Effects. In *Frontiers in Environmental Science* 7, p. 141.

Valett, H. M.; Dahm, C. N.; Campana, M. E.; Morrice, J. A.; Baker, M. A.; Fellows, C. S. (1997): Hydrologic Influences on Groundwater-Surface Water Ecotones: Heterogeneity in Nutrient Composition and Retention. In *Journal of the North American Benthological Society* 16 (1), pp. 239–247.

van Vliet, Michelle T. H.; Franssen, Wietse H. P.; Yearsley, John R.; Ludwig, Fulco; Haddeland, Ingjerd; Lettenmaier, Dennis P.; Kabat, Pavel (2013): Global river discharge and water temperature under climate change. In *Global Environmental Change* 23 (2), pp. 450–464.

Ward, Adam S.; Wondzell, Steven M.; Schmadel, Noah M.; Herzog, Skuyler P. (2020): Climate Change Causes River Network Contraction and Disconnection in the H.J. Andrews Experimental Forest, Oregon, USA. In *Frontiers in Water* 2, p. 7.

Whitehead, P. G.; Wilby, R. L.; Battarbee, R. W.; Kernan, M.; Wade, A. J. (2009): A review of the potential impacts of climate change on surface water quality. In *Hydrological Sciences Journal* 54 (1), pp. 101–123.

Winter, Thomas C.; Harvey, Judson W.; Franke, O. Lehn; Alley, William M. (1998): Ground water and surface water: A single resource. Circular 1139. U.S. Geological Survey.

Wohl, Ellen (2017): The significance of small streams. In *Frontiers of Earth Science* 11 (3), pp. 447–456.

Wunsch, Andreas; Liesch, Tanja; Broda, Stefan (2022): Deep learning shows declining groundwater levels in Germany until 2100 due to climate change. In *Nature Communications* 13 (1), p. 1221.

Zhou, YaoQuan; Sawyer, Audrey H.; David, Cédric H.; Famiglietti, James S. (2019): Fresh Submarine Groundwater Discharge to the Near-Global Coast. In *Geophysical Research Letters* 46 (11), pp. 5855–5863.

PART II

Publications and Manuscripts

Declaration of Contributions

Study 1

Title: Understanding the Vulnerability of Surface-Groundwater Interactions to Climate Change: Insights from a Bavarian Forest Headwater Catchment

Status: Published in Environmental Earth Sciences 83, 12 (2024).

https://doi.org/10.1007/s12665-023-11314-2

Authors: **Muhammad Usman Munir**, Katharina Blaurock, Sven Frei

Own Contribution in %:

Conceptualization 80%, data preparation 100%, data analysis 80%, methodology 80%, writing original draft 100%, review and editing 70%, and visualization 100%.

MUM: conceptualization and methodology, model development, data analysis, writing original draft. KB: reviewing and editing; SF: conceptualization, reviewing, and editing, supervision.

Study 2

Title: Runoff Generation and Groundwater Interactions in a Central European Headwater Catchment: Using Process-Based Modelling and Radon-222 as a Natural Tracer

Status: Submitted to the Journal of Hydrology.

Authors: **Muhammad Usman Munir**, Benjamin S. Gilfedder, Sven Frei

Own Contribution in %:

Conceptualization 70%, data preparation 100%, data analysis 100%, methodology 100%, writing original draft 100%, review and editing 70%, and visualization 100%

MUM contributed to the study conception and design, performed material preparation and analysis, and wrote the first draft of the manuscript. BSG contributed to the study conception and design, data collection, and review. SF contributed to the study

conception and design, reviewed manuscript drafts, and provided supervision. MUM, SF, and BSG read and approved the final manuscript.

Study 3

Title: Using Physics-Informed Neural Networks to Quantify Submarine Groundwater Discharge Under High-Frequency Tidal Dynamics using Heat as a Tracer

Status: Published in Limnology and Oceanography: Methods 24, e70015 (2026).

https://doi.org/10.1002/lom3.70015

Authors: Sven Frei, **Muhammad Usman Munir**, A. M. Seiverth, and Benjamin S. Gilfedder

Own Contribution in %:

Conceptualization 10%, data analysis 10%, methodology 50%, review and editing 20%, and visualization 50%

S. Frei developed the model framework and wrote the manuscript. A. M. Seiverth conducted fieldwork to collect the temperature time series used in this study. M. U. Munir contributed to coding the PINN framework in Python. B. S. Gilfedder was the lead scientist for the field campaign and contributed to writing and revising the manuscript.

2 Manuscript I: Understanding the Vulnerability of Surface-Groundwater Interactions to Climate Change: Insights from a Bavarian Forest Headwater Catchment

Outline

Abstract . . . 48
2.1 Introduction . . . 48
2.2 Methods . . . 52
2.2.1 Study Area . . . 52
2.2.2 Hydrological Modelling . . . 54
2.2.3 Model Setup, Parametrization and Boundary Conditions . . . 56
2.2.4 Climate Projections . . . 58
2.3 Results . . . 60
2.3.1 Model Performance . . . 60
2.3.2 Impact of Climate Change on the Water Balance Components . . . 61
2.3.3 Impact of Climate Change on Stream-Aquifer interactions . . . 64
2.4 Discussion . . . 70
2.5 Conclusions and Implications . . . 73
References . . . 76
Supplementary Material . . . 82

Bibliographic Information

Munir, M. U., Blaurock, K., and Frei, S. (2024): Understanding the vulnerability of surface–groundwater interactions to climate change: insights from a Bavarian Forest headwater catchment. *Environmental Earth Sciences*, 83, Article 12.

Article Adaptation

The contents of the original version were slightly modified for inclusion in this dissertation, including adjustments to the numbering of sections, figures, tables, and equations. The published version of this article can be found at https://doi.org/10.1007/s12665-023-11314-2

Abstract

Headwaters play a crucial role in maintaining forest biodiversity by providing unique habitats and are important for the regulation of water temperature and oxygen levels for downstream river networks. Approximately 90% of the total length of streams globally originate from headwaters and these systems are discussed to be especially vulnerable to impacts of climate change. This study uses an integrated hydrological model (HydroGeoSphere) in combination with 23 downscaled ensemble members from representative concentration pathways (RCPs) 2.6, 4.5 and 8.5 to examine how climate change affects water availability in a headwater catchment under baseflow conditions. The simulations consistently predict increasing water deficits in summer and autumn for both the near (2021-2050) and far future (2071-2099). Annual mean water deficits were estimated to be 4 to 7 times higher than historical levels. This is mainly due to a projected reduction in precipitation inputs of up to -22%, while AET rates remain similar to those observed during the historical reference period (1992-2018). The declining groundwater storage reserves within the catchment are expected to result in a significant decline in surface water availability during summer and autumn, with a reduction in mean annual stream discharge by up to 34% compared to the reference period. Due to declining groundwater levels, upstream reaches are predicted to become intermittent in summer leading to a reduction of the total stream flow length by up to 200 m. Findings from this study will enhance our understanding of future water availability in headwater systems, and may aid in the development of effective management strategies for mitigating local impacts of climate change and preserving these vulnerable ecosystems.

2.1 Introduction

Stream-aquifer interactions are characterized by dynamic exchange of water and solutes between the surface and subsurface flow domains. Direction and rate of water exchange controls instream biogeochemical conditions, hyporheic turnover of nutrients, moisture

availability in riparian areas as well as temperature and water availability in riverine systems (Fleckenstein et al., 2006; O'Connor and Harvey, 2008; Niswonger and Fogg, 2008; Frei et al., 2009; Taie Semiromi and Koch, 2020). Traditionally, three different types are used in literature to describe the nature of stream-aquifer interactions: (1) a gaining reach receives water from the aquifer when the instream hydraulic head is lower than that of the adjacent groundwater, (2) a losing reach occurs when the stream loses water to the aquifer due to a higher instream hydraulic head compared to the adjacent groundwater, and (3) a disconnected stream describes the situation where there is no water-saturated connection to the groundwater facilitating high loss rates of stream water to the aquifer. The exchange of water between stream and groundwater can be highly variable in time and space due to the temporal dynamics of river flows and the geologic heterogeneity at the stream-aquifer interface (Conant, 2004; Fleckenstein et al., 2006; Krause et al., 2007; Nyquist et al., 2008; Frei et al., 2009). Because of this high variability, it is often not possible to classify streams as purely gaining or losing (Baldwin and McGuinness, 1963). A stream reach however can be considered as net-gaining if it receives more water from the aquifer than it loses, and net-losing if the opposite is true.

When precipitation inputs are low, inflowing groundwater is often the only source that sustains streamflow under baseflow conditions (Delleur, 1999). During droughts perennial streams maintain continuous surface flow because of groundwater inflow (Misra et al., 2011). Surface water availability during baseflow conditions is essential for preserving aquatic habitats and influencing water quality in rivers and streams (Beatty et al., 2010; Choi et al., 2018). A study conducted in Sweden during winter baseflow conditions showed the importance of groundwater, where inflows scaled non-linearly related to catchment size, ranging from approximately 20% for smaller headwater catchments to 80% for larger sized catchments (Peralta-Tapia et al., 2015). Similarly, Kaule and Gilfedder (2021) highlighted the significance of groundwater in-

flow for headwater catchments in Germany, where the fraction of instream groundwater increased from 10% under normal flow conditions to 70% during baseflow conditions in late summer. For the Upper Colorado River Basin, Miller et al. (2016) found that on average, 56% of river stream water originates from groundwater inflow. The balance between moderate flow conditions, floods, and droughts is crucial for the health of fluvial ecosystems (Richter et al., 1997; Arthington et al., 2006), and dropping groundwater levels can negatively impact ecological processes and biodiversity for these sensitive ecosystems (Choi et al., 2018).

According to IPCC (2014) there is an increase in global temperature and various aquatic ecosystems are at risk of serious impacts due to increasing water temperature and lower water availability. The projections for climate change indicate a significant reduction in the availability of groundwater by the end of the 21st century, leading to significant effects on both global and regional water resources (Atawneh et al., 2021; Wunsch et al., 2022). Recent studies for Central Europe found that climate change is expected to increase the duration and frequency of low flow conditions (Gosling et al., 2017; Marx et al., 2018) with an increase of evapotranspiration rates during summer until 2100 (Chan et al., 2021; Kaule and Frei, 2022). For large areas in Germany it is predicted that climate change will increase the probability of drought conditions due to higher evapotranspiration rates in summer that causes up to 43% annual reduction in the streamflow by 2050 (Huang et al., 2010; Al-Mukhtar et al., 2014). Goderniaux et al. (2009) and Wunsch et al. (2022) found that due to increased evapotranspiration and reduced percolation rates, groundwater storage is also likely to decline as a result of climate change. According to Natkhin et al. (2012) Northeast Germany has already seen a significant reduction in groundwater recharge between 1957 and 2007, primarily as a result of decreased precipitation and increased evapotranspiration rates.

Approximately 90% of the total length of streams globally originate from headwaters (Downing et al., 2012; Allen et al., 2018), making them crucial for downstream

water availability and quality (Alexander et al., 2007). Headwater streams in general are often more dependent on groundwater inputs compared to downstream rivers and streams (Kaule and Gilfedder, 2021). Because of the strong dependency of groundwater inputs and limited groundwater storage reserves, streamflow in headwater catchments is highly sensitive to climate change (Bennett et al., 2012). A shift in precipitation patterns, increasing temperature and less rainfall during dry seasons in summer significantly can impact the water availability in these systems with the potential to also disrupt the connection between headwater catchment and downstream river networks. Bernsteinová et al. (2015) observed that headwater catchments in Central Europe were already experiencing negative flow trends in summer due to an increase in temperature from 1978 to 2011. Kaule and Frei (2022) demonstrated that the water balance of headwater catchments located in the lower mountain ranges of Germany has been and will continue to be significantly affected by climate change, resulting in an increased frequency and intensity of drought events.

Quantification of interactions between surface water bodies (e.g. rivers and streams or lakes) and groundwater on different spatial and temporal scales can be estimated using integrated hydrological modeling frameworks (Frei et al., 2009; Chen et al., 2016). These modelling frameworks offer a comprehensive and integrated view of the hydrological cycle, accounting for interactions and feedbacks between surface and subsurface flow processes. By accounting for the complex dynamics and feedbacks between surface and subsurface water flow, integrated hydrological models enable a more accurate representation of hydrological systems and provide valuable insights into the impacts of human activities and climate change on the water cycle. Surface-groundwater interactions on various scales were intensively studied in the past using integrated hydrological models (e.g., Ala-aho et al., 2017; Chen et al., 2016; Cloutier et al., 2014; Frei et al., 2009; Min et al., 2015) but only a few studies focused on how these interactions are affected by climate change (Goderniaux et al., 2015; Molano-Leno et al., 2018).

As part of this study, our objective is to assess the influence of regional climate change on the water availability in a small headwater catchment located in the Bavarian Forest region of South-East Germany. This catchment can be seen as a representative system for many forested catchments located in the lower mountain ranges of Germany and Central Europe. For this purpose, we used the integrated hydrological model HydroGeoSphere (HGS) to represent hydrological processes in the catchment, including surface and subsurface flow as well as interactions between both flow domains. We utilized Regional Climate Models (RCMs) to predict future precipitation inputs, temperature, and potential evapotranspiration rates. These parameters were integrated into the HGS model to simulate runoff generation processes in the catchment. Specifically, we focused on examining the effects of climate change on instream water availability and exchange of water between the stream and groundwater during baseflow conditions in late summer. We hypothesize that climate change will result in a decrease in groundwater contributions to the stream, particularly during low flow conditions in summer, due to dropping groundwater levels. This hypothesis is based on the expectation that RCMs, with their predicted changes in precipitation, temperature, and actual evapotranspiration rates, will alter the hydrological cycle and decrease the availability of groundwater for streamflow. Results from this study will provide a better understanding on future water availability in headwater systems and might help to develop efficient management strategies to mitigate local effects of climate change and to protect these sensitive ecosystems.

2.2 Methods

2.2.1 Study Area

The Grosse Ohe catchment is situated in the Bavarian Forest National Park in South-East Germany (Figure 2.1). It is the headwater catchment of the Grosse Ohe river, the largest tributary of the river Ilz which joins the Danube river at Passau, Germany. The catchment covers 19.2 km^2 area (mean terrain slope is 7.7^o) and shares its border with

the Czech Republic. Hinterer Schachtenbach having 3.5 km^2 area is the sub-catchment located in the Grosse Ohe catchment. The elevation of the Grosse Ohe catchment stretches from 770 to 1453 m.a.s.l. with a permanent lake (Rachelsee) located at an elevation of 1070 m.a.s.l. in the north of the catchment. The bedrock geology is characterized by two major rock types; biotite granite and ordierite-sillimanite gneiss. The main proportion of the soil consists of cambisol, while lithosol and histosol soil types also can be found in this catchment. Most of the area is covered with natural forest in which Norway Spruce is the dominant species (almost 70%) (Beudert et al., 2015). Annual rainfall in the Grosse Ohe catchment varies from 1350 to 1600 mm yr^{-1} with a mean annual discharge of 2.663 mm/d measured at the Taferlruck gauging station located at the catchments' outlet (Figure 2.1). Based on the climate, the catchment lies in the temperate zone and is affected by atlantic and continental influences (Bässler, 2008).

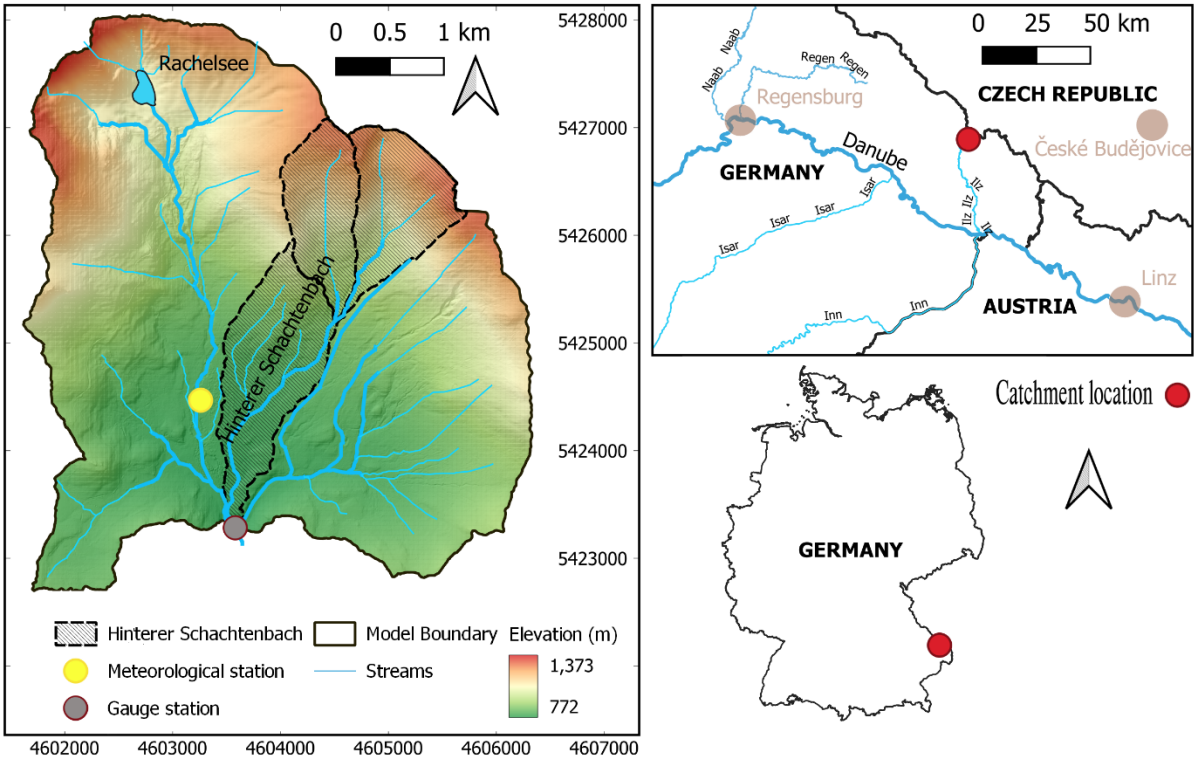


Figure 2.1. Topographical map and location of the Grosse Ohe catchment and its sub-catchment Hinterer Schachtenbach, along with the downstream river network.

2.2.2 Hydrological Modelling

HydroGeoSphere (HGS) is an integrated fully distributed, physical-based hydrological model that simultaneously represents surface and subsurface flow processes as well as interactions between the two flow domains (Therrien et al., 2008, Therrien et al., 2010). A detailed model description along with all governing equations are available in detail in Aquanty Inc. (2015). In HGS, a control-volume finite element scheme is used to solve the governing equations for 3D variably saturated subsurface flow and 2D-depth averaged surface flow. HGS uses the diffusive wave approximation of the Saint-Venant equation for representing 2D-depth averaged surface flow, given as:

$$\frac{\partial \phi_o h_o}{\partial t} - \frac{\partial}{\partial x}\left(d_o K_{ox}\frac{\partial h_o}{\partial x}\right) - \frac{\partial}{\partial y}\left(d_o K_{oy}\frac{\partial h_o}{\partial y}\right) + d_o \Gamma_o \pm Q_o = 0 \tag{1}$$

In equation (1) ϕ_o [-] is the surface flow domain porosity, h_o [L] the surface water elevation, d_o [L] is surface water depth, K_{ox} and K_{oy} are surface conductances [L T^{-1}], Q_o [L T^{-1}] is a volumetric flow rate per unit area representing external source and sinks and Γ_o [L T^{-1}] represents fluid exchanges with the subsurface domain. Variably saturated subsurface flow is represented using the modified form of the 3D Richards' equation, given as:

$$-\nabla.(q) + \sum \Gamma_o \pm Q_{BC} = S_\omega S_s \frac{\partial \psi}{\partial t} + \theta_s \frac{\partial S_\omega}{\partial t} \tag{2}$$

Where q [L T^{-1}] is the Darcy flux, Γ_o [L^3 L^{-3} T^{-1}] is symbolizes the exchange between surface and sub-surface domain, Q_{BC} [L^3 L^{-3} T^{-1}] is a volumetric flux that is associate with a boundary condition. ψ [L] is the hydraulic head, θ_s [-] is the porosity, S_ω and S_s [-] are the saturation and the specific storage coefficient, respectively. Surface and subsurface domains are linked using the dual node approach:

$$d_o \Gamma_o = \omega_m \frac{k_r K_{zz}}{l_{exch}}(h - h_{o)} + \omega_d \frac{k_{dr} K_{dzz}}{l_{exch}}(h_d - h_o) \tag{3}$$

Where, h_o [L] is the surface water head, h and h_d [L] are the subsurface porous media and dual media hydraulic head respectively, k_r and k_{dr} [-] are the relative permeabilities, ω_d [-] is the volumetric fraction of the dual medium, K_{zz} and K_{dzz} [LT^{-1}] are the vertical saturated hydraulic conductivities l_{exch} [L] is a coupling length.

Daily potential evapotranspiration rates were calculated with the FAO Penman-Monteith equation (Allen et al., 1998) based on the climatic available data (e.g. temperature, wind speed, relative humidity, solar radiation). HGS is calculating actual evapotranspiration based on the potential evapotranspiration rates using the method suggested by Kristensen and Jensen (1975). Here actual evapotranspiration is divided into three parts; evaporation from the canopy, transpiration from plants and evaporation from the soil. Root uptake of water (Tr) [LT^{-1}] is calculated using the relationship shown in equation (4).

$$Tr = f_1(LAI)\ f_2(\theta)\ RDF\ (E_p - E_{can}) \tag{4a}$$

$$f_1(LAI) = C_2 + C_1 LAI \tag{4b}$$

$$f_2(\theta) = 1 - \frac{(\theta_{FC} - \theta)^{C_3}}{(\theta_{FC} - \theta_{\omega p})} \tag{4c}$$

Here $f_1(LAI)$ [-] is a function of the Leaf Area Index provided seasonally for each type of vegetation, C_1[-], and C_2[-], and $f_2(\theta)$ [-] is a function of the soil moisture content, Root Distribution Function (RDF) defines the distribution of the roots with depth [-], E_p [LT^{-1}] is the potential evapotranspiration. C_3 [-] is a fitting parameter, $\theta_{\omega p}$ [-] is the moisture content at wilting point, θ_{FC} [-] is the moisture content at field capacity. Finally actual evaporation rates along with transpiration from soil surface and subsurface soil layers is estimated by equation 5**.**

$$E_s = \alpha \left(E_p - E_{can}\right) \left(1 - f_1(LAI) \; EDF\right) \tag{5}$$

Where, α [-] is a wetness factor, E_{can} [LT^{-1}] is the canopy evaporation and EDF [-] is the evaporation density function and is assumed to be effective from soil surface to a given extinction depth.

2.2.3 Model Setup, Parametrization and Boundary Conditions

To achieve the objective of this study, we employed a nested modelling approach using HGS. This involved developing an HGS model for the entire Große Ohe catchment, as well as a separate model for one of its sub-catchments, Hinterer Schachtenbach (Figure 2.2). As long-term discharge data was only available for the entire Große Ohe catchment, the larger model was used for calibration and validation, while the model for the sub-catchment, was used for investigating the impact of climate change on surface/groundwater interactions. Despite maintaining an accurate representation of surface/groundwater interactions, the sub-catchment model demonstrated greater computational efficiency than the larger catchment model. Due to its significantly lower runtimes, we utilized the sub-catchment model to simulate various long-term climate change scenarios.

The computational grid for the surface flow domains of both models was generated using the preprocessor software AlgoMesh (HydroAlgorithmics Pty Ltd, 2016). AlgoMesh calculates an optimal triangular finite element mesh based on the Delaunay criteria. To accurately represent surface/groundwater interactions, both models utilized a refined surface mesh in areas where these interactions were anticipated, such as stream locations and wetland areas (Figure 2.2). The elevation of the surface nodes was obtained from a 5 m resolution digital elevation model (DEM). The final 2D mesh of the larger catchment model contains 3,399 nodes and 6,570 triangular elements, whereas the sub-catchment model includes 1,824 nodes and 3,507 triangular elements. To generate a 3D mesh for the subsurface flow domain, the 2D surface mesh was extended

vertically by three main layers: a top layer with a thickness of 5 m, and middle and bottom layers with a thickness of 10 m each. Furthermore, the top layer was subdivided into multiple sub-layers, each with a thickness of 0.5 m. The vertical discretization was kept identical for both models to ensure consistency. The final 3D grid for the Grosse Ohe catchment comprises 40,788 nodes and 78,840 elements, while the sub-catchment grid consists of 21,888 nodes and 42,084 elements. Vertical discretization was implemented to represent the geological conditions within the two catchments with a shallow soil layer, a regolith main aquifer and an impermeable bedrock layer. Around 5.6% of the total area of the catchment are riparian wetlands with an average thickness of 1 to 2m. Wetlands were represented using an exponentially decaying hydraulic conductivity (Ksat) distribution with depth, following the approach proposed by Frei et al. (2010). All Ksat values (wetlands, soil layer and regolith aquifer) were parameterized during the calibration process, and the final values can be found in Table S2.1 as part of the supplement. Different overland flow and evapotranspiration properties were assigned to the forested and wetland areas as well as to the stream segments (see Table S2.1 supplement).

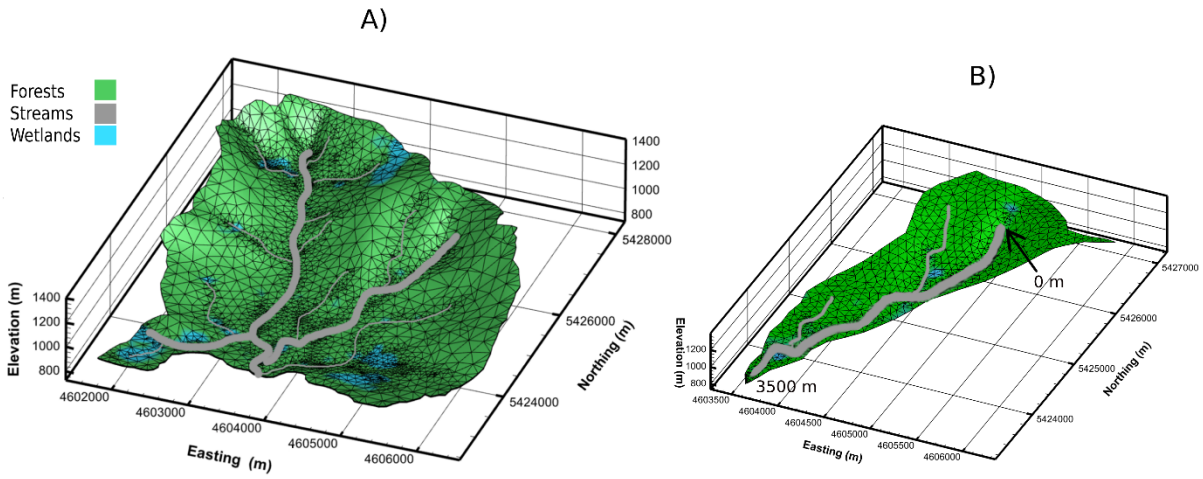


Figure 2.2. Model discretization of the A) Grosse Ohe catchment and B) the sub-catchment Hinterer Schachtenbach. The label 0 and 3500 m refer to the total stream length used in Figure 2.6 and 2.7.

All boundary nodes at the catchment/sub-catchment boundaries in the surface and subsurface flow domains, except for the outlet nodes (surface flow domain), were set as no-flow boundaries. Additionally, the subsurface nodes representing the impermeable bedrock also were assigned as no-flow boundary conditions. A critical depth boundary was assigned to the surface nodes representing the outlet of the catchment/sub-catchment, allowing the water to leave the surface flow domain at the outlet location. Spatially uniform daily rainfall and evapotranspiration rates were applied as upper flux boundaries for both models to the surface flow domain. Precipitation is the combined input of rainfall and snowmelt. To simulate snowmelt, we utilized the HBV light model (Seibert, 1997), which has been previously used in combination with process-based hydrological modeling, as presented in Kaule and Frei (2022). HBV uses the degree-day method to estimate snowmelt based on the air temperature.

2.2.4 Climate Projections

The Intergovernmental Panel on Climate Change (IPCC) introduced the Representative Concentration Pathways (RCPs) in its fifth assessment report (AR5). These pathways play a crucial role in understanding the exploration of climate change simulations and long-term predictions up to 2100. The Regional Climate Model (RCM) output from the EURO-CORDEX and ReKlies project was used in this model and was provided and downscaled by the Bavarian State Office for Environment (LFU). RCM is a time series of high-resolution climate data (0.11^{o} or 12 km) for the period of 1951-2006 and future scenarios ranging from 2006-2100. The selection of GCM and downscaling is very important as every GCM has its strengths and shortcomings (IPCC, 2014). The original RCM resolution is 12.5 x 12.5 km, but the LFU increased it to a 5 x 5 km grid resolution. The downscaling was carried out using the method proposed by Marke (2008). The presence of deviations between climate models and historical data is known as bias. This bias can be corrected using bias adjustment or bias correction methods. The bias adjustment method uses the Quantile Delta Mapping method (Cannon et al.,

2015) and is widely used in various studies to adjust the bias between projected and observed data (Maraun, 2013; Rajczak et al., 2016; Kim et al., 2016; Ngai et al., 2017; Ringard et al., 2017; Reiter et al., 2018). In order to evaluate potential impacts of climate change on stream water availability for the sub-catchment, in total we used 23 downscaled projections as input to the HGS model (6 from RCP 4.5, 8 from RCP2.6 and 9 from RCP 8.5, Table 2.1), detailed RCMs with their names are provided in Table 2.1. Each projection was split into two periods: (1) near future 2021-2050 and (2) far future 2071-2099. As a reference we additionally simulated the period from 1992 to 2018 based on available historical data. To investigate the impact of climate change on water balance components, each projection was simulated separately. Notably, each ensemble member contributed equally to the ensemble mean with a uniform weighting. The ensemble means of precipitation, evapotranspiration, discharge, and storage change for each pathway were calculated and compared with the reference period.

Table 2.1. Overview of the average annual temperature and total annual precipitation for the applied climate change scenarios. Each scenario corresponds to a combination of a Global Climate Model (GCM) and a Regional Climate Model (RCM).

GCM	**RCP**	**RCM**	**Institute**	**T[°C] 2021-2050**	**P[mm]**	**T[°C] 2071-2099**	**P[mm]**
EC-EARTH	rcp2.6	CCLM4-8-17	CLMcom	8.24	1140.1	8.4	1169.1
EC-EARTH		RACMO22E	KNMI	8.47	1175.0	8.6	1197.3
EC-EARTH		RCA4	SMHI	8.67	1097.5	8.8	1114.1
MIROC		CCLM4-8-17	CLMcom	9.01	1000.0	9.1	1048.2
MPI		WETTREG2018	CEC	8.35	1101.3	8.4	1085.8
MPI		CCLM4-8-17	CLMcom	8.33	1189.0	8.2	1155.8
MPI		RCA4	SMHI	8.87	1171.7	8.7	1100.5
MPI		WRF361H	UHOH	8.53	1088.2	8.6	1009.8
EC-EARTH	rcp4.5	CCLM4-8-17	CLMcom	8.45	1100.0	9.3	1182.1
EC-EARTH		RACMO22E r12	KNMI	8.75	1190.5	9.8	1228.9
EC-EARTH		RCA4	SMHI	8.85	1125.6	10.0	1193.0
EC-EARTH		RACMO22E	KNMI	8.86	1105.1	9.8	1120.7
MPI		CCLM4-8-17	CLMcom	8.22	1184.3	8.9	1173.8
MPI		RCA4	SMHI	8.67	1155.8	9.6	1185.7
EC-EARTH	rcp8.5	CCLM4-8-17	CLMcom	8.71	1176.5	11.0	1132.4
EC-EARTH		RACMO22Er12	KNMI	9.06	1234.4	11.6	1246.9
EC-EARTH		RCA4	SMHI	9.24	1176.4	12.0	1163.4
EC-EARTH		RACMO22E	KNMI	8.97	1147.4	11.5	1220.6
EC-EARTH		WRF361H	UHOH	8.84	1139.5	11.2	1044.5

Continued on next page

GCM	RCP	RCM	Institute	T[°C] 2021-2050	P[mm] 2021-2050	T[°C] 2071-2099	P[mm] 2071-2099
MPI		WETTREG	CEC	8.78	1059.8	11.0	992.3
MPI		CCLM4-8-17	CLMcom	8.31	1174.4	10.5	1219.4
MPI		RCA4	SMHI	8.69	1136.3	11.5	1268.5
MPI		WRF361H	UHOH	8.43	1078.0	10.7	1045.9

2.3 Results

2.3.1 Model Performance

The model was calibrated for the water year 2017 (11/01/2017 – 10/31/2018) based on available daily runoff data measured at the outlet of the Große Ohe catchment. Due to the high computational demand of the large catchment model and associated long simulation runtimes, calibration was performed manually. Using only a single hydrological year for model calibration is frequently employed when utilizing process-based and fully distributed hydrological models (e.g. Cornelissen et al., 2013; Glaser et al., 2016; De Schepper et al., 2017; Kaule and Frei, 2022). Validation was performed for the water years 2004-2017 (11/01/2004 – 10/31/2017). Figure 2.3 presents the observed and simulated discharge of the Große Ohe catchment during the calibration and validation period. The Nash-Sutcliffe-Efficiency (NSE) for the calibration period was estimated at 0.61, suggesting a satisfactory agreement between the observed and simulated discharge values. Despite a slightly lower NSE value of 0.51 for the validation period, the performance of the process-based hydrological model remains acceptable (Moriasi et al., 2007). Especially during low flow conditions in summer/early autumn, discharge was represented very well by the HGS model, as suggested by the high NSE score of 0.67 for this period. The simulations however proved challenging when high flow conditions were encountered since peak discharges were often systematically underestimated. This discrepancy can be partly attributed by the underestimation of precipitation rates during snow-melting events in winter and spring, as predicted by the degree-day method. Additionally, the insufficient resolution of the DEM used in

the study is unable to capture the small-scale topographical features (stream width < 1m) of the stream network, contributing to the disparity between the observed and simulated discharge values during high flow events.

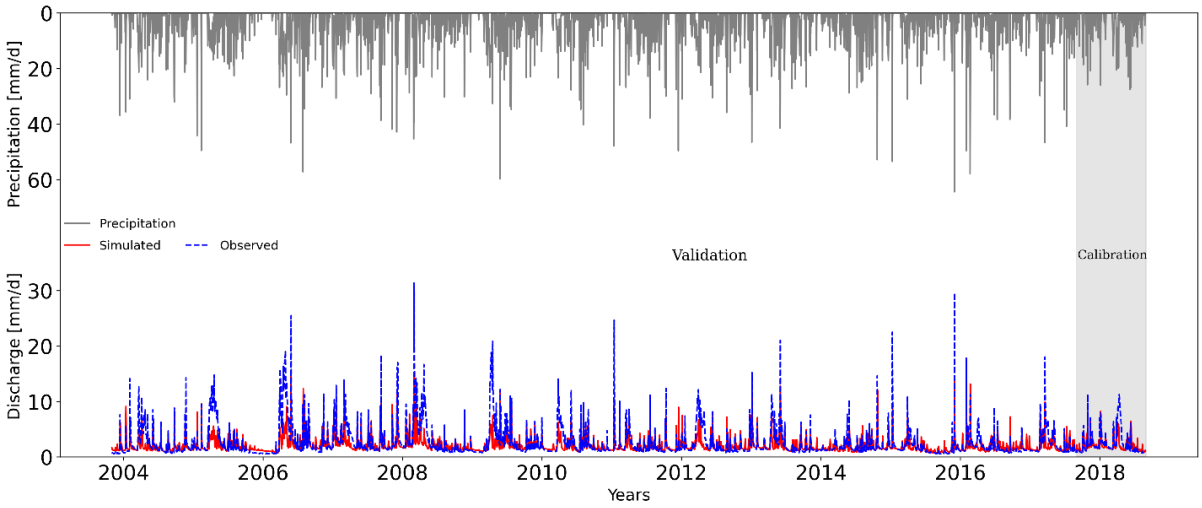


Figure 2.3. Simulated and observed discharge for the calibration (11/01/2017 – 10/31/2018) and validation (11/01/2004 – 10/31/2017) period. NSE for the calibration period is 0.61 and for the validation period 0.51

2.3.2 Impact of Climate Change on the Water Balance Components

The water balance of a catchment is a representation of the balance between precipitation (P), actual evapotranspiration (AET), discharge (Q), and storage change (ΔS). These components can help in understanding the changing hydrological conditions. Table 2.2 shows the mean annual water balance components for the different RCP ensembles utilized in the sub-catchment model. Figure 2.4 illustrates the seasonally-averaged water balance components for the sub-catchment, for the water years 2021-2050 (A, C, E,G), 2071-2099 (B, D, F,H), with the reference period of 1992-2018. According to the near future simulations using ensembles from RCP 2.6, 4.5 and 8.5, the annual average precipitation (including both rainfall and snowmelt) is expected to decrease by -9%, -12%, and -12%, respectively, compared to the reference period (Table 2.2). The far future simulations using ensembles from RCP 2.6, 4.5, and 8.5 suggest that the annual average precipitation inputs will decrease by -15%, -11%, and -22%, respectively, com-

pared to the reference period (Table 2.2). Figure 2.4A, indicates that all simulated RCP ensembles demonstrated a similar trend for precipitation, with a substantial decrease in seasonally-averaged precipitation rates during spring, summer, and autumn. For summer, the season where baseflow conditions are mostly relevant, ensemble simulations for RCP 8.5 for the far future showed the lowest seasonally-averaged precipitation inputs with a decrease of 141 mm compared to the reference period (Figure 2.4B). According to the simulations across all RCP ensembles, average winter precipitation (including rainfall and snowmelt) is projected to increase significantly. This increase can be attributed to a shift from snowfall towards rainfall and snowmelt, which is caused by higher predicted temperatures during winter.

In comparison to the reference period, the average annual rates of AET shown in Table 2.2 were similar for the near and far future simulations using RCP 2.6 (-4% and -3%) and RCP 4.5 (-3% and -0.5%). For the RCP 8.5 ensemble, average annual AET decreased by -4% for the near future and increased by +7% for the far future simulations (Table 2.2). On a seasonal basis, the average AET rates for all RCP ensembles in the near future simulations were lower compared to the reference period, and this trend was observed across all seasons (Figure 2.4E). In the far future simulations, particularly, simulations using the RCP 8.5 ensemble showed the highest seasonally-averaged AET for all seasons (Figure 2.4F). Simulations revealed a general reduction in surface water availability on an annual basis (Table 2.2), where average discharge decreased by -2%, -3%, and -8% (for RCP 2.6, 4.5 and 8.5, respectively) in the near future, and a severe reduction by -17%, -8%, and -34% (for RCP 2.6, 4.5 and 8.5, respectively) in the far future simulations. In the near future, simulations using all RCPs showed a notable increase in seasonally-averaged discharge during winter when compared to the reference period. However, for spring, summer, and autumn, a decrease in discharge was observed across all RCP ensembles. Simulations for all RCPs suggested a significant decrease in seasonally-averaged discharge for the far future. Lowest discharge values were simulated

during baseflow conditions in summer and autumn, with a maximum decrease of up to -50% for RCP 8.5 when compared to the reference period.

Table 2.2 shows that on average there was a slight water deficit of approximately -16 mm per year during the reference period. However, it's important to note that although this value is negative, the past conditions in the catchment can be considered as neutral. This is because the long-term storage changes in the catchment were relatively stable and did not result in significant overall gains or losses of water. For the near and far future simulations, average annual storage change revealed a substantial increase in water deficits for all RCP ensembles ranging from -375 to -719% when compared to the reference period (Table 2.2). A seven-fold increase in water deficit was predicted using the RCP 4.5 ensemble for the near future and a six-fold increase was predicted using RCP 8.5 for the far future. Figure 2.4 (G and H) present the simulated values for the seasonally-averaged storage change, wherein a positive value indicates that the catchment is gaining more water than it is losing, with water primarily stored in the subsurface (unsaturated zone + groundwater). Negative values correspond to situations where the catchment is losing more water than it is receiving, highlighting a deficit in the overall water budget. Based on the presented seasonally-averaged storage change especially spring and summer is affected by increasing water deficits as was predicted by all RCP ensembles in the near and far future simulations. On average, simulations for all RCP ensembles predict an excess of water during winter and autumn, although average storage changes are only slightly positive during autumn. This trend of increasing water deficits becomes even more pronounced in the period 2071-2099, with a significant shift in the water balance towards negative values, particularly in spring and summer. Statistical significance in the differences between the historical and the climate change scenarios was assessed through a t-test where $\alpha = 0.05$.

Table 2.2. Average annual components of the water balance of the sub-catchment for the different RCP ensembles and the historical reference period. Q = discharge, AET = actual evapotranspiration, and P = precipitation. The percentage in parentheses represent the relative change of the components to the historical reference period. The scenarios include near future (2021-2050) and far future (2071-2099) simulations for RCP 2.6, RCP 4.5, and RCP 8.5

Parameters	**Historic [mm/a]**	**Scenarios**	**RCP2.6 [mm/a]**	**RCP4.5 [mm/a]**	**RCP8.5 [mm/a]**
Discharge	716	2021-2050	700 (~-2%)	694 (~-3%)	658 (~-8%)
		2071-2099	597 (~-17%)	657 (~-8%)	469 (~-34%)
Precipitation	1330	2021-2050	1210 (~-9%)	1171 (~-12%)	1175 (~-12%)
		2071-2099	1131 (~-15%)	1181 (~-11%)	1034 (-22%)
AET	630	2021-2050	605 (~-4%)	608 (~-3%)	603 (~-4%)
		2071-2099	610 (~-3%)	627 (~-0.5%)	675 (+7%)
Storage Change	-16	2021-2050	-95 (~-494%)	-131 (~-719%)	-86 (~-438%)
		2071-2099	-76 (~-375%)	-103 (~-544%)	-110 (~-588%)

2.3.3 Impact of Climate Change on Stream-Aquifer interactions

For the sub-catchment simulations the total amount of groundwater inflow into the stream (exfiltration rates in Figure 2.5) was estimated for all RCP simulations on a seasonal basis. In both near and far future simulations, seasonally-averaged exfiltration rates show a significant decrease when compared to the historical reference period, indicating a severe reduction in groundwater availability for stream flow. Particularly during summer and autumn seasonally-averaged exfiltration rates showed a substantial decrease by up to -30% (RCP 8.5) compared to the reference period. Highest decreases in exfiltration rates throughout all seasons were simulated for the RCP 8.5 ensemble.

To better understand the potential consequences of declining groundwater levels in the sub-catchment under baseflow conditions, we investigated local surface-aquifer interactions by extracting spatially distributed exchange fluxes along the stream in the sub-catchment. Figure 2.6 presents the spatially distributed exchange fluxes extracted for all RCP ensembles and for all stream nodes in the sub-catchment model, ranging from spring areas (X=0 m) down to the sub-catchment's outlet (X=3500 m). Due to the unavailability of spatially distributed data across all RCP simulations and days during the summer and late autumn period, we made the choice to designate a reference day

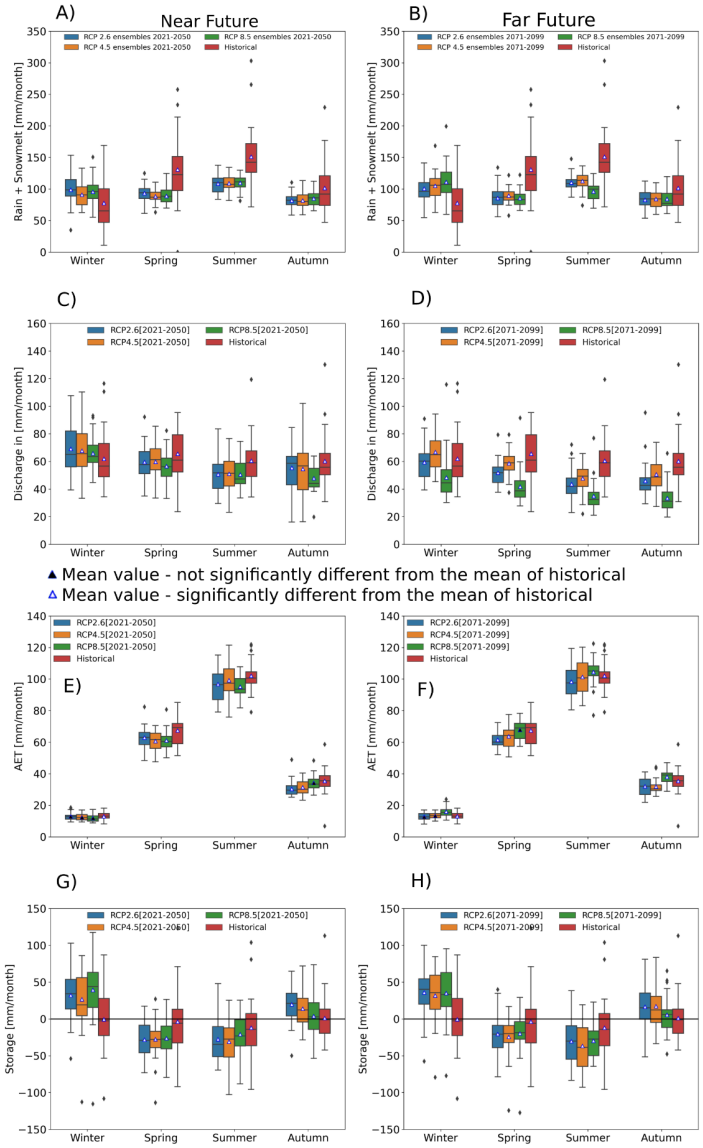


Figure 2.4. Mean water balance components for the Hinterer Schachtenbach subcatchment, presented seasonally for both the near future (2021-2050) and far future (2071-2099), across all Representative Concentration Pathway (RCP) projections. A,B Seasonally-averaged monthly precipitation (P) (mm/month); C,D) Seasonally-averaged monthly discharge (Q) (mm/month); E,F) Seasonally-averaged monthly actual evapotranspiration (AET) (mm/month);G,H) Seasonally-averaged monthly storage change (ΔS) (mm/month) The box represents the interquartile range (IQR), which spans from the 25th percentile (Q1) to the 75th percentile (Q3), with the median indicated by the line inside the box. The whiskers extend to the minimum and maximum values within 1.5 times the IQR from the upper and lower quartiles, respectively. Any data points outside of this range are displayed as points, representing potential outliers. Difference is significant at $\alpha = 0.05$

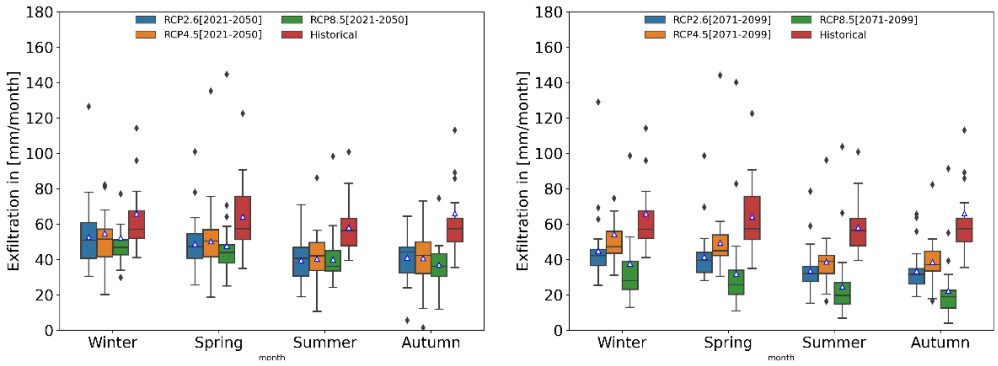


Figure 2.5. Seasonally-averaged total exfiltration rates between the groundwater and stream (exfiltration = inflow of groundwater to the stream) for the near and far future simulations and reference period.

for the purpose of evaluating groundwater-surface water interactions. To determine an appropriate reference day, we conducted an analysis of historical data spanning from 2002 to 2018, as well as predicted discharge from various RCP scenarios. Our analysis consistently revealed that the lowest mean discharge consistently took place in late summer, specifically in September. Consequently, we settled on the 15th of September as our reference day. For each RCP ensemble member and the reference period, the15$^{\text{th}}$ September of each year consequently was selected for which the local exchange fluxes were estimated.

Gaining stream sections are indicated by positive flux rates, while losing sections are indicated by negative rates. The flux rates for the reference period, which are presented as the average values estimated for the historic reference period (Blue lines in Figure 2.6), show that most stream sections in the past received water due to groundwater inflow. There are some stream reaches in the reference simulations where flux rates are negative indicating losing conditions. These losing conditions can be attributed to local topographical features (e.g. break in slope). In Figure 2.6, the areas shaded in grey depict the range of variation for the extracted exchange fluxes observed among the different simulations belonging to a specific RCP ensemble. All RCP ensembles show a similar trend of decreasing exchange fluxes between stream and aquifer. While certain

stream sections (1000m>X>1500m) exhibit a notable resilience to water deficits during summer (with exchange fluxes only marginally different from those observed during the reference period), the majority of both the upstream and downstream sections show a significant reduction in groundwater inflow due to declining groundwater levels. Especially the stream reaches close to upstream spring areas (X < 750 m) were most affected by the water deficit in the different RCP ensembles e.g. where exchange rates drop by up to ~88% (RCP 8.5 far future) compared to the reference period and where entire stream sections turn from gaining into losing sections (X < 250 m). This trend can be observed among all RCP ensembles and for the near as well as far future simulations.

Figure 2.7 illustrates the effect of the declining trend in groundwater inflow on surface water availability during baseflow conditions in the sub-catchment. For the reference day (September 15th), the average surface water depths in the past (historical reference period) ranged from 2.5 cm in the upstream spring areas to approximately 0.5 m at the sub-catchments' outlet. Simulation results for the historical reference period indicate that there was always sufficient instream water available from baseflow to sustain a continuous streamflow for all sections of the stream within the sub-catchment. For the near future simulations (Figure 2.7), all RCP ensembles predicted a significant decrease in surface water availability along the entire stream. Despite maintaining a continuous stream flow for the lower sections, the near-future simulations (Figure 2.7 A, C and E) show a significant decrease in surface water availability by up to 47% for the entire stream. However, due to falling groundwater levels and associated water loss to the aquifer, the most upstream sections (X<100m) in all RCP ensembles are projected to fall dry. A similar trend, with even less surface water availability (here water depths decrease by up to 50% compared to the reference period), is predicted for the far future (Figure 2.7 B, D and F).

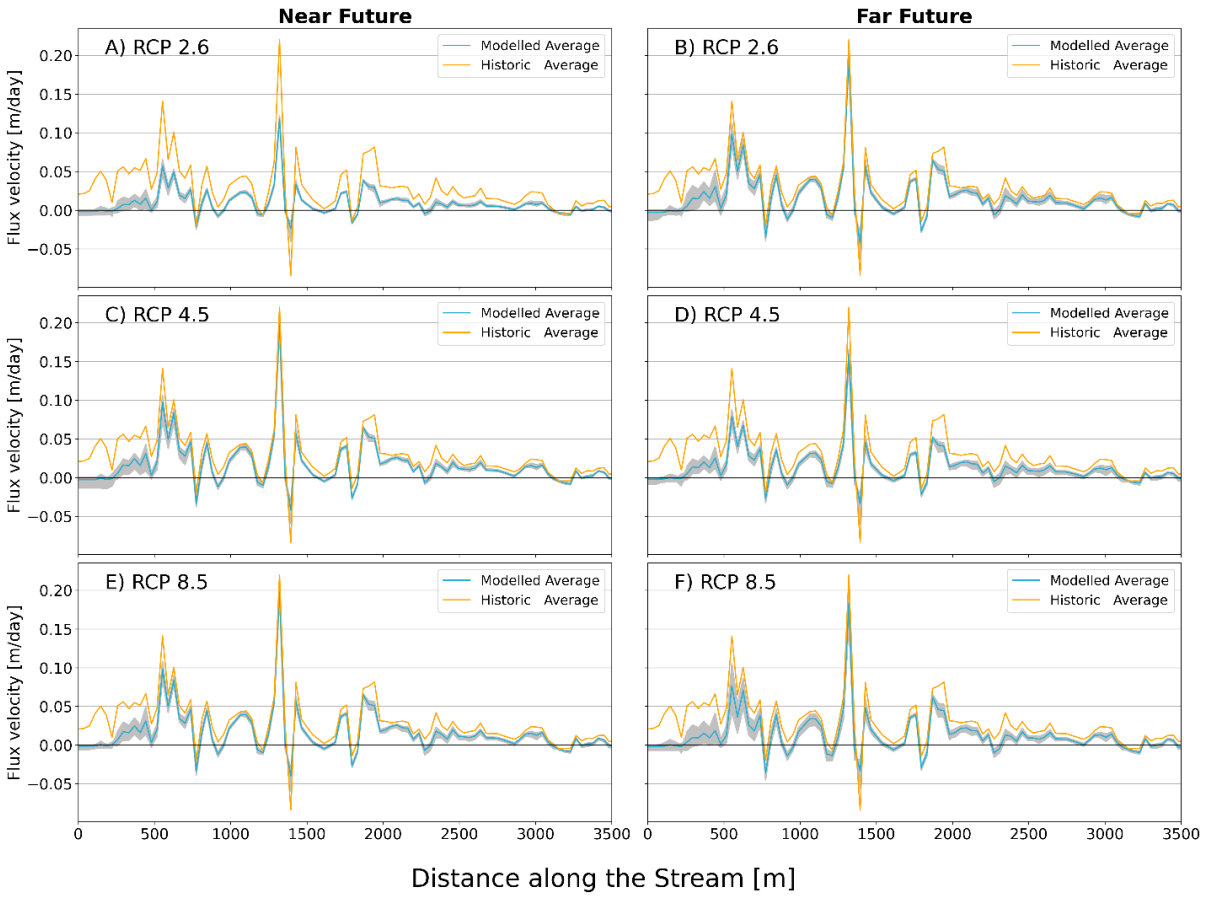


Figure 2.6. Illustrates the projected flux exchange between the stream and aquifer in m/d during baseflow conditions in late summer. The flux rates were estimated for September 15th for all RCP ensembles and the reference period, and the blueline represents the mean exchange flux for the reference period (1992 to 2018). The grey shaded area indicates the range of variation in the exchange rates for the different RCP scenarios.

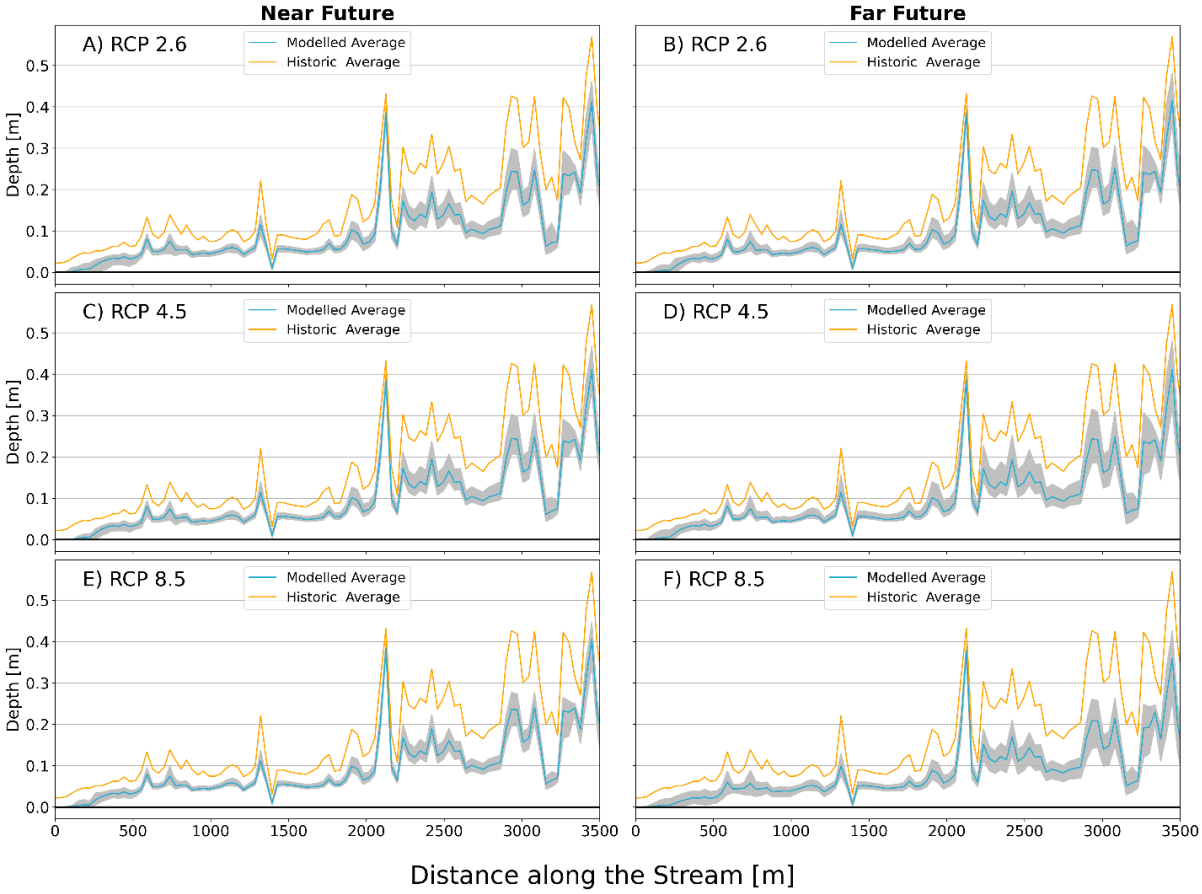


Figure 2.7. Projected surface water depths for the stream during baseflow conditions in late summer. Water depths were estimated for September 15th for all RCP ensembles and the reference period, and the Blue line represents the mean water depth for the reference period (1992 to 2018). The grey shaded area indicates the range of variation in water depths for the different RCP scenarios.

2.4 Discussion

In this study we used an integrated hydrological model to investigate how local climate change affects the water availability of a headwater catchment under baseflow conditions. Particularly, we focused on three different aspects: The impact of climate change on (1) the different components of the annual/seasonal water balance, (2) interactions between the stream and aquifer, and (3) availability of surface water resources. Model calibration and validation results revealed a good overall model performance, with NSE values of 0.61 and 0.51, respectively. These values are consistent with those typically reported in studies utilizing catchment-scale hydrological models (e.g. Glaser et al., 2016; Kaule and Frei, 2022; Partington et al., 2013). The model accurately represented catchment discharge under baseflow conditions. Simulations however proved challenging when high flow conditions were encountered since peak discharges were often systematically underestimated. This discrepancy can be partly attributed to the underestimation of snow-melting in winter and spring, as predicted by the degree-day method. Further, precipitation rates were spatially uniformly distributed over the catchment area, and the temporal model resolution required daily input data. Since intensive rainfall events can take place on temporal scales of minutes to hours, discharge peaks might have been missed in the model.

The study's predictions for the near and far future were generated using ensemble means derived from simulations of multiple ensemble members from different RCPs. Notably, each member contributed equally to the ensemble mean with uniform weighting. Ensemble members are usually chosen randomly from a larger population, which can introduce statistical biases and raise concerns about their representativeness for the whole population. One way to compensate for this, is to employ as many ensemble simulations as possible (Kaule and Frei, 2022). In our study we used all ensemble members that were available at the required resolution, which in total included 23 members from 3 different RCPs. Since the downscaling of the scenarios was performed by the Bavarian

State Office for Environment (LFU) rather than by ourselves, we had to depend on the available number of ensemble members provided to us. Varying model performances of different ensemble members can introduce biases into the simulation results that might be compensated by using non-uniform weights. Weighting methods, however, require detailed information such as each member's skill, error, and noise, which is often unavailable (Weigel et al., 2010). Hence, Weigel et al. (2010) recommended equal weights as the safest of all possible methods.

Across all RCP simulations, there is a consistent change towards increasing water deficits in summer and autumn predicted for both near and far future scenarios. The simulations showed that the annual average water deficits were approximately 4 to 7 times higher than those observed during the historical reference period. Highest water deficits of ~-590% and ~-720% were simulated for RCP 4.5 (near future) and RCP 8.5 (far future), respectively. Increasing water deficits can be primarily attributed to the projected reduction in precipitation inputs by up to -22%, as opposed to AET rates which remain similar to those observed during the historical reference period. Only the RCP 8.5 far future ensemble showed a significant increase of 7% in mean annual AET rates. These findings differ from results of other studies that predict a general decrease in precipitation inputs and a significant shift towards increasing AET rates for European headwater catchments (e.g. Benčoková et al., 2011; Kaule and Frei, 2022). A limitation of our study is that potential shifts in the compositions and distribution of vegetation were not accounted for in our simulations. However, it is highly likely that the vegetation composition, particularly in tree species, will undergo changes in the next 80-100 years. Reasons for this are adaptation to more frequent and longer drought conditions or infestation by pests such as bark beetles. Changes in plant communities are likely to affect AET rates and, consequently, will also impact water availability in the catchment. Incorporating vegetation changes into our simulations would require detailed scenarios regarding the timescales of transition as well as vegetation-specific

parameters that can be used to estimate AET. However, developing scenarios for future vegetation composition is outside the scope of our expertise and beyond the objectives of our study.

Prolonged water deficit conditions resulted in declining groundwater storage reserves within the catchment. As a result of declining groundwater levels and the associated reduction in baseflow input, the stream network within the catchment is expected to undergo a significant decline in surface water availability especially during summer and autumn. A reduction in annual mean stream discharge by up to -34% compared to the reference period was evident across all emission scenarios and is most notable during baseflow conditions in the late summer and early autumn months. The analysis of spatial exchange fluxes during the historical reference period indicated that the catchment's stream is primarily gaining water from groundwater inflow during baseflow conditions. There are some reaches in the simulations where the stream loses water to the aquifer, which can be explained by local topographical features such as breaks in slope. Small-scale transitions between gaining and losing conditions as a consequence of topography or instream obstacles such as beaver dams or dead trees has been described in literature as a common feature of headwater catchments (Huntington and Niswonger, 2012; Majerova et al., 2015). The RCP simulations indicate that a reduction in absolute exchange rates will affect all stream reaches, including those with gaining and losing conditions, as well as those located in higher and lower areas of the catchment. However, for upstream reaches the reduction of groundwater inflow under baseflow conditions has severe consequences for the surface water availability as the stream becomes temporarily intermittent. Consequently, during summer and autumn it is predicted that the stream network within the catchment will diminish by up to 200m, as upstream reaches near spring areas dry up as they lose the connection to the local groundwater. Similar findings were presented in Ward et al. (2020) that were examining stream network dynamics for headwater catchments in the U.S. Pacific

Northwest. Here it was predicted that Oregon's headwaters could experience a 25% decrease in flow pathways during the driest months, ultimately leading to a reduction in the length of flowing river networks. Similarly, Kaule and Gilfedder (2021) highlighted that in the lower mountain ranges of central Europe, extreme weather events and prolonged drought conditions could potentially leading to stream disconnection and a severe reduction in surface water availability under climate change conditions.

2.5 Conclusions and Implications

Our study aimed to investigate the impact of regional climate change on the water availability of a small headwater stream in the Bavarian Forest region of Germany. We used an integrated hydrological model in combination with multiple ensembles from different Representative Concentration Pathways (RCPs) to examine the potential effects of climate change on the stream's water resources. Simulations indicated:

(1) A significant decrease in precipitation inputs for the near (2021-2050) and far future (2071-2099).

(2) Rates of actual evapotranspiration that are comparable when related to the historical reference period (1992-2017).

(3) Prolonged water deficit conditions in future, resulting in declining groundwater levels in the catchment.

(4) A significant reduction in groundwater inflow during baseflow conditions leading to a temporal intermittence of the stream for upstream reaches

(5) A reduction of the total flow length by up to 200m for the stream network in the catchment

These findings potentially can have significant implications for the ecosystem, as decreasing water availability may lead to changes in the water flow regime, increased water temperature and lower oxygen availability. Especially spring ecosystems depend

on the continuous supply of groundwater and in mid mountain ranges are characterized by low temperature variability (Biggs et al., 2016). These ecosystems are recognized as biodiversity hotspots that serve as habitats for a diverse range of species that occupy various ecotonal niches (Cantonati et al., 2012). Supply of groundwater from spring areas is important for the regulation of water temperature and oxygen levels for downstream reaches, which is especially relevant during hot summer months when water temperatures can reach stressful levels for aquatic organisms (Power et al., 1999). Springs are the birthplace of 1st order streams, typically located in the upstream areas of headwater catchments. Our simulations have demonstrated that upstream reaches are especially vulnerable to the effects of decreasing groundwater levels, with a high likelihood that streams in these areas will become intermittent in summer (as was projected by all RCP scenarios). For spring areas this could mean that water supply from groundwater will decrease substantially or could be interrupted entirely with fatal consequences for these sensitive ecosystem and the associated ecosystem services.

Headwaters play a crucial role in maintaining forest biodiversity by providing unique habitats, but they are also particularly vulnerable to the effects of climate change as was shown by our simulations and various other authors (e.g. Brooks, 2009; Estrela-Segrelles et al., 2023; López-de Sancha et al., 2022; Ward et al., 2020). The anticipated increase in air temperatures, coupled with declining inputs from groundwater sources, is expected to cause a shift towards higher water temperatures in future (Van Vliet et al., 2013). For higher water temperatures, transmission rates of certain diseases can increase, posing health risks to freshwater species such as fish (Karvonen et al., 2010). All RCP scenarios predict a decline in summer precipitation, which, when combined with reduced groundwater supply and increasing water temperatures, may lead to lower dissolved oxygen concentrations and increased biological oxygen demand in headwater streams, thereby posing a threat to aquatic life (Whitehead et al., 2009). Plant communities that have adapted to high water saturation environments, such as

riparian areas or wetlands, will be impacted by the decreasing availability of surface water during droughts, potentially resulting in a reduction in the size of these areas over time (Dwire et al., 2018). Once headwater streams become intermittent, species communities unadopted to such dry conditions might face trouble to regain vitality fast which might lead to a shift in the species composition (Majdi et al., 2020).

Acknowledgements

This work was supported by the Bavarian State Ministry of Science and the Arts in the Bavarian Climate Research Network (bayklif). We thank the Bavarian State Office for Environment for providing the climate change scenarios (original dataset obtained from Euro-Cordex and ReKliEs-DE). The authors would like to thank the Bavarian Forest National Park administration, for providing physiographic and meteorological data. The authors also thank the Higher Education Commission of Pakistan (HEC) for the scholarship funds jointly provided by the German Academic Exchange Service (DAAD).

Conflict of Interest

The authors declare that they have no conflict of interest.

References

Al-Mukhtar M, Dunger V, Merkel B (2014) Assessing the Impacts of Climate Change on Hydrology of the Upper Reach of the Spree River: Germany. Water Resour Manag 28:2731–2749.

Ala-aho P, Soulsby C, Wang H, Tetzlaff D (2017) Integrated surface-subsurface model to investigate the role of groundwater in headwater catchment runoff generation: A minimalist approach to parameterisation. J Hydrol 547:664–677.

Alexander RB, Boyer EW, Smith RA, et al (2007) The Role of Headwater Streams in Downstream Water Quality. JAWRA J Am Water Resour Assoc 43:41–59.

Allen GH, Pavelsky TM, Barefoot EA, et al (2018) Similarity of stream width distributions across headwater systems. Nat Commun 9:610.

Allen RG, Pereira LS, Raes D, Smith M (1998) Crop evapotranspiration —guidelines for computing crop water requirements. FAO Irrigation and drainage paper 56. Food and Agriculture Organization, Rome

Aquanty Inc. (2015) HydroGeoSphere: A three-dimensional numerical model describing fully-integrated subsurface and surface flow and solute transport. Groundwater Simulations Group, University of Waterloo

Arthington AH, Bunn SE, Poff NLR, Naiman RJ (2006) The challenge of providing environmental flow rules to sustain river ecosystems. Ecol Appl 16:1311–1318.

Atawneh DA, Cartwright N, Bertone E (2021) Climate change and its impact on the projected values of groundwater recharge: A review. J Hydrol 601:126602.

Baldwin HL, McGuinness CL (1963) A primer on ground water. U.S. Geological Survey, Washington, D.C.

Bässler C (2008) Climate change-trend of air temperature in the Innerer Bayerischer Wald (Bohemian Forest). Silva Gabreta 14:1–18.

Beatty SJ, Morgan DL, McAleer FJ, Ramsay AR (2010) Groundwater contribution to baseflow maintains habitat connectivity for Tandanus bostocki (Teleostei: Plotosidae) in a south-western Australian river. Ecol Freshw Fish 19:595–608.

Benčoková A, Krám P, Hruška J (2011) Future climate and changes in flow patterns in Czech headwater catchments. Clim Res 49:1–15.

Bennett KE, Werner AT, Schnorbus M (2012) Uncertainties in Hydrologic and Climate Change Impact Analyses in Headwater Basins of British Columbia. J Clim 25:5711–5730.

Bernsteinová J, Bässler C, Zimmermann L, et al (2015) Changes in runoff in two neighbouring catchments in the Bohemian Forest related to climate and land cover changes. J Hydrol Hydromechanics 63:342–352.

Beudert B, Bässler C, Thorn S, et al (2015) Bark Beetles Increase Biodiversity While Maintaining Drinking Water Quality. Conserv Lett 8:272–281.

Biggs J, von Fumetti S, Kelly-Quinn M (2016) The importance of small waterbodies for biodiversity and ecosystem services: implications for policy makers. Hydrobiologia 793:3–39.

Brooks RT (2009) Potential impacts of global climate change on the hydrology and ecology of ephemeral freshwater systems of the forests of the northeastern United States. Clim Change 95:469–483.

Cannon AJ, Sobie SR, Murdock TQ (2015) Bias Correction of GCM Precipitation by Quantile Mapping: How Well Do Methods Preserve Changes in Quantiles and Extremes? J Clim 28:6938–6959.

Cantonati M, Füreder L, Gerecke R, et al (2012) Crenic habitats, hotspots for freshwater biodiversity conservation: toward an understanding of their ecology. Freshw Sci 31:463–480.

Chan SS, Seidenfaden IK, Jensen KH, Sonnenborg TO (2021) Climate change impacts and uncertainty on spatiotemporal variations of drought indices for an irrigated catchment. J Hydrol 601:126814.

Chen JW, Kuo HT, Lin HL (2016) Estimation the hot spring recharge using groundwater numerical model in Jiao-Shi area, Taiwan. Proc IEEE Int Conf Adv Mater Sci Eng Innov Sci Eng IEEE-ICAMSE 434–437.

Choi B, Kang H, Lee WH (2018) Baseflow Contribution to Streamflow and Aquatic Habitats Using Physical Habitat Simulations. Water 10:1304.

Cloutier CA, Buffin-Bélanger T, Larocque M (2014) Controls of groundwater floodwave propagation in a gravelly floodplain. J Hydrol 511:423–431.

Conant B (2004) Delineating and Quantifying Ground Water Discharge Zones Using Streambed Temperatures. Ground Water 42:243–257.

Cornelissen T, Diekkrüger B, Bogena H (2013) Using HydroGeoSphere in a Forested Catchment: How does Spatial Resolution Influence the Simulation of Spatio-temporal Soil Moisture Variability? Procedia Environ Sci 19:198–207.

De Schepper G, Therrien R, Refsgaard JC, et al (2017) Simulating seasonal variations of tile drainage discharge in an agricultural catchment. Water Resour Res 53:3896–3920.

Delleur JW (1999) The handbook of groundwater engineering. CRC Press, Boca Raton, FL

Downing JA, Cole JJ, Duarte CM, et al (2012) Global abundance and size distribution of streams and rivers. Inl Waters 2:229–236.

Dwire KA, Mellmann-Brown S, Gurrieri JT (2018) Potential effects of climate change on riparian areas, wetlands, and groundwater-dependent ecosystems in the Blue Mountains, Oregon, USA. Clim Serv 10:44–52.

Estrela-Segrelles C, Gómez-Martínez G, Pérez-Martín MÁ (2023) Climate Change Risks on Mediterranean River Ecosystems and Adaptation Measures (Spain). Water Resour Manag 37:2757–2770.

Fleckenstein JH, Niswonger RG, Fogg GE (2006) River-aquifer interactions, geologic heterogeneity, and low-flow management. Ground Water 44:837–852.

Frei S, Fleckenstein JH, Kollet SJ, Maxwell RM (2009) Patterns and dynamics of river-aquifer exchange with variably-saturated flow using a fully-coupled model. J Hydrol 375:383–393.

Frei S, Lischeid G, Fleckenstein JH (2010) Effects of micro-topography on surface–subsurface exchange and runoff generation in a virtual riparian wetland — A modeling study. Adv Water Resour 33:1388–1401.

Glaser B, Klaus J, Frei S, et al (2016) On the value of surface saturated area dynamics mapped with thermal infrared imagery for modeling the hillslope-riparian-stream continuum. Water Resour Res 52:8317–8342.

Goderniaux P, Brouyère S, Fowler HJ, et al (2009) Large scale surface-subsurface hydrological model to assess climate change impacts on groundwater reserves. J Hydrol 373:122–138.

Goderniaux P, Brouyère S, Wildemeersch S, et al (2015) Uncertainty of climate change impact on groundwater reserves - Application to a chalk aquifer. J Hydrol 528:108–121.

Gosling SN, Zaherpour J, Mount NJ, et al (2017) A comparison of changes in river runoff from multiple global and catchment-scale hydrological models under global warming scenarios of 1 °C, 2 °C and 3 °C. Clim Change 141:577–595.

Huang S, Krysanova V, Österle H, Hattermann FF (2010) Simulation of spatiotemporal dynamics of water fluxes in Germany under climate change. Hydrol Process 24:3289–3306.

Huntington JL, Niswonger RG (2012) Role of surface-water and groundwater interactions on projected summertime streamflow in snow dominated regions: An integrated modeling approach. Water Resour Res 48:W11524.

HydroAlgorithmics Pty Ltd (2016) AlgoMesh User Guide.

IPCC (2014) Climate Change 2014: Synthesis Report. Contribution of Working Groups I, II and III to the Fifth Assessment Report of the Intergovernmental Panel on Climate Change [Core Writing Team, R.K. Pachauri and L.A. Meyer (eds.)]. IPCC, Geneva, Switzerland

Karvonen A, Rintamäki P, Jokela J, Valtonen ET (2010) Increasing water temperature and disease risks in aquatic systems: climate change increases the risk of some, but not all, diseases. Int J Parasitol 40:1483–1488.

Kaule L, Frei S (2022) Analysis of drought conditions and their impacts in a headwater stream in the Central European lower mountain ranges. Reg Environ Change 22:82.

Kaule R, Gilfedder BS (2021) Groundwater Dominates Water Fluxes in a Headwater Catchment During Drought. Front Water 3:706932.

Kim MK, Kim S, Kim J, et al (2016) Statistical downscaling for daily precipitation in Korea using combined PRISM, RCM, and quantile mapping: Part 1, methodology and evaluation in historical simulation. Asia-Pacific J Atmos Sci 52:79–89.

Krause S, Bronstert A, Zehe E (2007) Groundwater-surface water interactions in a North German lowland floodplain - Implications for the river discharge dynamics and riparian water balance. J Hydrol 347:404–417.

Kristensen KJ, Jensen SE (1975) A model for estimating actual evapotranspiration from potential evapotranspiration. Nord Hydrol 6:170–188.

López-de Sancha A, Roig R, Jiménez I, et al (2022) Impacts of damming and climate change on the ecosystem structure of headwater streams: a case study from the Pyrenees. Inl Waters 12:434–450.

Majdi N, Colls M, Weiss L, et al (2020) Duration and frequency of non-flow periods affect the abundance and diversity of stream meiofauna. Freshw Biol 65:1906–1922.

Majerova M, Neilson BT, Schmadel NM, et al (2015) Impacts of beaver dams on hydrologic and temperature regimes in a mountain stream. Hydrol Earth Syst Sci 19:3541–3556.

Maraun D (2013) Bias Correction, Quantile Mapping, and Downscaling: Revisiting the Inflation Issue. J Clim 26:2137–2143.

Marke T (2008) Development and Application of a Model Interface To couple Land Surface Models with Regional Climate Models For Climate Change Risk Assessment in the Upper Danube Watershed. Ludwig Maximilian University of Munich

Marx A, Kumar R, Thober S, et al (2018) Climate change alters low flows in Europe under global warming of 1.5, 2, and 3°C. Hydrol Earth Syst Sci 22:1017–1032.

Miller MP, Buto SG, Susong DD, Rumsey CA (2016) The importance of base flow in sustaining surface water flow in the Upper Colorado River Basin. Water Resour Res 52:3547–3562.

Min L, Shen Y, Pei H (2015) Estimating groundwater recharge using deep vadose zone data under typical irrigated cropland in the piedmont region of the North China Plain. J Hydrol 527:305–315.

Misra D, Daanen RP, Thompson AM (2011) Base Flow/Groundwater Flow. In: Singh, V.P., Singh, P., Haritashya, U.K. (eds) Encyclopedia of Snow, Ice and Glaciers. Encyclopedia of Earth Sciences Series. Springer, Dordrecht, pp 90–93

Molano-Leno L, Kohfahl C, Martínez Suárez DJ, et al (2018) Investigating the Impact of Climate Change on Groundwater Recharge Using a High Precision Meteo Lysimeter in a Dune Belt of the Doñana National Park. In: Calvache, M., Duque, C., Pulido-Velazquez, D. (eds) Groundwater and Global Change in the Western Mediterranean Area. Environmental Earth Sciences. Springer, Cham, pp 227–234

Moriasi DN, Arnold JG, Van Liew MW, et al (2007) Model Evaluation Guidelines for Systematic Quantification of Accuracy in Watershed Simulations. Trans ASABE 50:885–900.

Natkhin M, Steidl J, Dietrich O, et al (2012) Differentiating between climate effects and forest growth dynamics effects on decreasing groundwater recharge in a lowland region in Northeast Germany. J Hydrol 448–449:245–254.

Ngai ST, Tangang F, Juneng L (2017) Bias correction of global and regional simulated daily precipitation and surface mean temperature over Southeast Asia using quantile mapping method. Glob Planet Change 149:79–90.

Niswonger RG, Fogg GE (2008) Influence of perched groundwater on base flow. Water Resour Res 44:W03405.

Nyquist JE, Freyer PA, Toran L (2008) Stream bottom resistivity tomography to map ground water discharge. Ground Water 46:561–569.

O'Connor BL, Harvey JW (2008) Scaling hyporheic exchange and its influence on biogeochemical reactions in aquatic ecosystems. Water Resour Res 44:W12423.

Partington D, Brunner P, Frei S, et al (2013) Interpreting streamflow generation mechanisms from integrated surface-subsurface flow models of a riparian wetland and catchment. Water Resour Res 49:5501–5519.

Peralta-Tapia A, Sponseller RA, Ågren A, et al (2015) Scale-dependent groundwater contributions influence patterns of winter baseflow stream chemistry in boreal catchments. J Geophys Res Biogeosciences 120:847–858.

Power G, Brown RS, Imhof JG (1999) Groundwater and fish—insights from northern North America. Hydrol Process 13:401–422.

Rajczak J, Kotlarski S, Schär C (2016) Does Quantile Mapping of Simulated Precipitation Correct for Biases in Transition Probabilities and Spell Lengths? J Clim 29:1605–1615.

Reiter P, Gutjahr O, Schefczyk L, et al (2018) Does applying quantile mapping to subsamples improve the bias correction of daily precipitation? Int J Climatol 38:1623–1633.

Richter BD, Baumgartner JV, Wigington R, Braun DP (1997) How much water does a river need? Freshw Biol 37:231–249.

Ringard J, Seyler F, Linguet L (2017) A Quantile Mapping Bias Correction Method Based on Hydroclimatic Classification of the Guiana Shield. Sensors 17:1413.

Seibert J (1997) Estimation of Parameter Uncertainty in the HBV Model. Hydrol Res 28:247–262.

Taie Semiromi M, Koch M (2020) How Do Gaining and Losing Streams React to the Combined Effects of Climate Change and Pumping in the Gharehsoo River Basin, Iran? Water Resour Res 56:e2019WR025388.

Therrien R, McLaren R, Sudicky E, Panday S (2008) HydroGeoSphere: A three-dimensional numerical model describing fully-integrated subsurface and surface flow and solute transport (manual). Groundwater Simulations Group, University of Waterloo

Therrien R, McLaren RG, Sudicky EA, Panday SM (2010) HydroGeoSphere: A three-dimensional numerical model describing fully-integrated subsurface and surface flow and solute transport. Groundwater Simulations Group, University of Waterloo, Waterloo

Van Vliet MTH, Franssen WHP, Yearsley JR, et al (2013) Global river discharge and water temperature under climate change. Glob Environ Change 23:450–464.

Ward AS, Wondzell SM, Schmadel NM, Herzog SP (2020) Climate Change Causes River Network Contraction and Disconnection in the H.J. Andrews Experimental Forest, Oregon, USA. Front Water 2:7.

Weigel AP, Knutti R, Liniger MA, Appenzeller C (2010) Risks of Model Weighting in Multimodel Climate Projections. J Clim 23:4175–4191.

Whitehead PG, Wilby RL, Battarbee RW, et al (2009) A review of the potential impacts of climate change on surface water quality. Hydrol Sci J 54:101–123.

Wunsch A, Liesch T, Broda S (2022) Deep learning shows declining groundwater levels in Germany until 2100 due to climate change. Nat Commun 13:1221.

Supplementary Material

Table S2.1. Surface and subsurface calibrated parameters used in the model.

Subsurface flow parameters

Subsurface flow domain	**Hydraulic conductivity (m/day)**	**Porosity (–)**	**Residual saturation (–)**	**Unsaturated van Genuchten parameters**	
				α **(m^{-1})**	β **(–)**
Bottom, middle and top layer	1.1	0.4	0.1	2.69	1.45
Wetlands (bottom to top)	0.68, 1.5, 3.7, 8.6	0.5	0.1	3.5	1.7

Evapotranspiration parameters

Parameter	**Subparameter**	**Unit**	**Forest**	**Wetlands**
Leaf area index		–	6.5	2.08
Evaporative depth		m	1	3
Transpiration fitting parameters	C1	–	0.2	0.3
	C2		0.5	0.2
	C3		1	10
Transpiration limiting saturations	Wilting point	–	0.3	0.2
	Field capacity		0.34	0.32
	Oxic limit		1	0.76
	Anoxic limit		1	0.9
Canopy storage parameters		m	1×10^{-6}	0
Root depth		m	1	0.5
Evaporation limiting parameters	Minimum	–	0.3	0.2
	Maximum		0.4	0.32
Initial interception storage		m	1×10^{-6}	0

Surface flow parameters

Surface flow domain	**Manning's roughness n (d/m$^{1/3}$)**	**Coupling length (m)**	**Rill storage height (m)**
Forests	1.9×10^{-6}	0.1	0.5
Wetlands	8.1×10^{-5}	0.1	0.2
Streams	4.0×10^{-7}	0.1	0

3 Manuscript II: Runoff Generation and Groundwater Interactions in a Central European Headwater Catchment: Using Process-Based Modelling and Radon-222 as a Natural Tracer

Outline

Abstract . . . 85
3.1 Introduction . . . 85
3.2 Materials and Methods . . . 89
3.2.1 Field location . . . 89
3.2.2 ^{222}Rn Sampling . . . 90
3.2.3 Modelling . . . 91
3.2.4 Boundary conditions, calibration and simulations . . . 94
3.3 Results . . . 96
3.3.1 Modelled and Observed ^{222}Rn Concentrations . . . 97
3.3.2 Temporal model results at HS7 . . . 98
3.4 Discussion . . . 101
3.4.1 Persistent groundwater influence around HS6-HS7 . . . 101
3.4.2 Seasonal and rainfall-related behaviour at HS7 . . . 103
3.4.3 Local differences between streambed exchange and stream-water ^{222}Rn . . . 104
3.4.4 Endmember assumptions, model uncertainty and further measurements . . . 106
3.5 Conclusions . . . 108
References . . . 110
Supplementary Material . . . 116

Bibliographic Information

Munir, M. U., Gilfedder, B. S., and Frei, S. (submitted): Runoff Generation and Groundwater Interactions in a Central European Headwater Catchment: Using Process-Based Modelling and Radon-222 as a Natural Tracer. *Journal of Hydrology.*

Article Adaptation

The contents of the original version were slightly modified for inclusion in this dissertation, including adjustments to the numbering of sections, figures, tables, and equations. The manuscript was submitted to the Journal of Hydrology.

Abstract

Headwater catchments in Central European mountain ranges supply downstream rivers but respond rapidly to changes in precipitation, snow accumulation/melt and evapotranspiration. This study combines a process-based hydrological and solute-transport model that couples three-dimensional variably saturated subsurface flow, two-dimensional depth-averaged surface flow, and advective–dispersive reactive solute transport in the Grosse Ohe catchment, Germany. HydroGeoSphere (HGS), a fully integrated finite element flow and solute transport model was applied to simulate Radon-222 (^{222}Rn). The hydrological flow model was calibrated independently against catchment outlet runoff, while groundwater ^{222}Rn measurements were used to estimate the groundwater endmember concentration. Stream water ^{222}Rn concentrations from three sampling campaigns were used to calibrate and evaluate the transport component. Across 12 sites simulated and observed ^{222}Rn activity concentrations were strongly related in all three campaigns (R^2 = 0.86–0.88, all $p < 0.001$; RMSE 164–302 Bq m^{-3}; n = 12 per campaign). In all three campaigns the highest measured ^{222}Rn activity concentrations occurred within the same 600 m section of the stream, where the model also simulated the largest streambed exchange fluxes (25–31 mm d^{-1}). The results reveal a spatially variable reach scale groundwater-surface water exchange pattern. Although the estimated flux distribution remains model-dependent, it provides a plausible and physically consistent representation of exchange processes within the study reach.

3.1 Introduction

Headwater catchments in the Central European mountain ranges strongly influence water availability in downstream river reaches and stream networks (Kaule & Frei, 2022; Munir et al., 2024). Headwaters with limited storage in lakes or snowpacks are particularly vulnerable to the impacts of climate change, potentially leading to decreased water availability (Bennett et al., 2012). This vulnerability is connected to their strong

dependence on precipitation inputs and their sensitivity to changes in precipitation patterns, warmer air temperatures and land use (Bennett et al., 2012). Central European mountain headwaters are projected to experience substantial streamflow declines, especially in the wettest catchments, with consequences for ecological flows (Vlach et al., 2020). Research by Šanda et al. (2014) in the Jizera Mountains of the Czech Republic highlighted the importance of baseflow and snowmelt inputs for headwater streams. Similarly, Kaule & Gilfedder (2021) demonstrated the critical importance of groundwater contributions for maintaining streamflow in a Central European headwater catchment, particularly during drought periods.

The exchange between groundwater and surface water is a pivotal characteristic of the hydrological cycle, influencing water balances, water quality and ecosystem health (Fleckenstein et al., 2010; McCallum et al., 2012; Ortega et al., 2015; Shanafield & Cook, 2014). Historically, groundwater and surface water have been managed as separate entities, often overlooking this significant exchange (Chen, 2007; Sophocleous, 2002). This exchange is particularly important in headwater ecosystems, where groundwater contributions often sustain water availability, especially during dry seasons (Jia et al., 2021; Munir et al., 2024). Understanding and quantifying water and solute fluxes between groundwater and surface water are crucial for effective water resource management and ecosystem conservation (Brunke & Gonser, 1997; Munir et al., 2024).

Quantifying groundwater discharge to surface waters remains challenging due to difficulties in accurately measuring hydraulic conductivity and low hydraulic gradients in lake and wetland systems (Rosenberry et al., 2021). Usman et al. (2024) highlighted substantial uncertainty in rainfall-runoff prediction for the Simbach headwater catchment in southern Bavaria. Methods relying on water balance calculations for estimating groundwater discharge face limitations particularly because components such as actual evapotranspiration are difficult to quantify accurately (Faybishenko, 2010). Environmental tracers used to identify and quantify groundwater-surface water exchange

include major ions, stable isotopes, radioisotopes and temperature (Genereux et al., 1993; Cartwright et al., 2011; Shaw et al., 2014; Unland et al., 2013; Yang et al., 2018). Another effective approach employs stable hydrogen and oxygen isotopes, which are useful for understanding groundwater-surface water exchange (Liu et al., 2004; Petermann et al., 2018a; Pham et al., 2024; Qin et al., 2021; Schmidt et al., 2011; Yang et al., 2021; Yuan et al., 2020; Zhao et al., 2018).

Among these tracers, radon-222 (^{222}Rn) is frequently used to quantify groundwater-surface water exchange in freshwater and marine systems (Frei & Gilfedder, 2021; Gilfedder et al., 2015, 2019; Krabbenhoft & Webster, 1995; Petermann et al., 2018b; Petpongpan et al., 2022; Schubert et al., 2023). ^{222}Rn is a radioactive noble gas with a half-life of 3.83 days and can be used as a natural tracer to quantify groundwater discharge. It is produced by alpha decay of ^{226}Ra within the aquifer matrix, only the fraction that escapes the mineral grains into pore water the emanation fraction is available as a tracer. (Cecil & Green, 2000). Surface waters typically have lower ^{222}Rn concentrations than groundwater because of degassing, radioactive decay and the lack of significant production within the surface water. However, concentrations increase where groundwater discharges to rivers. These properties make ^{222}Rn a suitable tracer for quantifying groundwater-surface water exchange and identifying infiltration and discharge zones (Burnett & Dulaiova, 2003; Ellins et al., 1990). It presents significant advantages over other established tracer methods because of its simple and cost effective measurement and the large difference in concentration between groundwater and surface water. As a result, mobile ^{222}Rn detectors are becoming increasingly popular in studies examining groundwater-surface water exchange (Hofmann et al., 2011; Cranswick et al., 2014; Pittroff et al., 2017).

However, ^{222}Rn is limited in providing a broader, catchment wide perspective over longer periods and larger spatial extents (Adyasari et al., 2023). This limitation arises because ^{222}Rn has a short half-life, is rapidly lost by gas exchange and can have a spa-

tially variable groundwater endmember concentration. In contrast, longer-lived tracers (^{3}H–^{3}He, CFCs/SF_6 and ^{14}C) retain information over longer periods and behave more conservatively along flow paths. Hydrological and transport modelling can simulate groundwater-surface water exchange across broader temporal and spatial scales, offering a more comprehensive understanding of these systems. By combining tracer data with modelling, it is possible to constrain and evaluate models using field observations. For example, Dimova et al. (2013) combined ^{222}Rn with a steady-state mass-balance model to assess groundwater discharge into small lakes. Similarly, Frei & Gilfedder (2021) presented a framework that integrates ^{222}Rn as a natural tracer with modelling techniques to estimate mean residence times of bank filtrate in aquifers.

This study combines hydrological and transport modelling with longitudinal tracer surveys to examine local groundwater discharge to a headwater stream. The objectives are (i) to test whether a fully integrated flow and transport model, calibrated against catchment runoff alone, can reproduce the observed longitudinal ^{222}Rn pattern; (ii) to identify reaches in which groundwater discharge is persistently concentrated under different flow conditions; and (iii) to establish which features of the resulting exchange-flux distribution are constrained by the tracer data and which remain model-dependent. To achieve these objectives, we implement the fully integrated control-volume finite-element hydrological model HydroGeoSphere (HGS), which solves the three-dimensional Richards equation for variably saturated groundwater flow and couples it to two-dimensional depth-averaged surface flow. The flow model simulates streambed exchange flux independently of the ^{222}Rn observations and the resulting flow fields drive the solute transport model. Groundwater ^{222}Rn measurements were used to define the groundwater endmember concentration, while stream-water ^{222}Rn concentrations from three sampling campaigns were used to calibrate and evaluate the transport component. ^{222}Rn has previously been simulated explicitly in HGS for hyporheic and bank-storage systems (Gilfedder et al., 2019) and coupled with HGS to estimate bank-

filtrate residence times (Frei & Gilfedder, 2021), and the flow model used here was developed and evaluated for this catchment in an earlier study (Munir et al., 2024). The contribution of the present work is to bring these elements together at the catchment scale in a configuration in which the flow field is calibrated entirely independently of the tracer, and to evaluate the resulting transport model against three longitudinal surveys carried out under different low-to-moderate flow conditions. This design allows the persistence of a groundwater-discharge zone to be tested rather than inferred from a single survey, and allows the location of that zone to be assessed separately from the magnitude of the associated exchange flux.

3.2 Materials and Methods

3.2.1 Field location

The Große Ohe (Grosse Ohe) River catchment (19.2 km^2) is situated in the Bavarian Forest of Lower Bavaria, Germany, near the border with the Czech Republic. This study was focused on the Hinterer Schachtenbach, a 3.5 km^2 sub-catchment of the Grosse Ohe catchment in the Bavarian Forest (Fig. 3.1). With an average terrain slope of 7.7°, the catchment has been monitored by the Bavarian Forest National Park (BFNP) since 1977 (Beudert & Gietl, 2015). The Hinterer Schachtenbach catchment is subdivided into three sub-catchments: Markungsgraben (MG; 1.10 km^2), Hinterer Schachtenbach sub (HS_{sub}; 1.48 km^2) and Kaltenbrunner Seige (KS; 0.90 km^2). Forests cover almost 98% of the landscape, with Norway spruce (Picea abies, 70%) and European beech (Fagus sylvatica) being the dominant species (Beudert et al., 2015). The catchment spans an elevation range from 1,300 to 770 m above sea level.

Geologically, the catchment is underlain predominantly by biotite granite and cordierite-sillimanite gneiss (Beudert et al., 2015). Across the catchment, fractured bedrock is overlain by sedimentary deposits (Beudert et al., 2015), creating a local aquifer system that includes both fractured-rock and unconsolidated components. Soils are mainly cambisols and podzols, although lithosols, histosols and hydromorphic soils

also occur, with the proportion of these hydromorphic soils varying from about 5% at one monitoring site (MG) to 35% at another (HS) (Beudert et al., 2015).

Annual precipitation in the Grosse Ohe catchment is approximately 1,500 mm. The river is a perennial stream, supported by substantial precipitation within its catchment (Beudert et al., 2015). During summers and periods of drought, it is anticipated that certain stretches of the river might experience a loss of water to the underlying aquifer. During these dry seasons, aquifer-dependent streams may receive less groundwater recharge, resulting in reduced flow or even a temporary cessation of flow.

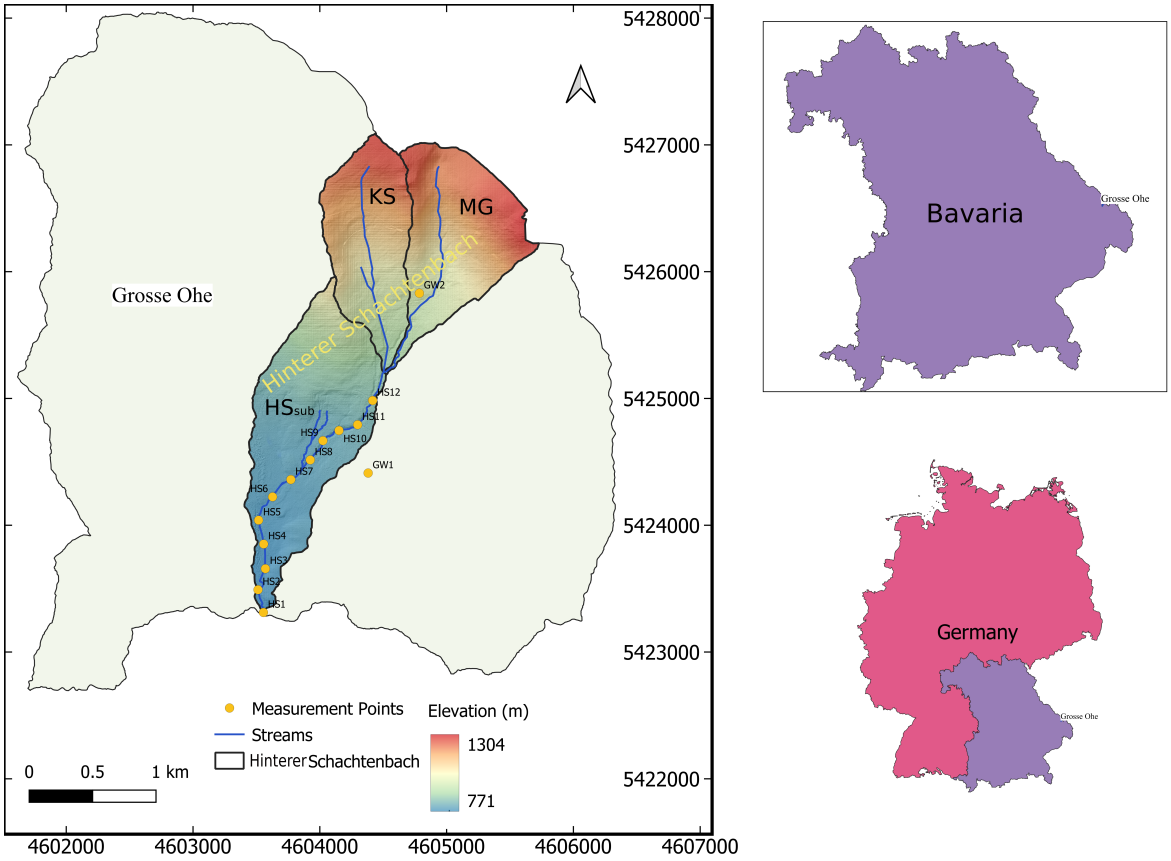


Figure 3.1. Location map of the Grosse Ohe catchment and its sub-catchment Hinterer Schachtenbach. Measurements points showing observation wells (GW1, GW2) for groundwater samples and others denote ^{222}Rn sampling sites. German names (e.g., Große Ohe) are translated to English (e.g., Grosse Ohe) after their first mention.

3.2.2 ^{222}Rn Sampling

Samples were collected along the stream Hinterer Schachtenbach (Figure 3.1) during three field campaigns in June 2018, September 2018 and June 2019. Surface water

samples were collected in the middle of the stream at 12 locations using 1 L bottles. To avoid degassing of ^{222}Rn each sample was filled underwater without leaving any headspace. ^{222}Rn samples were measured in the field within 6 h of sampling using multiple RAD-7 (Durridge Company Inc.) detectors. Before starting the measurement, the air circuit of the detectors were dried (Drierite) to maintain the relative humidity of around 5%. Every sample was counted for 1 hr. For groundwater, samples were collected from two wells which were purged at least three times prior to collection. Each sample was then collected into 250 mL bottles, which were filled from the bottom without leaving headspace.

3.2.3 Modelling

3.2.3.1 Hydrological Model

To represent runoff generation for the sub-catchment, a hydrological model was developed as part of a previous study (Munir et al., 2024). Hydrology was represented using the fully integrated model HGS, capable of simultaneously representing surface and subsurface flow processes as well as interactions between the two flow domains (Therrien et al., 2008). In HGS, a control-volume finite element method is used to solve the governing equations for 3D variably saturated subsurface flow and 2D-depth averaged surface flow. Here, 'depth-averaged' means that hydraulic variables such as velocity and pressure are averaged over the local water depth, so that surface flow is represented in two horizontal dimensions. Coupling between the surface and subsurface flow domain is achieved by using the dual node concept (Therrien et al., 2008). The two-dimensional (2D) mesh for the Grosse Ohe catchment model includes 3,399 nodes and 6,570 triangular elements, while the model for Hinterer Schachtenbach comprises 1,824 nodes and 3,507 triangular elements. To develop a three-dimensional (3D) mesh for the subsurface flow domain, the 2D surface mesh was vertically extended by combining three primary layers: a top layer with a 5 m thickness and middle and bottom layers each of 10 m thickness. The top layer was further divided into several sub-layers,

each 0.5 m thick. To maintain consistency, the same vertical discretization was applied to both models. The completed 3D mesh for the Grosse Ohe catchment consists of 40,788 nodes and 78,840 elements and the sub-catchment mesh includes 21,888 nodes and 42,084 elements. Approximately 5.6% of the total catchment area comprises riparian wetlands. These wetlands were modelled with a hydraulic conductivity (K_{sat}) that decreases exponentially with depth, using the same methodology proposed by Frei et al. (2010).

All boundary nodes at the catchment/sub-catchment interfaces in both the surface and subsurface flow domains were assigned as no-flow boundaries, except for the outlet nodes in the surface flow domain. Nodes representing the impermeable bedrock in the subsurface were similarly assigned no-flow conditions. A critical depth boundary condition was applied to the surface nodes at the outlet of the catchment/sub-catchment, enabling outflow from the surface domain at these points. Uniform daily rates of rainfall and evapotranspiration were imposed as flux boundary conditions across both models in the surface flow domain. The model was calibrated for the hydrological year 2018 (November 1, 2017– October 31, 2018) using available daily runoff data collected at the outlet of the Grosse Ohe catchment. Because of the high computational demands and long simulation runtimes of the catchment model, the calibration was conducted manually. Validation was carried out for the hydrological years 2004-2017. Using a single hydrological year for calibration is a common practice in the application of process-based, fully distributed hydrological models, as demonstrated in previous studies (Cornelissen et al., 2013; De Schepper et al., 2017; Glaser et al., 2016; Kaule & Frei, 2022).

3.2.3.2 Transport model

To represent ^{222}Rn in surface and subsurface flow, a reactive transport model was set up using HGS that is coupled to the hydrological model. Reactive transport of ^{222}Rn in the subsurface flow domain in HGS is represented according to equation 1 (Therrien et

al., 2008). Equation 1 accounts for advective and dispersive transport (first two terms on the left side), as well as the decay and emanation of Rn from the porous media.

$$\frac{\partial \left(\theta_s{}^{222}\ Rn\right)}{\partial t} \ + \ \nabla \cdot (q^{222}Rn) \ - \ \nabla \cdot (\theta_s \, \mathbf{D} \, \nabla^{222}\ Rn) \ = \ -\,\theta_s \, \lambda^{222}\ Rn \ + \ \gamma \quad (1)$$

In Eq. 1, ^{222}Rn [Bq L^{-3}] represents the ^{222}Rn concentration, q [L T^{-1}] is the darcy flow velocity vector derived from solving the 3D Richards equation, θ_s [$-$] is the subsurface volumetric soil water content, D [L^2 T^{-1}] represents the hydrodynamic dispersion (mechanical dispersion + diffusion) tensor, λ [T^{-1}] is the ^{222}Rn decay constant (0.18 day^{-1}) and γ [Bq L^{-3} T^{-1}] is the emanation rate of ^{222}Rn in the porous media. The emanation rate γ was calibrated so that the simulated ^{222}Rn activity concentration at secular equilibrium reproduced the highest groundwater endmember activity measured in wells GW1 and GW2; the calibrated value is given in Table 3.1. γ was held constant throughout the subsurface domain, so the model represents a single, catchment-wide groundwater ^{222}Rn endmember rather than a spatially variable endmember along the stream. This choice is supported by the relatively uniform granite–gneiss lithology of the catchment and its consequences for the estimated exchange fluxes are evaluated in Section 3.4.4.

For the surface flow domain equation 2 (Therrien et al., 2008) was used to represent the reactive transport of ^{222}Rn in the surface flow domain.

$$-\bar{\nabla} \cdot \left(d_o \mathbf{v}_a \ {}^{222}Rn - d_o D_o \bar{\nabla} \ {}^{222}Rn\right) - d_o \left(\lambda + \lambda_{degassing}\right) \ {}^{222}Rn + d_o \Omega_o = \frac{\partial \left(d_o \ {}^{222}Rn\right)}{\partial t} \quad (2)$$

Here v_a [L T^{-1}] is the depth-averaged surface flow velocity vector, D_o [L^2 T^{-1}] represents the hydrodynamic dispersion tensor in surface water, $\lambda_{degassing}$ represents the 1st order

degassing constant [T^{-1}], d_o is the surface water depth [L] and Ω_o is Rn exchange term [M L^{-3} T^{-1}].

To represent the simultaneous transport in both subsurface and surface domains the solute exchange term Ω_o[M L^{-3} T^{-1}] is defined in Eq. 3 (Therrien et al., 2008) as follows:

$$d_o\Omega_o = d_o\Gamma_o C_{ups} + \left(\frac{|d_o\Gamma_o|\,\alpha_c + \theta_s S_w \tau D_{free}}{l_{exch}}\right)(C - C_o) \quad (3)$$

Here [L] represents surface flow water depth, [T^{-1}] represents fluid exchanges with the subsurface domain, the term α_c [L] is the coupling dispersivity between the subsurface and surface, θ_s is volumetric water content/porosity (dimensionless) and $S_w$is water saturation (a fraction between 0 and 1, dimensionless), τ[-] tortuosity factor, D_{free} is the free-solution diffusion coefficient [L^2T^{-1}], l_{exch} [L]is coupling length. Where C [M L^{-3}] is the subsurface concentration and C_o[M L^{-3}] is the surface concentration and the upstream concentration C_{ups} [M L^{-3}] is equal to C when the flow is from the subsurface to the surface (exfiltration) and equal to C_o when the flow is from the surface to the subsurface (infiltration).

3.2.4 Boundary conditions, calibration and simulations

Initially, the model was used to represent the endmember concentration observed in the aquifer of the catchment accurately. This was done by applying the zero-order source (γ) boundary condition to all model elements. The zero-order source condition represents the emanation of ^{222}Rn from the sediments. To establish secular equilibrium in the model, a simulation was conducted using long-term average rainfall as input. The model was run until the change in ^{222}Rn concentration within the subsurface approached zero, ensuring equilibrium conditions. At secular equilibrium under no-flow conditions, Eq. 1 reduces to θ_s λ ^{222}Rn = γ. The calibrated γ of 4,500 Bq m^{-3} d^{-1}, with λ = 0.18 d^{-1} and a mean subsurface water content of θ_s = 0.40, therefore corresponds to a groundwater endmember of approximately 62,500 Bq m^{-3}. Here γ is defined per unit

bulk volume. This value is identical to the highest groundwater activity measured in the two observation wells (62,500 Bq m^{-3} in GW2 on 12 June 2018; Table S3.2). In the surface domain (overland flow), the longitudinal and transverse dispersivities were uniformly set to 100 meters (X and Y direction) in all simulations (Liggett et al., 2015). This was done to minimize numerical oscillations associated with high Peclet numbers due to surface flow velocities. Simulations were performed with subsurface dispersion, using the model's default values for longitudinal and transverse dispersivities in porous media. A decay constant of 0.18 d^{-1} was applied to both surface and subsurface domains and various calibrated 1st-order degassing constants (Table 3.1) were applied to the surface flow domain.

The transport model was calibrated with the ^{222}Rn concentration measured in the surface water samples. The calibration was done by manually adjusting the first-order degassing constants of the surface flow domain. Since degassing is influenced by hydrodynamic flow conditions in the stream (e.g. laminar vs. turbulent flow) as well as meteorological factors such as wind speed and rainfall, varying degassing constants were calibrated to account for the different spatial and temporal conditions observed in the stream. Due to the computationally intensive requirements of the catchment-scale model, calibration of the ^{222}Rn concentrations was performed manually. The calibration of the model was based on ^{222}Rn concentrations measured on June 12, 2018. Further simulation of the model was done using two more measurements of ^{222}Rn concentrations in surface water collected in September 2018 and June 2019.

Table 3.1. Model parameters for the Grosse Ohe catchment.

Parameters	**Porous media**	**Surface domain**
Longitudinal dispersivity α_L (m)	1 [a]	100[b]
Transverse dispersivity α_T (m)	0.1 [a]	100[b]
γ (Bq/m^3/day) (Calibrated)	4,500	-
Degassing constant $\lambda_{Overland}$ (per day) (Calibrated)	-	4.82 & 44.82
λ(per day)	0.18	0.18

Table notes: [a] Therrien et al. (2008); [b] Liggett et al. (2015).

3.3 Results

The hydrological flow model applied here was calibrated and evaluated by Munir et al. (2024). Its Nash-Sutcliffe Efficiency (NSE) for the calibration period was 0.61, indicating satisfactory agreement between observed and modelled discharge. Simulated and observed discharge at the catchment outlet are shown in Figure 3.2 together with the three sampling dates, confirming that all three ^{222}Rn surveys were carried out under low-to-moderate flow. Model accuracy was highest under the low-flow conditions that prevail in summer and early autumn, with an NSE of 0.67 for that interval. Performance was weaker during the winter and spring seasons, particularly during snowmelt periods, which is attributed to limitations in the snowmelt processes represented within HGS, which relies on snowmelt routines adapted from the HBV (Hydrologiska Byråns Vattenbalansavdelning) conceptual rainfall–runoff model. Because the ^{222}Rn transport simulations are driven by the flow fields produced by this model, the weaker winter-season performance propagates into the transport results and is considered further in Section 3.4.4. Building upon this calibrated model, we extended our analysis to simulate the ^{222}Rn concentrations in surface water.

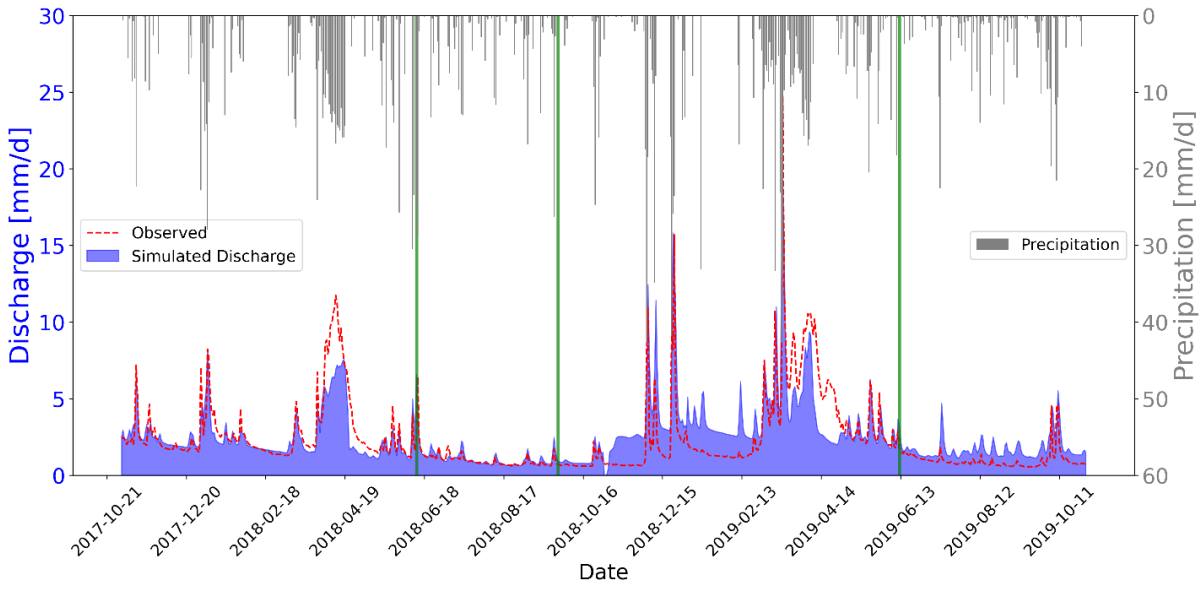


Figure 3.2. Simulated and observed river discharge (1 November 2017 – 31 October 2019), with sampling dates also marked. The green line indicates the sampling events.

3.3.1 Modelled and Observed ^{222}Rn Concentrations

Stream water ^{222}Rn concentrations were measured and simulated at 12 sampling sites (HS1–HS12) during three campaigns: 12 June 2018, 27 September 2018 and 12 June 2019 (Fig. 3.3a–c). The sites are arranged from upstream (HS12) to downstream (HS1) in the combined figure. Positive modelled streambed exchange flux denotes groundwater discharge to the stream, whereas negative flux denotes stream water infiltration and groundwater recharge. The two degassing regimes shown in Fig. 3.3 are calibrated transport-model parameters rather than measured quantities. The fluxes reported below are local streambed exchange fluxes expressed in mm d^{-1}. Measured and simulated ^{222}Rn activity concentrations and modelled streambed exchange fluxes for all 12 sites and all three campaigns are given in Table S3.1.

On 12 June 2018, measured ^{222}Rn concentrations ranged from 158 Bq m^{-3} at HS10 to 1,797 Bq m^{-3} at HS6 (Fig. 3.3a). The simulated concentration at HS6 was 1,273 Bq m^{-3} 29% below the measured value and the modelled streambed exchange flux was +12.8 mm d^{-1}. HS7 had a measured concentration of 1,549 Bq m^{-3} and the largest positive exchange flux of the campaign (+30.8 mm d^{-1}). At HS8, the measured and simulated concentrations were 445 and 96 Bq m^{-3}, respectively and the exchange flux was +2.4 mm d^{-1}. Low measured values at HS10 and HS11 (158 and 166 Bq m^{-3}, respectively) occurred with a near-zero flux at HS10 (+0.13 mm d^{-1}) and a negative flux at HS11 (−3.75 mm d^{-1}). For this calibration campaign, measured and simulated activity concentrations were strongly related across the 12 sites ($R^2 = 0.86$, $p < 0.001$; RMSE = 222 Bq m^{-3}; PBIAS = −10.1%; n = 12).

On 27 September 2018, which had the lowest catchment-outlet runoff of the three sampling dates, measured ^{222}Rn concentrations ranged from 275 Bq m^{-3} at HS10 to 2,888 Bq m^{-3} at HS7 (Fig. 3.3b). Simulated concentrations ranged from 112 Bq m^{-3} at HS8 to 2,275 Bq m^{-3} at HS7. Both maxima therefore occurred at HS7, where the modelled streambed exchange flux was +25.1 mm d^{-1}. HS9 had a positive exchange flux of +24.7

mm d^{-1}, although its measured concentration remained lower than those at HS4–HS7. For this evaluation campaign, measured and simulated activity concentrations were strongly related across the 12 sites ($R^2 = 0.87$, $p < 0.001$; RMSE = 302 Bq m^{-3}; PBIAS = −15.2%; n = 12).

On 12 June 2019, measured ^{222}Rn concentrations ranged from 83 Bq m^{-3} at HS11 to 1,678 Bq m^{-3} at HS7 (Fig. 3.3c). Simulated concentrations ranged from 126 Bq m^{-3} at HS8 to 1,655 Bq m^{-3} at HS7. The measured/simulated difference at HS7 was 23 Bq m^{-3} and the modelled streambed exchange flux was +27.6 mm d^{-1}. At HS8, the measured and simulated concentrations were 459 and 126 Bq m^{-3}, respectively and the exchange flux was −6.6 mm d^{-1}. HS9 remained a groundwater-discharge location, with a positive exchange flux of +19.5 mm d^{-1}, but its measured concentration was again lower than those at HS4–HS7. For this evaluation campaign, measured and simulated activity concentrations were strongly related across the 12 sites ($R^2 = 0.88$, $p < 0.001$; RMSE = 164 Bq m^{-3}; PBIAS = −9.5%; n = 12), the closest agreement of the three campaigns.

Across the three campaigns (Table S3.1), measured and simulated ^{222}Rn concentrations were generally higher at HS4–HS7 and lower at HS8–HS12. HS6 or HS7 contained the measured maximum on every sampling date. The contrast between HS8 and HS9 also persisted. At HS8, measured concentrations were 445, 529 and 459 Bq m^{-3}, whereas the modelled streambed exchange flux changed from slightly positive on 12 June 2018 (+2.4 mm d^{-1}) to negative on 27 September 2018 and 12 June 2019 (−13.9 and −6.6 mm d^{-1}, respectively). By comparison, HS9 had positive modelled exchange fluxes on all three dates (+24.5, +24.7 and +19.5 mm d^{-1}, respectively), despite lower measured concentrations than those at HS4–HS7.

3.3.2 Temporal model results at HS7

HS7 was selected for temporal analysis because it had persistently high measured ^{222}Rn concentrations during the three sampling campaigns. Daily model outputs were exam-

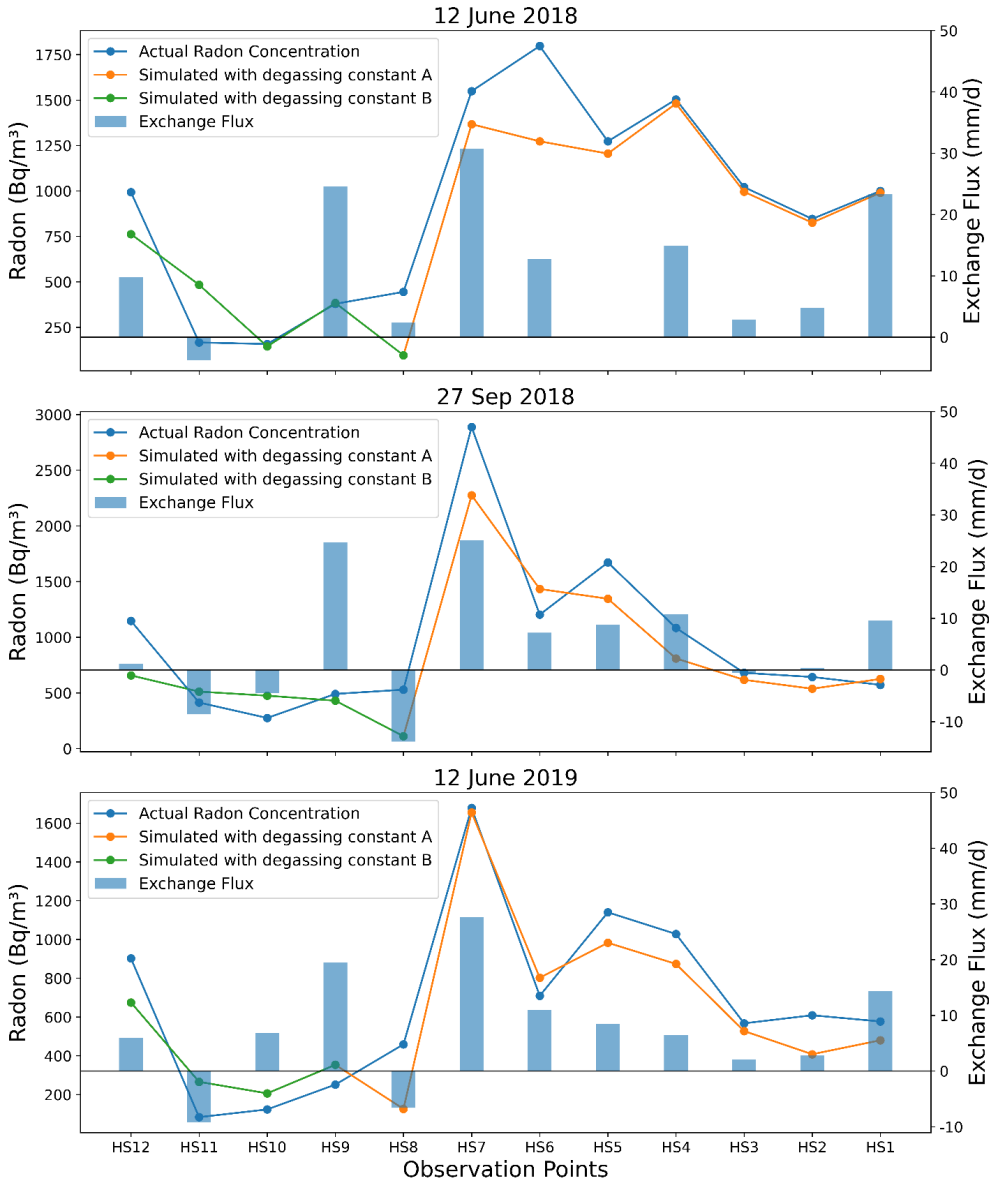


Figure 3.3. Longitudinal measured and simulated stream-water ^{222}Rn concentration and modelled streambed exchange flux at HS1–HS12 for (a) 12 June 2018, (b) 27 September 2018 and (c) 12 June 2019. Sites are plotted from upstream (HS12) to downstream (HS1). Positive exchange flux denotes groundwater discharge to the stream; negative flux denotes stream-water infiltration and groundwater recharge. Regime A denotes the lower calibrated degassing constant used for HS1–HS7 (4.82 d^{-1}); regime B denotes the higher calibrated constant used for HS8–HS12 (44.82 d^{-1}).

ined from 1 November 2017 to 31 October 2019 (Fig. 3.4). The continuous streambed exchange-flux and ^{222}Rn series are model simulations; stream-water ^{222}Rn concentration was measured only on the three dates marked in Fig. 3.4. Modelled streambed exchange flux at HS7 remained positive throughout the simulation period and ranged from +13.0 mm d^{-1} on 13 July 2019 to +33.7 mm d^{-1} on 21 April 2018, with a mean of +20.1 mm d^{-1}. Simulated ^{222}Rn concentrations ranged from 868 Bq m^{-3} on 3 December 2018 to 2,275 Bq m^{-3} on 27 September 2018, with a mean of approximately 1,584 Bq m^{-3}. On 24 April 2018, a local simulated concentration peak of 2,055 Bq m^{-3} occurred with a modelled exchange flux of +27.8 mm d^{-1}. On the three dates marked in Fig. 3.4, modelled exchange fluxes were +30.8, +25.1, and +27.6 mm d^{-1}, with corresponding ^{222}Rn concentrations of 1,367, 2,275, and 1,655 Bq m^{-3} on 12 June 2018, 27 September 2018, and 12 June 2019, respectively.

Both modelled series were generally higher during winter and spring than during summer and early autumn. In January 2018, streambed exchange flux exceeded 30 mm d^{-1} and simulated concentration exceeded 1,900 Bq m^{-3}, whereas in August 2018 exchange flux declined below 15 mm d^{-1} and simulated concentration was approximately 1,100 Bq m^{-3}. Shorter-term variation was also evident during the June 2018 rainfall sequence. Following 30.5 mm of precipitation on 9 June, the simulated concentration decreased from 1,530 Bq m^{-3} on 8 June to 1,116 Bq m^{-3} on 9 June. On 10 June, when precipitation totaled 23.4 mm, the simulated concentration was 1,211 Bq m^{-3}. Because the transport calculation uses streambed exchange flux from the flow solution, co-variation between the two continuous model series represents model behaviour rather than independent evidence for modelled exchange.

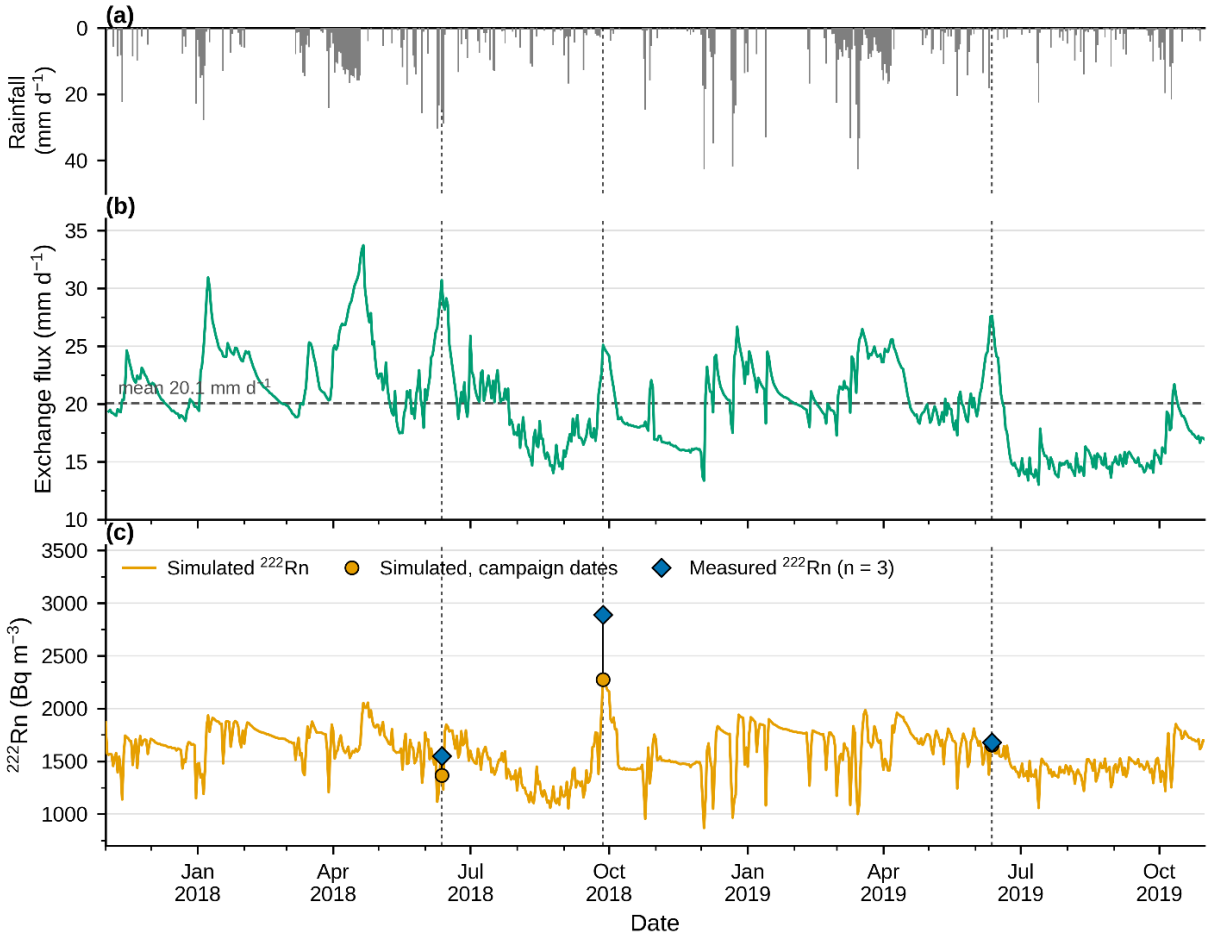


Figure 3.4. Modelled daily streambed exchange flux and ^{222}Rn concentration at HS7, together with observed daily precipitation used as model forcing (grey), from 1 November 2017 to 31 October 2019. Vertical dotted lines denote the three dates on which stream water ^{222}Rn concentration was measured.

3.4 Discussion

3.4.1 Persistent groundwater influence around HS6-HS7

Across the three surveys, stream-water ^{222}Rn showed a consistent longitudinal pattern under different low-to-moderate flow conditions. Measured and simulated concentrations were significantly related in all campaigns, with generally higher values at HS4-HS7 and lower values at HS8-HS12. The HGS flow model that supplied water velocities and streambed exchange fluxes was calibrated against catchment-outlet runoff without using stream-water ^{222}Rn. The June 2018 survey was then used to calibrate the effective degassing constants, whereas the September 2018 and June 2019 surveys evaluated the resulting transport model. Reproduction of the same longitudinal pattern in both

evaluation surveys therefore indicates that the simulated flow field captured the main location of groundwater influence without adjusting the streambed exchange fluxes directly to those surveys. This agreement supports the broader spatial pattern but does not independently validate the exact exchange flux at each site.

The clearest feature was the repeated ^{222}Rn enrichment around HS6-HS7. HS6 contained the maximum measured concentration in June 2018, whereas HS7 contained the measured and simulated maxima in September 2018 and June 2019. HS7 also had positive modelled streambed exchange fluxes during all three surveys, ranging from +25.1 to +30.8 mm d^{-1}. These repeated observations indicate that groundwater influence was concentrated around HS6-HS7 rather than distributed uniformly along the stream. Longitudinal ^{222}Rn surveys have similarly identified spatially restricted groundwater-inflow reaches in subalpine and small headwater streams (Avery et al., 2018; Schubert et al., 2020). Engel et al. (2024) also reproduced a localized ^{222}Rn peak along the River Moselle under two flow conditions, although the inferred groundwater-inflow magnitude depended strongly on the selected endmember.

Repeated measurements under different flow conditions provide stronger support for the HS6-HS7 interpretation than an isolated concentration maximum. In a Bavarian headwater, repeated ^{222}Rn surveys showed persistent spatial differences in groundwater contribution and a larger groundwater fraction during low flow (Kaule & Gilfedder, 2021). Johnson et al. (2024) likewise identified spatially distinct groundwater sources in a mountain headwater, but found that a fractured-bedrock contribution declined through summer while a downstream, higher-storage source remained comparatively stable. The persistence of the HS6-HS7 signal therefore suggests a groundwater source that remained connected to the stream during all three surveys although the available data do not identify the specific geological structure or storage unit contributing that water.

Stream-water ^{222}Rn concentration should not, however, be interpreted as a direct measure of the local groundwater flux. The measured concentration integrates groundwater input, upstream transport, mixing, radioactive decay and atmospheric degassing. Explicit HGS simulations have shown that advection and dispersion between low-^{222}Rn surface water and high-^{222}Rn groundwater can produce tracer patterns that do not correspond simply to one local flow path or flux (Gilfedder et al., 2019). The groundwater endmember and atmospheric evasion are also recognized as major uncertainties in ^{222}Rn-based groundwater-discharge estimates (Adyasari et al., 2023). The present results therefore provide greater confidence in the location and recurrence of groundwater influence around HS6-HS7 than in the exact magnitude of the modelled site-scale exchange fluxes.

3.4.2 Seasonal and rainfall-related behaviour at HS7

The two-year simulation at HS7 places the three surveys within a broader hydrological context. Modelled streambed exchange remained positive throughout the simulation, ranging from +13.0 to +33.7 mm d^{-1} and averaging +20.1 mm d^{-1}. Both the exchange flux and simulated ^{222}Rn concentration were generally higher during winter and spring and lower during summer and early autumn. This pattern is consistent with seasonal recharge and snowmelt entering subsurface storage and sustaining groundwater contributions to mountain streams. Tracer studies in alpine catchments have shown that a substantial fraction of snowmelt can reach streams through subsurface flow paths and that pre-event water may remain important during the melt period (Liu et al., 2004). The simulated seasonal behaviour is also consistent with the recharge and storage dynamics represented previously for this catchment (Munir et al., 2024).

The model produced a marked response during the June 2018 rainfall sequence. Following 30.5 mm of precipitation on 9 June, simulated ^{222}Rn activity concentration decreased from 1,530 to 1,116 Bq m^{-3} and remained below the pre-event value after a further 23.4 mm of rainfall on 10 June. Such a decrease may reflect dilution by rainfall,

surface runoff, or shallow subsurface water with low ^{222}Rn concentration, together with changes in the relative contributions of shallow and deeper flow paths. This interpretation is consistent with the lower groundwater fraction observed at increasing discharge in a Bavarian headwater (Kaule & Gilfedder, 2021) and with seasonal changes in groundwater sources and rapid responses to summer precipitation in a fractured mountain catchment (Johnson et al., 2024).

Rainfall may also alter hydraulic gradients and groundwater discharge rather than producing dilution alone (Poulsen et al., 2015; He et al., 2022). Continuous ^{222}Rn and electrical-conductivity measurements in a groundwater-connected wetland showed that storms activated local groundwater flow paths and rapidly changed groundwater discharge, although the calculated response was sensitive to the treatment of atmospheric gas exchange (Gilfedder et al., 2015). Explicit HGS simulations have similarly shown that transient hydraulic gradients and mixing between surface water and groundwater can produce rapid ^{222}Rn changes during bank storage and return flow (Gilfedder et al., 2019). The HS7 rainfall response should nevertheless be interpreted cautiously because both continuous series are model outputs, stream-water ^{222}Rn was measured only during the three surveys and the simulated tracer series is partly driven by the exchange flux supplied by the flow model. Their co-variation therefore represents model behaviour rather than two independent lines of evidence.

3.4.3 Local differences between streambed exchange and stream-water ^{222}Rn

The contrasting results at HS8 and HS9 show that local streambed exchange alone cannot explain all of the observed tracer variation. HS9 had positive modelled exchange fluxes during all three surveys, ranging from +19.5 to +24.7 mm d^{-1}, but its measured ^{222}Rn concentrations remained lower than those at HS4-HS7. HS8 showed the opposite behaviour: measured concentrations remained moderate even when the model simulated negative streambed exchange in September 2018 and June 2019. A positive local

groundwater flux therefore does not necessarily produce an immediate or proportional increase in stream-water ^{222}Rn at the same sampling site.

One explanation is that the concentration measured at a site includes tracer transported from upstream. Groundwater entering an upstream reach may retain an observable signal farther downstream, whereas locally discharging groundwater may be diluted or degassed before sampling. Dispersion and mixing can also smooth, shift, or weaken local concentration peaks. Gilfedder et al. (2019) showed that two-dimensional flow fields generated neighbouring zones with contrasting ^{222}Rn concentrations because of local downwelling, upwelling and dispersive mixing. Although their study concerned hyporheic and bank-storage systems, it demonstrates why stream-water ^{222}Rn need not vary in direct proportion to one local exchange flux.

Atmospheric degassing may also contribute to the upstream-downstream contrast. The calibrated effective degassing constants were substantially higher for HS8-HS12 than for HS1-HS7. Greater gas loss in the upstream channel is hydrologically plausible because gas-transfer velocity can vary strongly over short distances and is related to current velocity and turbulence (Kokic et al., 2018). Direct tracer-gas measurements in a subalpine stream also showed that degassing had to be constrained before groundwater inflow could be quantified from ^{222}Rn (Avery et al., 2018). However, neither gas-transfer velocity nor the reach-scale hydraulic conditions controlling it were measured here, so the calibrated constants should be treated as effective reach parameters rather than direct measurements of atmospheric ^{222}Rn loss.

Spatial variation in the groundwater ^{222}Rn source provides another possible explanation. The broadly similar granite-gneiss bedrock provides a practical first-order basis for a common source representation, but it does not exclude local differences in mineral composition, weathering, fractures, residence time, or the contributions of shallow and deeper flow paths. The HS8 and HS9 responses may therefore reflect different combinations of upstream transport, degassing, groundwater-source variability, mixing

and unresolved local flow paths. The current observations do not distinguish among these alternatives and there is no direct field evidence for assigning either anomaly to a particular wetland, seep, fracture, or tributary.

3.4.4 Endmember assumptions, model uncertainty and further measurements

The main tracer uncertainty concerns the groundwater ^{222}Rn source. The catchment is dominated by granite and gneiss, with no major contrast in mapped lithology along the studied stream. Because bedrock lithology and mineralogy strongly influence groundwater ^{222}Rn, this setting provides a reasonable basis for applying a spatially uniform emanation rate, γ (Grande & Moran, 2021). However, a uniform γ does not imply that groundwater ^{222}Rn was identical throughout the catchment. Groundwater radon can vary within crystalline bedrock because of differences in mineralogy, weathering, fractures, residence time and the mixing of shallow and deeper groundwater (Sukanya et al., 2021). As groundwater ^{222}Rn was measured in only two wells, this spatial variability could not be assessed directly.

The adopted groundwater endmember of 62,500 Bq m^{-3} was the highest of the four activities measured in GW1 and GW2 and was 9.8% above their arithmetic mean of 56,919.5 Bq m^{-3} (Table S3.2). This is a conservative choice in the sense that it maximizes the stream-water activity produced by a given exchange flux. Even so, the model under-predicted measured stream ^{222}Rn by 9.5 to 15.2% in the three campaigns. The systematic under-prediction therefore cannot be attributed to an endmember set too low, and more probably reflects either an overestimate of the effective degassing rate or groundwater discharging along the studied reach with a higher activity than that sampled in the two available wells.

With the hydrological solution held fixed, changing the groundwater ^{222}Rn source affects simulated tracer concentrations but does not alter the hydraulic streambed exchange fluxes. Source variability instead affects how strongly the tracer observations

support those flux estimates. Studies that infer groundwater inflow directly from tracer concentrations have shown that different source representations can produce different flux estimates (Peel et al., 2022; Engel et al., 2024). The repeated enrichment at HS6–HS7 is therefore more reliable as evidence of the location of groundwater influence than as a measure of its exact flux. The calibrated degassing constants introduce a related uncertainty. Both the groundwater endmember and gas-transfer rate are difficult to constrain in small, turbulent headwater streams (Schubert et al., 2020). Because gas transfer was not measured directly, the relative effects of groundwater discharge, mixing, upstream transport and atmospheric loss cannot be separated fully, particularly at HS8 and HS9.

The hydrological observations also provide limited information on local streambed exchange. Model evaluation was based on catchment-outlet runoff, which constrains the catchment water balance but not the hydraulic gradients along individual stream reaches. The model reproduced baseflow and recession periods more closely than winter and spring runoff peaks and no high-flow ^{222}Rn survey was available. Reach scale streamflow, groundwater heads, seepage and specific conductance were also not measured. Comparisons of hydraulic, tracer and groundwater model estimates have shown that both the direction and magnitude of groundwater stream exchange may remain uncertain where near stream hydraulic heads are poorly constrained (Bouchez et al., 2021). The reported site scale exchange fluxes should therefore be interpreted as model estimates rather than independent field measurements.

Further measurements should focus on HS6–HS9. Additional groundwater ^{222}Rn samples from wells, springs, or streambed piezometers would test whether the groundwater source varies along the stream. Differential streamflow measurements, near-stream groundwater heads, seepage measurements and specific conductance would provide independent evidence of gaining and losing conditions. Direct gas-transfer measurements and a high flow ^{222}Rn survey would help separate groundwater input from

atmospheric loss, while snow depth and snow water equivalent observations would improve the evaluation of winter and spring flow. Combining these data with sensitivity analysis would better constrain the magnitude of streambed exchange. Until such observations are available, the strongest conclusion is that groundwater influence was repeatedly concentrated around HS6–HS7, whereas the exact exchange rates and the responses at HS8–HS9 remain less certain.

3.5 Conclusions

This study combined ^{222}Rn measurements with a fully integrated flow and transport model to examine groundwater discharge to a Central European headwater stream. Simulated and measured stream-water ^{222}Rn concentrations were significantly related in all three sampling campaigns, and the model reproduced the dominant longitudinal pattern of higher concentrations at HS4–HS7 and lower concentrations at HS8–HS12 in the two campaigns that were not used for calibration.

The clearest result is the repeated ^{222}Rn enrichment around HS6–HS7, which was present under three different low-to-moderate flow conditions and coincided with persistent positive modelled streambed exchange. Groundwater influence along this reach is therefore spatially concentrated rather than uniformly distributed. The two-year simulation at HS7 indicates higher exchange and higher ^{222}Rn during winter and spring than during summer and early autumn, which is consistent with seasonal recharge sustaining groundwater contributions, although stream-water ^{222}Rn was measured on only three dates and the continuous series are model output.

The approach nevertheless shows that coupling a distributed flow and transport model with repeated longitudinal tracer surveys can locate persistent groundwater-discharge zones within a headwater catchment. This is relevant for identifying the reaches whose streamflow depends most strongly on groundwater during dry periods, and for targeting the further measurements needed to quantify that dependence.

Acknowledgments

This work was supported by the Bavarian State Ministry of Science and the Arts in the Bavarian Climate Research Network (bayklif). The authors would like to thank the Bavarian Forest National Park administration, for providing physiographic and meteorological data. The authors would also like to thank Burkhard Beudert for providing assistance in the Bavarian Forest National Park. The authors also thank the Higher Education Commission of Pakistan (HEC) for the scholarship funds jointly provided by the German Academic Exchange Service (DAAD).

Funding

This work was supported by the Bavarian State Ministry of Science and the Arts in the Bavarian Climate Research Network (bayklif).

Data Availability Statement

The data that support the findings of this study are available from the corresponding author upon reasonable request.

References

Adyasari, D., Dimova, N.T., Dulai, H., Gilfedder, B.S., Cartwright, I., McKenzie, T., Fuleky, P., 2023. Radon-222 as a groundwater discharge tracer to surface waters. Earth-Sci. Rev. 238, 104321.

Avery, E., Bibby, R., Visser, A., Esser, B., Moran, J., 2018. Quantification of groundwater discharge in a subalpine stream using radon-222. Water 10 (2), 100.

Bennett, K.E., Werner, A.T., Schnorbus, M., 2012. Uncertainties in hydrologic and climate change impact analyses in headwater basins of British Columbia. J. Clim. 25, 5711–5730.

Beudert, B., Gietl, G., 2015. Long-term monitoring in the Große Ohe catchment, Bavarian Forest National Park. Silva Gabreta 21 (1), 5–27.

Beudert, B., Bässler, C., Thorn, S., Noss, R., Schröder, B., Dieffenbach-Fries, H., Foullois, N., Müller, J., 2015. Bark beetles increase biodiversity while maintaining drinking water quality. Conserv. Lett. 8, 272–281.

Bouchez, C., Cook, P.G., Partington, D., Simmons, C.T., 2021. Comparison of surface water-groundwater exchange fluxes derived from hydraulic and geochemical methods and a regional groundwater model. Water Resour. Res. 57 (3), e2020WR029137.

Brunke, M., Gonser, T., 1997. The ecological significance of exchange processes between rivers and groundwater. Freshw. Biol. 37, 1–33.

Burnett, W.C., Dulaiova, H., 2003. Estimating the dynamics of groundwater input into the coastal zone via continuous radon-222 measurements. J. Environ. Radioact. 69, 21–35.

Cartwright, I., Hofmann, H., Sirianos, M.A., Weaver, T.R., Simmons, C.T., 2011. Geochemical and ^{222}Rn constraints on baseflow to the Murray River, Australia, and timescales for the decay of low-salinity groundwater lenses. J. Hydrol. 405, 333–343.

Cecil, L.D., Green, J.R., 2000. Radon-222. In: Environmental Tracers in Subsurface Hydrology. Springer, Boston, MA, pp. 175–194.

Chen, X., 2007. Hydrologic connections of a stream-aquifer-vegetation zone in south-central Platte River valley, Nebraska. J. Hydrol. 333, 554–568.

Cornelissen, T., Diekkrüger, B., Bogena, H., 2013. Using HydroGeoSphere in a forested catchment: How does spatial resolution influence the simulation of spatio-temporal soil moisture variability? Procedia Environ. Sci. 19, 198–207.

Cranswick, R.H., Cook, P.G., Lamontagne, S., 2014. Hyporheic zone exchange fluxes and residence times inferred from riverbed temperature and radon data. J. Hydrol. 519, 1870–1881.

De Schepper, G., Therrien, R., Refsgaard, J.C., He, X., Kjaergaard, C., Iversen, B.V., 2017. Simulating seasonal variations of tile drainage discharge in an agricultural catchment. Water Resour. Res. 53, 3896–3920.

Dimova, N.T., Burnett, W.C., Chanton, J.P., Corbett, J.E., 2013. Application of radon-222 to investigate groundwater discharge into small shallow lakes. J. Hydrol. 486, 112–122.

Ellins, K.K., Roman-Mas, A., Lee, R., 1990. Using ^{222}Rn to examine groundwater/surface-water interaction in the Rio Grande de Manatí, Puerto Rico. J. Hydrol. 115, 319–341.

Engel, M., Mischel, S., Quanz, S., Frei, S., Radny, D., Voelpel, R., Schmidt, A., 2024. Localizing and quantifying groundwater-surface water interactions at different scales: A tracer approach at the River Moselle, Germany. Hydrol. Process. 38 (5), e15118.

Faybishenko, B., 2010. Fuzzy-probabilistic calculations of water-balance uncertainty. Stoch. Environ. Res. Risk Assess. 24, 939–952.

Fleckenstein, J.H., Krause, S., Hannah, D.M., Boano, F., 2010. Groundwater-surface water interactions: New methods and models to improve understanding of processes and dynamics. Adv. Water Resour. 33, 1291–1295.

Frei, S., Gilfedder, B.S., 2021. Quantifying residence times of bank filtrate: A novel framework using radon as a natural tracer. Water Res. 201, 117376.

Frei, S., Lischeid, G., Fleckenstein, J.H., 2010. Effects of micro-topography on surface-subsurface exchange and runoff generation in a virtual riparian wetland: A modeling study. Adv. Water Resour. 33, 1388–1401.

Genereux, D.P., Hemond, H.F., Mulholland, P.J., 1993. Use of radon-222 and calcium as tracers in a three-end-member mixing model for streamflow generation on the West Fork of Walker Branch Watershed. J. Hydrol. 142, 167–211.

Gilfedder, B.S., Frei, S., Hofmann, H., Cartwright, I., 2015. Groundwater discharge to wetlands driven by storm and flood events: Quantification using continuous radon-222 and electrical conductivity measurements and dynamic mass-balance modelling. Geochim. Cosmochim. Acta 165, 161–177.

Gilfedder, B.S., Cartwright, I., Hofmann, H., Frei, S., 2019. Explicit modeling of radon-222 in HydroGeoSphere during steady state and dynamic transient storage. Groundwater 57 (1), 36–47.

Glaser, B., Klaus, J., Frei, S., Frentress, J., Pfister, L., Hopp, L., 2016. On the value of surface saturated area dynamics mapped with thermal infrared imagery for modeling the hillslope-riparian-stream continuum. Water Resour. Res. 52, 8317–8342.

Grande, E., Moran, J.E., 2021. Patterns in radon activity in California groundwater. ACS ES&T Water 1 (11), 2390–2402.

He, X., Zhou, H., Wan, J., Guo, Y., Zhao, H., 2022. The effects of rainfall on groundwater hydrogeochemistry and chemical weathering. Environ. Sci. Pollut. Res. 30, 12152–12168.

Hofmann, H., Gilfedder, B.S., Cartwright, I., 2011. A novel method using a silicone diffusion membrane for continuous ^{222}Rn measurements for the quantification of groundwater discharge to streams and rivers. Environ. Sci. Technol. 45, 8915–8921.

Jia, S., Dai, Z., Du, X., Meng, B., Yang, Z., Lan, T., 2021. Quantitative evaluation of groundwater and surface water interaction characteristics during a dry season. Water Environ. J. 35, 1348–1361.

Johnson, K., Christensen, J.N., Gardner, W.P., Sprenger, M., Li, L., Williams, K.H., Carroll, R.W.H., Thiros, N.E., Brown, W.S., Beutler, C.A., Newman, A., Sullivan, P.L., 2024. Shifting groundwater fluxes in bedrock fractures: Evidence from stream water radon and water isotopes. J. Hydrol. 635, 131202.

Kaule, L., Frei, S., 2022. Analysis of drought conditions and their impacts in a headwater stream in the Central European lower mountain ranges. Reg. Environ. Change 22, 82.

Kaule, R., Gilfedder, B.S., 2021. Groundwater dominates water fluxes in a headwater catchment during drought. Front. Water 3, 706932.

Kokic, J., Sahlée, E., Sobek, S., Vachon, D., Wallin, M.B., 2018. High spatial variability of gas transfer velocity in streams revealed by turbulence measurements. Inland Waters 8 (4), 461–473.

Krabbenhoft, D.P., Webster, K.E., 1995. Transient hydrogeological controls on the chemistry of a seepage lake. Water Resour. Res. 31, 2295–2305.

Liggett, J.E., Partington, D., Frei, S., Werner, A.D., Simmons, C.T., Fleckenstein, J.H., 2015. An exploration of coupled surface-subsurface solute transport in a fully integrated catchment model. J. Hydrol. 529, 969–979.

Liu, F., Williams, M.W., Caine, N., 2004. Source waters and flow paths in an alpine catchment, Colorado Front Range, United States. Water Resour. Res. 40, W09401.

McCallum, J.L., Cook, P.G., Berhane, D., Rumpf, C., McMahon, G.A., 2012. Quantifying groundwater flows to streams using differential flow gaugings and water chemistry. J. Hydrol. 416–417, 118–132.

Munir, M.U., Blaurock, K., Frei, S., 2024. Understanding the vulnerability of surface-groundwater interactions to climate change: Insights from a Bavarian Forest headwater catchment. Environ. Earth Sci. 83, 12.

Ortega, L., Manzano, M., Custodio, E., Hornero, J., Rodríguez-Arévalo, J., 2015. Using ^{222}Rn to identify and quantify groundwater inflows to the Mundo River (SE Spain). Chem. Geol. 395, 67–79.

Peel, M., Kipfer, R., Hunkeler, D., Brunner, P., 2022. Variable ^{222}Rn emanation rates in an alluvial aquifer: Limits on using ^{222}Rn as a tracer of surface water-groundwater interactions. Chem. Geol. 599, 120829.

Petermann, E., Gibson, J.J., Knöller, K., Pannier, T., Weiß, H., Schubert, M., 2018a. Determination of groundwater discharge rates and water residence time of groundwater-fed lakes by stable isotopes of water (^{18}O, ^{2}H) and radon (^{222}Rn) mass balances. Hydrol. Process. 32, 805–816.

Petermann, E., Knöller, K., Rocha, C., Scholten, J., Stollberg, R., Weiß, H., Schubert, M., 2018b. Coupling end-member mixing analysis and isotope mass balancing (^{222}Rn) for differentiation of fresh and recirculated submarine groundwater discharge into Knysna Estuary, South Africa. J. Geophys. Res. Oceans 123, 952–970.

Petpongpan, C., Ekkawatpanit, C., Bailey, R.T., Kositgittiwong, D., Saraphirom, P., 2022. Evaluating surface water-groundwater interactions in consequence of changes in climate and groundwater extraction. Water Resour. Manag. 36, 5767–5783.

Pham, Q.N., Tran, T.L., Dang, D.N., 2024. Enhancing hydrological insight: Isotopic methods revealing groundwater-surface water interactions in the Lower Quang Tri River Group, Vietnam. Isot. Environ. Health Stud. 60, 309–330.

Pittroff, M., Frei, S., Gilfedder, B.S., 2017. Quantifying nitrate and oxygen reduction rates in the hyporheic zone using ^{222}Rn to upscale biogeochemical turnover in rivers. Water Resour. Res. 53, 563–579.

Poulsen, J.R., Sebok, E., Duque, C., Tetzlaff, D., Engesgaard, P., 2015. Detecting groundwater discharge dynamics from point-to-catchment scale in a lowland stream: Combining hydraulic and tracer methods. Hydrol. Earth Syst. Sci. 19, 1871–1886.

Qin, W., Han, D., Song, X., Liu, S., 2021. Environmental isotopes (δ^{18}O, δ^{2}H, ^{222}Rn) and hydrochemical evidence for understanding rainfall-surface water-groundwater transformations in a polluted karst area. J. Hydrol. 592, 125748.

Rosenberry, D.O., Engesgaard, P., Hatch, C., 2021. Hydraulic conductivity can no longer be considered a fixed property when quantifying flow between groundwater and surface water. Hydrol. Process. 35, e14226.

Šanda, M., Vitvar, T., Kulasová, A., Jankovec, J., Císlerová, M., 2014. Run-off formation in a humid, temperate headwater catchment using a combined hydrological, hydrochemical and isotopic approach (Jizera Mountains, Czech Republic). Hydrol. Process. 28, 3217–3229.

Schmidt, A., Santos, I.R., Burnett, W.C., Niencheski, F., Knöller, K., 2011. Groundwater sources in a permeable coastal barrier: Evidence from stable isotopes. J. Hydrol. 406, 66–72.

Schubert, M., Knöller, K., Müller, C., Gilfedder, B., 2020. Investigating river water/groundwater interaction along a rivulet section by ^{222}Rn mass balancing. Water 12 (11), 3027.

Schubert, M., Knoeller, K., Scholten, J., Daesslé, L.W., Reyes Bravo, M.M., Chávez Solís, E.M., 2023. Quantification of groundwater discharge into a shallow coastal lagoon applying a multi-tracer approach. Environ. Monit. Assess. 195, 601.

Shanafield, M., Cook, P.G., 2014. Transmission losses, infiltration and groundwater recharge through ephemeral and intermittent streambeds: A review of applied methods. J. Hydrol. 511, 518–529.

Shaw, G.D., Conklin, M.H., Nimz, G.J., Liu, F., 2014. Groundwater and surface water flow to the Merced River, Yosemite Valley, California: ^{36}Cl and Cl^- evidence. Water Resour. Res. 50, 1943–1959.

Sophocleous, M., 2002. Interactions between groundwater and surface water: The state of the science. Hydrogeol. J. 10, 52–67.

Sukanya, S., Noble, J., Joseph, S., 2021. Factors controlling the distribution of radon (^{222}Rn) in groundwater of a tropical mountainous river basin in southwest India. Chemosphere 263, 128096.

Therrien, R., McLaren, R.G., Sudicky, E.A., Panday, S.M., 2008. HydroGeoSphere: A three-dimensional numerical model describing fully integrated subsurface and surface flow and solute transport. Groundwater Simulations Group, University of Waterloo, Waterloo, ON, Canada.

Unland, N.P., Cartwright, I., Andersen, M.S., Rau, G.C., Reed, J., Gilfedder, B.S., Atkinson, A.P., Hofmann, H., 2013. Investigating the spatio-temporal variability in groundwater and surface water interactions: A multi-technique approach. Hydrol. Earth Syst. Sci. 17, 3437–3453.

Usman, M.N., Leandro, J., Broich, K., Disse, M., 2024. Multi-objective calibration and uncertainty analysis for the event-based modelling of flash floods. Hydrol. Sci. J. 69 (4), 456–473.

Vlach, V., Ledvinka, O., Matouskova, M., 2020. Changing low flow and streamflow drought seasonality in Central European headwaters. Water 12 (12), 3575.

Yang, J., Yu, Z., Yi, P., Aldahan, A., 2018. Assessment of groundwater quality and ^{222}Rn distribution in the Xuzhou region, China. Environ. Monit. Assess. 190 (9), 549.

Yang, N., Zhou, P., Wang, G., Zhang, B., Shi, Z., Liao, F., Li, B., Chen, X., Guo, L., Dang, X., Gu, X., 2021. Hydrochemical and isotopic interpretation of interactions between surface water and groundwater in Delingha, Northwest China. J. Hydrol. 598, 126243.

Yuan, R., Wang, M., Wang, S., Song, X., 2020. Water transfer imposes hydrochemical impacts on groundwater by altering the interaction of groundwater and surface water. J. Hydrol. 583, 124617.

Zhao, D., Wang, G., Liao, F., Yang, N., Jiang, W., Guo, L., Liu, C., Shi, Z., 2018. Groundwater-surface water interactions derived by hydrochemical and isotopic (^{222}Rn, deuterium, oxygen-18) tracers in the Nomhon area, Qaidam Basin, NW China. J. Hydrol. 565, 650–661.

Supplementary Material

Table S3.1. Measured and simulated stream-water ^{222}Rn activity concentrations and modelled streambed exchange fluxes at HS1–HS12 during the three sampling campaigns.

Site	12 June 2018			27 September 2018			12 June 2019		
	Measured ^{222}Rn (Bq m^{-3})	Simulated ^{222}Rn (Bq m^{-3})	Exchange flux (mm d^{-1})	Measured ^{222}Rn (Bq m^{-3})	Simulated ^{222}Rn (Bq m^{-3})	Exchange flux (mm d^{-1})	Measured ^{222}Rn (Bq m^{-3})	Simulated ^{222}Rn (Bq m^{-3})	Exchange flux (mm d^{-1})
HS1	1000.0	990.3	23.30	572.7	625.6	9.55	576.9	479.9	14.38
HS2	846.2	825.5	4.79	643.4	537.9	0.42	608.8	407.8	2.78
HS3	1021.0	995.3	2.90	680.4	617.9	−0.55	567.3	527.4	2.09
HS4	1503.5	1480.6	14.87	1083.9	809.9	10.76	1028.0	873.6	6.41
HS5	1272.7	1205.4	−0.10	1671.3	1345.8	8.72	1139.9	982.8	8.45
HS6	1797.2	1273.0	12.78	1202.8	1433.5	7.19	709.1	802.5	10.93
HS7	1549.0	1367.2	30.75	2888.1	2274.8	25.10	1678.3	1654.9	27.61
HS8	444.8	96.3	2.38	529.4	111.7	−13.88	458.7	125.8	−6.63
HS9	379.0	383.8	24.54	491.4	430.8	24.70	251.0	353.2	19.46
HS10	158.0	145.0	0.13	275.3	475.6	−4.45	123.1	206.0	6.81
HS11	166.4	483.7	−3.75	414.0	512.0	−8.60	83.2	265.5	−9.21
HS12	993.0	762.6	9.81	1146.9	657.5	1.21	902.1	674.7	5.92

Notes: Measured and simulated ^{222}Rn values are activity concentrations. Regime A (degassing constant = 4.82 d^{-1}) was applied at HS1–HS7, and regime B (44.82 d^{-1}) at HS8–HS12. Positive exchange flux denotes groundwater discharge to the stream; negative flux denotes stream-water infiltration and groundwater recharge. Exchange fluxes were converted from m d^{-1} to mm d^{-1}.

Table S3.2. Measured ^{222}Rn activity concentrations in deep groundwater samples from observation wells GW1 and GW2.

Observation well	**12 June 2018 (Bq m^{-3})**	**12 June 2019 (Bq m^{-3})**
GW1	56,000	56,801
GW2	62,500	52,377

Note: These groundwater measurements informed the ^{222}Rn endmember used in the transport model.

4 Manuscript III: Using Physics-Informed Neural Networks to Quantify Submarine Groundwater Discharge under High-Frequency Tidal Dynamics Using Heat as a Tracer

Outline

Abstract . . . 120
4.1 Introduction . . . 120
4.2 Materials and Procedures . . . 125
4.2.1 The heat transport equation . . . 125
4.2.2 Physics informed neural network . . . 126
4.3 Assessment . . . 128
4.3.1 Hyperparameter optimization . . . 129
4.3.2 Case Study 1: Step-function . . . 130
4.3.3 Case Study 2: Tidal pumping . . . 134
4.3.4 Case Study 3: Tidal creek system . . . 136
4.4 Discussion . . . 144
4.5 Comments and Recommendations . . . 146
References . . . 148

Bibliographic Information

Frei, S., Munir, M. U., Seiverth, A. M., and Gilfedder, B. S. (2026): Using physics-informed neural networks to quantify submarine groundwater discharge under high-frequency tidal dynamics using heat as a tracer. *Limnology and Oceanography: Methods*, 24(2), Article e70015.

Article Adaptation

The contents of the original version were slightly modified for inclusion in this dissertation, including adjustments to the numbering of sections, figures, tables, and equations. The published version of this article can be found at https://doi.org/10.1002/lom3.70015

Abstract

Estimating exchange rates of submarine groundwater discharge (SGD) at high temporal resolution over extended periods remains challenging, particularly when using heat as a tracer in highly dynamic environments such as tidal systems. Currently available heat transport models struggle to accurately quantify SGD exchange rates in these settings, where sharp transitions and high-frequency fluctuations in hydrodynamic forcings cannot be reproduced with current inverse optimization methods. This study evaluates the ability of Physics-Informed Neural Networks (PINNs) to overcome these limitations through inverse modeling of temperature derived Darcy fluxes. Three case studies—a synthetic step-function transition, a synthetic tidal pumping scenario, both published datasets, and measurements from a field-scale tidal creek (Texel, Netherlands)—were used to test and validate the PINN approach. Unlike conventional methods such as VFLUX and 1DTEMPRO, which exhibited delays and inaccuracies when tidal cycles influence groundwater fluxes on sub-daily to daily frequencies, the PINN successfully predicted exchange fluxes driven by the K1 (24-h) and M2 (12-h) tidal cycles with a high degree of accuracy. Spectral analysis confirmed the PINNs ability to precisely estimate the impact of multi-scale tidal signals on SGD dynamics at a sub-daily resolution. This work highlight PINN as a powerful inversion method when using heat as a tracer in highly dynamic environments, offering new insights into the complex interplay between tidal signals and SGD in coastal systems.

4.1 Introduction

Submarine groundwater discharge (SGD) is a critical component of global water and nutrient cycles, linking terrestrial and marine systems. It accounts for approximately 0.6–1% of the total global freshwater input into the oceans, although these percentages can be much higher on local to regional scales (Luijendijk et al. 2020; Zhou et al. 2019). Local freshwater availability from SGD is important for coastal biodiversity and species richness (Lirman et al. 2003) and has a significant influence on meiofaunal communities

(Grzelak et al. 2018; Kotwicki et al. 2014). Coastal ecosystems, such as estuaries (Santos et al. 2012; Slomp and Van Cappellen 2004), coral reefs (Paytan et al. 2006; Silbiger et al. 2020), and mangroves (Duarte and Cebrián 1996), are nutrient-limited systems and inputs from SGD represent an important source for nitrogen, phosphorus, iron, silica, dissolved organic and inorganic carbon. These nutrient inputs can create favorable conditions for biodiversity hotspots, enhancing food web complexity, and ecosystem productivity (Lecher and Mackey 2018; Luijendijk et al. 2020).

However, nutrient inputs from SGD are also frequently associated with ecosystem degradation in marine environments. Excessive nutrient availability from subterranean terrestrial sources can lead to the uncontrolled growth of phytoplankton and cyanobacteria (Glibert et al. 2012; Howarth and Marino 2006; Paerl 2009; Paerl and Otten 2013) as well as macroalgae (Duarte 1995; McGlathery 2001; Teichberg et al. 2008; Valiela et al. 1997). Harmful algal blooms are a consequence of eutrophication, often triggering cascading effects on marine ecosystems, including large-scale hypoxic events (Diaz and Rosenberg 2008; Rabalais et al. 2002) and the release of toxic substances (e.g., cyanotoxins from cyanobacterial blooms) (Landsberg 2002; Paerl and Otten 2013). These processes can ultimately lead to mass mortality of marine organisms, as has been observed in the Mississippi River estuary in the Gulf of Mexico since the 1950s (Rabalais et al. 2002). Eutrophication of coastal areas is particularly prevalent in regions experiencing intensive anthropogenic activities (e.g., high population density, intensive agriculture and industry), especially along the coastlines of Southeast Asia, North and Central America, and Northern Europe (Beusen et al. 2013).

Quantifying SGD and associated nutrient fluxes in time and space is challenging due to various factors related to its complex nature and the difficulty of measuring groundwater flow in coastal and marine environments. Submarine groundwater discharge can be highly heterogeneous, occurring over large and often poorly defined areas. It can be seasonally variable, and on shorter timescales influenced by tidal cycles, wave dy-

namics and storm events (Taniguchi et al. 2019). Submarine groundwater discharge can range from diffuse seepage over broad areas to more focused discharge at specific points (springs, fractures, etc.) (Burnett et al. 2006; Tsabaris et al. 2021). Unlike surface water inflow (e.g., rivers and streams), SGD cannot be easily measured directly (seepage meters are error-prone and difficult to deploy under long-term conditions), requiring indirect quantification methods such as anthropogenic (e.g., fluorescent dyes, pharmaceuticals) or environmental tracers (e.g., heat, radon, radium, methane, stable isotopes), hydraulic gradient measurements or groundwater flow modeling (Dulaiova et al. 2010).

Using heat as a tracer offers several advantages over the other existing methods: (1) Heat is naturally present in both subsurface and surface environments, allowing for the quantification of bidirectional exchange fluxes. (2) Temperature time series can be collected relatively easily and cost-effectively using commercially available or self-constructed sondes containing thermistors or thermocouples combined with loggers that can be deployed directly in the field over long time periods (weeks to months). (3) Heat can serve as a tracer to quantify bi-directional exchange rates (infiltration and exfiltration) between surface water and groundwater. (4) The physical principles governing heat transport, as well as the thermal properties of sediments and water, are well understood and can be reliably characterized (Anderson 2005). In the past, measuring temperature gradients required expensive sensors, as low-resolution sensors often failed to reliably detect small temperature differences (below 1°C), which is critical when quantifying water fluxes using heat transport modeling (Shanafield et al. 2011). However, recent advancements have made cost-effective high-resolution sensors more accessible, significantly expanding the use of heat as a tracer in terrestrial and aquatic research (Gilfedder et al. 2021; Sohn et al. 2024).

Quantification of SGD by using heat as a tracer relies on model-based inversion techniques (Anderson 2005). These approaches typically use either analytical or nu-

merical solutions to the heat transport equation to derive water exchange fluxes across the sediment–water interface. A widely used analytical method is the MATLAB-based software package VFLUX2 (Gordon et al. 2012; Irvine et al. 2015), which estimates fluxes by extracting amplitude and phase information from depth-specific temperature time series. Numerical models such as FLUX-BOT (Munz and Schmidt 2017) and 1DTempPro (Koch et al. 2016; Voytek et al. 2014) solve the dynamic heat transport equation using finite differences, estimating exchange fluxes through an optimization process based on measured temperature data.

However, various applications in the past have shown that these inversion methods often struggle to predict exchange fluxes accurately when the flux is rapidly changing in response to dynamic boundary conditions. Especially where a high temporal resolution (daily, sub daily) flux data is required, established inversion methods tend to fail, or at least smooth the data over multiple days. LeRoux et al. (2021) evaluated the performance of VFLUX2 and 1DTempPro in estimating SGD exchange rates in highly dynamic, tidally influenced systems. Using temperature timeseries alone, both models failed to capture sub-daily fluctuations in exchange rates driven by tidal pumping. Accurate representation of tidal cycles in 1DTempPro was only achieved when vertical head variations were incorporated into the inversion process (the authors here used a synthetic time series data from a coupled hydrological-heat transport model). Nevertheless, measuring vertical hydraulic gradients under field conditions—particularly in coastal systems—remains extremely challenging. Similar limitations were reported for FLUX-BOT, which also struggled to estimate flux variations at a sub-daily time scale (Chen et al. 2022).

McAliley et al. (2022) applied VFLUX2 to predict exchange rates for a synthetic scenario with abrupt, step-wise variations in flux rates. They found that the dynamic harmonic regression algorithm used in VFLUX2 required approximately 2 d to fully adapt to the step-wise changes. Additionally, the model's flux estimates were signifi-

cantly less accurate during periods of strong upwelling. To overcome these limitations, McAliley et al. (2022) developed a novel Kalman filter-based approach. This method combines the calibration capabilities of rigorous process-based models (e.g., 1DTemp-Pro) with digital signal processing techniques (e.g., VFLUX2), resulting in a hybrid model capable of accurately capturing sharp temporal transitions in groundwater fluxes. However, to the best of our knowledge, it remains untested whether this hybrid model can accurately reproduce high-frequency, sub-daily fluctuations in groundwater–surface water exchange, such as those driven by tidal pumping in coastal settings.

Physics-Informed Neural Networks (PINNs) are an emerging class of deep neural networks that bridge the gap between process-based modeling and machine learning (Karniadakis et al. 2021; Raissi et al. 2019). By combining the predictive power of neural networks with the interpretive clarity and physical accuracy of process-based models, PINNs offer a powerful framework for modeling complex dynamical systems. The core concept of PINNs is to embed known physical equations or constraints—represented as ordinary or partial differential equations (ODEs/PDEs)—directly into the neural network architecture. This enables the model to learn from data while simultaneously adhering to underlying physical laws. Physics-Informed Neural Networks have demonstrated their effectiveness in solving a wide range of linear and non-linear mathematical problems, including the Reynolds-averaged Navier–Stokes Equation (Eivazi et al. 2022) and the 1D Burgers Equation (Raissi et al. 2019). Recently, PINNs showed promising advances in solving both forward and inverse problems in hydrology. They have been successfully applied to inverse parameterization problems, such as multi-component diffusion–reaction systems and subsurface flow modeling (Sun et al. 2023). He and Tartakovsky (2021) employed a multiphysics-informed deep neural network to predict state variables and parameters in steady-state advection–dispersion problems. Ji et al. (2024) utilized a PINN to inversely estimate hydraulic conductivity distributions based on hydraulic head data.

In this study, we aim to evaluate the potential of PINNs for inversely solving the 1D heat transport equation to estimate SGD related flux rates. We aim to test if a PINN can overcome the current limitations of established methods such as VFLUX2, FLUX-BOT, and 1DTempPro. We use a PINN architecture that utilizes two separate deep neural networks: One for predicting spatio-temporal temperature variations and the other for estimating dynamic exchange fluxes. The training process is controlled by multiple loss functions that ensure the PINN's ability to (1) accurately reproduce observed data and (2) solve the dynamic 1D heat transport equation. We assess the performance of the PINN using both synthetic and real-world scenarios. The primary objective of this study is to determine whether the PINN can address current limitations of conventional methods by accurately capturing (1) sharp temporal transitions in water exchange fluxes and (2) high-frequency oscillations (daily to sub-daily) in advective flow patterns at the sediment–water interface and apply this to highly dynamic hydrological environments such as the coastal zone.

4.2 Materials and Procedures

4.2.1 The heat transport equation

The propagation of heat through space and time within water-saturated porous media, under the assumption of 1D unidirectional flow, can be described by the heat transport equation, which accounts for both convective and conductive heat transfer (Anderson 2005):

$$\frac{k_e}{C_s}\frac{\partial^2 T}{\partial z^2} - \frac{C_w}{C_s}\frac{\partial (Tq)}{\partial z} = \frac{\partial T}{\partial t} \tag{1}$$

With T [°C] being the temperature as a function of depth z [m], and time, t [s]. The effective thermal conductivity of the saturated sediments is denoted by k_e [J s^{-1} m^{-1} $°C^{-1}$]. The volumetric heat capacity of the fluid–solid system is given by C_s [J m^{-3} $°C^{-1}$], while the volumetric heat capacity of water is represented by C_w [J m^{-3} $°C^{-1}$].

The time- and depth-dependent Darcy flow velocity in Eq. 1 is denoted by q [m s^{-1}], with negative values indicating upward flow.

4.2.2 Physics informed neural network

The key idea behind PINNs is to embed known physical equations or constraints in the form of ODEs/PDEs directly into their architecture, allowing the model to learn from data while adhering to the underlying physical laws. Where numerical methods (such as implicit/explicit Finite Elements or Finite Differences) represent discrete integrators that project solutions at time $t + \Delta t$ based on a set of initial values at time t, PINNs are learning the multidimensional solution space described by the ODE/PDE and constrained by the imposed boundary and initial conditions. The PINN framework was developed in Python using the DeepXDE library (Lu et al. 2021), which is built on TensorFlow. We implemented a Piecewise-Feedforward Neural Network (PFNN) architecture consisting of two independent sub-networks that share a common input layer (Fig. 4.1). Each sub-network contains four hidden layers, with 40 nodes per layer. The spatio-temporal coordinates (z,t) of the model domain are fed into each sub-network through the input layer. The first sub-network (shown in red in Fig. 4.1) has a single output node that predicts the temperature values $T(z,t)$ for the given input coordinates (z,t). The second sub-network (shown in green in Fig. 4.1) also consists of a single output node, which provides the Darcy flux $q(z,t)$ for each time and spatial coordinate.

The training of the PFNN sub-networks is governed by the sum of three distinct loss functions: L_{PDE}, L_{OBS} and L_{GRAD} where λ represents the weighting factors for each loss function.

$$L_{TOTAL} = \lambda_{PDE} L_{PDE} + \lambda_{OBS} L_{OBS} + \lambda_{GRAD} L_{GRAD} \tag{2}$$

The first loss function L_{PDE} evaluates how well the predicted temperature field $T(z,t)$ satisfies the heat transport equation (Eq. 1). L_{PDE} (shown in Eq. 3a) can be derived

from Eq. 1 by applying the product rule to the advective term. The Jacobian and Hessian matrices, which represent the first- and second-order derivatives in the loss function, are internally estimated. This loss function is computed as the mean sum of the squared residuals of the PDE evaluated at the observation points N_r. The second loss function (L_{OBS}) quantifies how well the predicted temperature field matches observed data, incorporating boundary, initial conditions and observations. DeepXDE can also handle flux (Neumann-type) boundary conditions, which then are incorporated into a separate loss term rather than being combined with temperature observations (Lu et al. 2021). However, flux boundary conditions are typically not directly observable under field conditions, making this setup largely irrelevant when working with field equipment (e.g., Case Study 3). The final loss function, L_{GRAD}, ensures that the predicted Darcy fluxes $q(t)$ depend only on time. Without this term, the PINN estimates $q(z,t)$ as a function of both space and time, which is a valid alternative in this framework. However, in most applications, the inversion of the heat transport equation assumes that the Darcy flux near the measurement interface remains uniform and uni-directional across the depth profile where temperature measurements are collected.

$$L_{pdf} = \frac{1}{N_r}\sum_{i=1}^{N_r}\left[\frac{\partial T}{\partial t} + \frac{C_w}{C_s}\left(q\frac{\partial T}{\partial z} + T\frac{\partial q}{\partial z}\right) - \frac{k_e}{C_s}\frac{\partial^2 T}{\partial z^2}\right]^2 \tag{3a}$$

$$L_{obs} = \frac{1}{N_r}\sum_{i=1}^{N_r}\left[T(z,t) - T(z_{obs}, t_{obs})\right]^2 \tag{3b}$$

$$L_{grad} = \frac{1}{N_r}\sum_{i=1}^{N_r}\left[\frac{\partial q}{\partial z}\right]^2 \tag{3c}$$

Both sub-networks of the PFNN utilize a *sine* activation function, which was found to be highly effective in minimizing the loss function for periodical temperature datasets. Both networks are initialized using *Glorot Uniform* initialization. For training, a two-step optimization procedure was employed: In the first step, *ADAM* optimization is

performed for a predefined number of iterations or until the condition $L_{OBS} < \epsilon$ is met, where ϵ is a user-defined threshold value. In the second step, *L-BFGS-B* optimization is used to further reduce the total loss. The sequential use of *ADAM* followed by *L-BFGS-B* is a common strategy in PINN frameworks, as it is generally associated with improved convergence and learning performance (*see* Lu et al. 2021). Optimal weighting factors for the individual loss functions (λ_{PDE}, λ_{GRAD}, λ_{OBS}) and learning rate for all test cases were identified using hyperparameter optimization. Hyperparameter optimization was carried out using a 2-d subset of the temperature data from Case Study 2. For hyperparameter optimization, the PINN was trained for 500,000 iterations, first with the *ADAM* optimizer and subsequently with the *L-BFGS-B* algorithm.

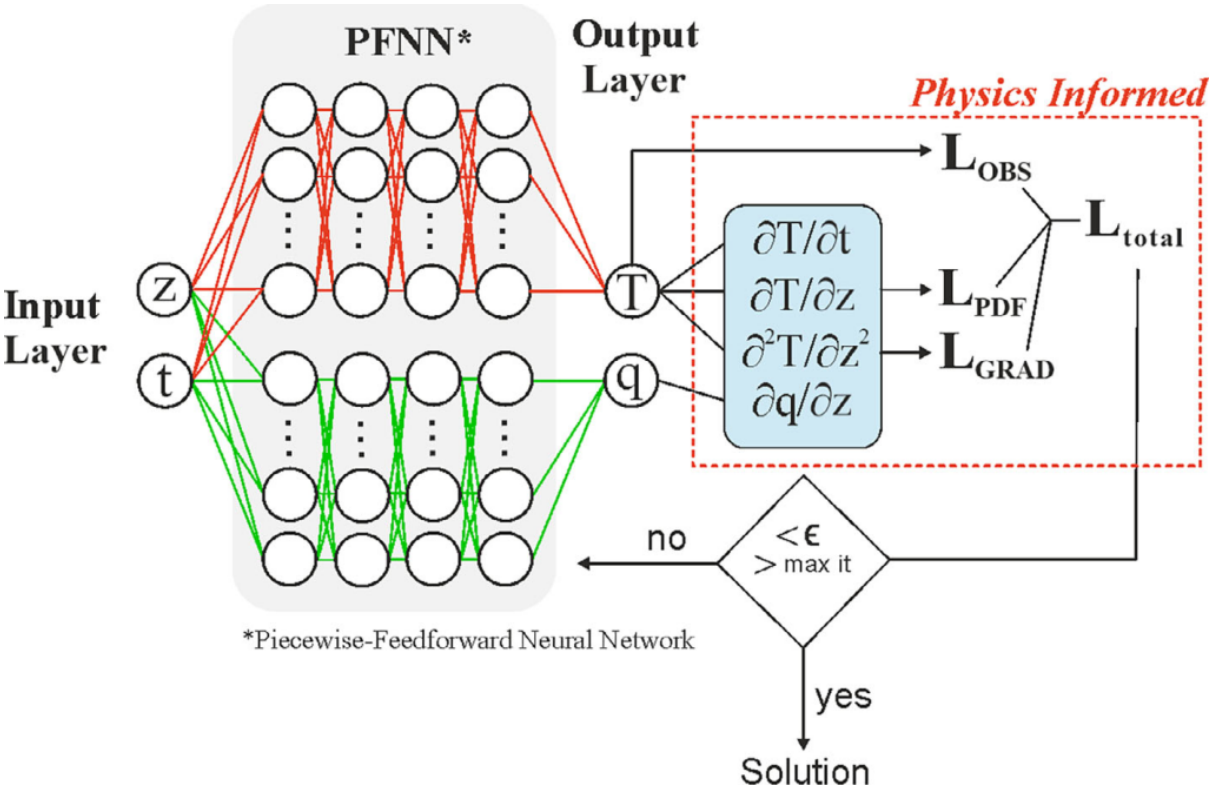


Figure 4.1. PINN architecture using Piecewise-Feedforward Neural Networks with two separate sub-nets to predict the temperature field T(z,t) and the Darcy fluxes q(t).

4.3 Assessment

The PINN framework was applied as part of three case studies: (1) a synthetic test case published by McAliley et al. (2022) where Darcy fluxes are pre-defined by a step

function, defined as an instantaneous change of Darcy fluxes, to test the PINN's ability to capture abrupt shifts in hydrological forcings; (2) a synthetic test case featuring high-frequency, sub-daily variations in Darcy fluxes published by LeRoux et al. (2021) which are representative of tidally influenced systems. These assess the PINN's capability to resolve periodically changing groundwater fluxes with dynamic boundary conditions; and (3) a real-world scenario with temperature observations from a tidal creek system with unknown Darcy fluxes, demonstrating the applicability of the PINN to work with field data under realistic coastal conditions. For all case studies, Darcy fluxes estimated by the PINN were compared to those obtained using the Extended Rauch–Tung–Striebel Smoother (ERTSS; McAliley et al. 2022), the Extended Kalman Filter (EKF; McAliley et al. 2022), as well as the Hatch/Kerry and McCallum/Luce method, both implemented in the VFLUX2 package (Gordon et al. 2012; Irvine et al. 2015). For the second case study, Darcy fluxes were additionally compared with results from 1DTempPro (fluxes were provided in the supplementary information of LeRoux et al. 2021). Fluxes were compared using the Root Mean Squared Error ($RMSE$) and Mean Absolute Error (MAE). For all test cases, the PINN was trained on a NVIDIA A100 Tensor-Core GPU using Google Colab's cloud computing platform.

4.3.1 Hyperparameter optimization

The results of the hyperparameter optimization are summarized in Table 4.1. The highest learning efficiency with the lowest total loss ($L_{TOTAL} = 1.22 \times 10^{-3}$) was achieved using a learning rate of 10^{-5} with weighting factors $\lambda_{PDE} = 1$, $\lambda_{GRAD} = 1$, and $\lambda_{OBS} = 100$. The optimal training rate and loss weightings were subsequently applied across all test cases.

Table 4.1. Results of the hyperparameter optimization. Shown are the final total loss values (L_{TOTAL}) after 500,000 iterations for the different combinations of the learning rate (rows) and the weighting factors λ_{PDE}, λ_{GRAD} and λ_{OBS}.

	$[\lambda_{PDE}, \lambda_{GRAD}, \lambda_{OBS}]$			
Learning rate	**[1, 1, 1]**	**[1, 1, 100]**	**[1, 100, 1]**	**[100, 1, 1]**
10^{-6}	5.21×10^{-3}	3.74×10^{-3}	1.95	1.30
10^{-5}	5.13×10^{-3}	1.22×10^{-3}	1.93	5.87×10^{-1}
10^{-4}	1.31×10^{-3}	1.89×10^{-3}	1.23×10^{-3}	1.84×10^{-2}
10^{-3}	2.08	1.19×10^{-1}	2.06	2.2

4.3.2 Case Study 1: Step-function

The synthetic scenario is based on a test case published in McAliley et al. (2022) to evaluate the PINN's ability to capture abrupt changes in Darcy fluxes derived from temperature data at the sediment–water interface. Heat propagation was simulated using a numerical model adapted from McAliley et al. (2022) for a 10-d period. Darcy fluxes were represented using a piecewise-defined function with instantaneous jumps (Eq. 4), designed to challenge the PINN's capability to handle sudden transitions (Fig. 4.3):

$$q(t) \begin{cases} q = 0 \ m/d & t \in [0 \ , \ 2.5[\ days \\ q = 1 \ m/d & t \in [2.5 \ , \ 5[\ days \\ q = 0 \ m/d & t \in [5 \ , \ 7.5[\ days \\ q = -1 \ m/d & t \in [7.5, 10] \ days \end{cases} \quad (4)$$

Heat transport was simulated under the assumption that the sediment–water interface experiences sinusoidal diurnal and weekly temperature fluctuations, with amplitudes of 5°C and 3°C, respectively, combined with an upward linear trend of 0.3°C per day, as described in McAliley et al. (2022). The bottom boundary was set at a depth of 5 m, assuming a constant temperature of 10°C to represent regional groundwater conditions. Thermal properties used in the simulation are listed in Table 4.2. From the simulated temperature data, time series were extracted at different depths $z = 0$, 0.21, 0.42, 0.62, 0.82, 1.01 and 1.22 m which are typical for temperature sensing lances with a temporal resolution of $\Delta t = 15$ min. The PINN used the temperature field

to inversely estimate the Darcy fluxes. Time-dependent Dirichlet boundary conditions were applied at $z = 0$ and $z = 1.22$ m, while the initial condition was derived from the simulated temperature field T (z,$t = 0$). The loss terms were evaluated at 403,200 collocation points, which coincide with the observed values, including boundary and initial conditions.

Table 4.2. Thermal properties, training parameters and data for Case Study 1.

	Case: Step-function	**Unit**
Thermal properties		
k_e	2.0	J s^{-1} m^{-1} °C^{-1}
C_w	4.182×10^6	J m^{-3} °C^{-1}
C_s	2×10^6	J m^{-3} °C^{-1}
PINN training		
ADAM iterations	2×10^6	—
L-BFGS-B iteration	15	—
Learning rate	0.0001	—
λ_{PDE},λ_{GRAD},λ_{OBS}	1, 1, 100	—
ϵ for L_{OBS}	10^{-5}	°C^2
Collocation points	403,200	—
Training data		
Length	10	d
Resolution	15	min
Depth	0, 0.21, 0.42, 0.62, 0.82, 1.01, 1.22	m
BC	T(z = 0 m,t); T(z = 1.22 m,t)	°C
IC	T(z,t = 0)	°C

Training progress for this case study is illustrated in Fig. 4.2, showing the progress of the total loss function and its individual components. After 2×10^6 iterations, L_{OBS} dropped below the predefined threshold value $\epsilon = 10^{-5}$. The PINN achieved a final total loss of $L_{TOTAL} = 4.20 \times 10^{-3}$, with contributions of $L_{PDE} = 3.43 \times 10^{-3}$, $L_{GRAD} = 7.69 \times 10^{-4}$ and $L_{OBS} = 1.00 \times 10^{-6}$, the latter also representing the MSE between the predicted and observed temperatures. Notably, L_{OBS} initially dominated L_{TOTAL} during the first 10,000 iterations. As training progressed, L_{PDE} became more dominant, indicating the model's increasing adherence to the physics of heat transport when fitting

the observed temperature timeseries. The final drop in L_{OBS} was achieved through L-BFGS-B optimization, which fine-tuned the solution after the ADAM optimization phase.

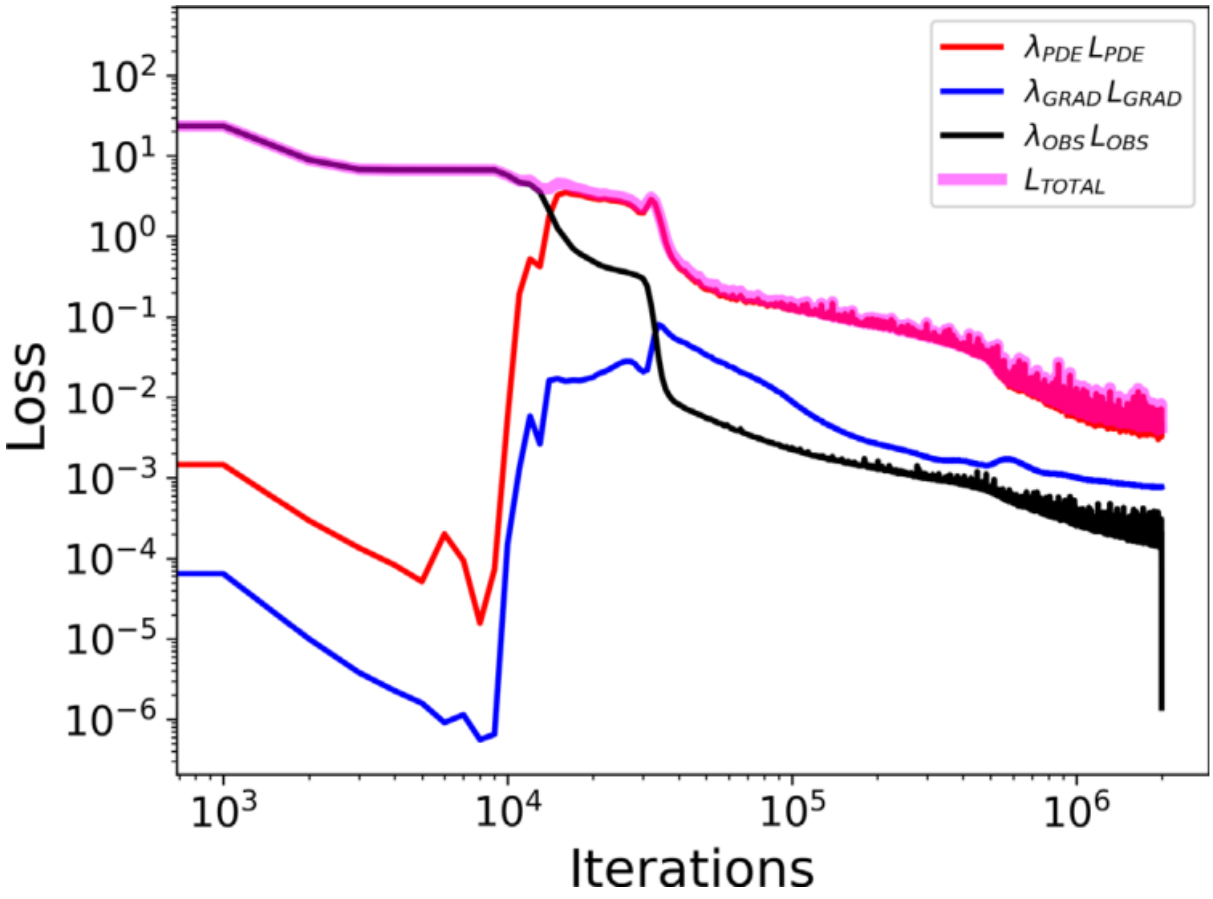


Figure 4.2. Training progress for Case Study 1 represented by the loss function and its contributions from λ_{PDE}, λ_{GRAD}, and λ_{OBS}.

Figure 4.3A shows the predicted temperature time series at different depths, along with the corresponding real and modeled variations in Darcy flux over time. Depth-specific temperature profiles exhibit daily fluctuations (day–night cycle), with amplitudes decreasing with depth under infiltrating (positive flux) and neutral (zero flux) conditions. Under exfiltrating conditions (negative fluxes), only the surface temperature ($z = 0$ m) reflects a daily cycle, while deeper temperatures are dominated by groundwater. When compared to the reference fluxes, the PINN effectively captures the instantaneous changes in q at $t = 2.5$, 5, and 7.5 d, while also accurately representing the steady flux periods between the changes. The RMSE for the flux is 0.08

m/d (Table 4.3), demonstrating a strong agreement with the reference flux. Comparable performance was obtained with the EKF and ERTSS methods (Fig. 4.3; Table 4.3). However, VFLUX2 (Hatch/Kerry and McCallum/Luce) generally had problems estimating dynamic Darcy flux over the full timespan, frequently returning NaN values. In particular, the model struggled with sharp and instantaneous transitions in Darcy fluxes, leading to substantial problems when applying the model. Only for the shallowest depth combination was the Hatch/Kerry method able to estimate fluxes over the entire timespan (Fig. 4.3B). However, those fluxes deviated substantially from the true values (Table 4.3).

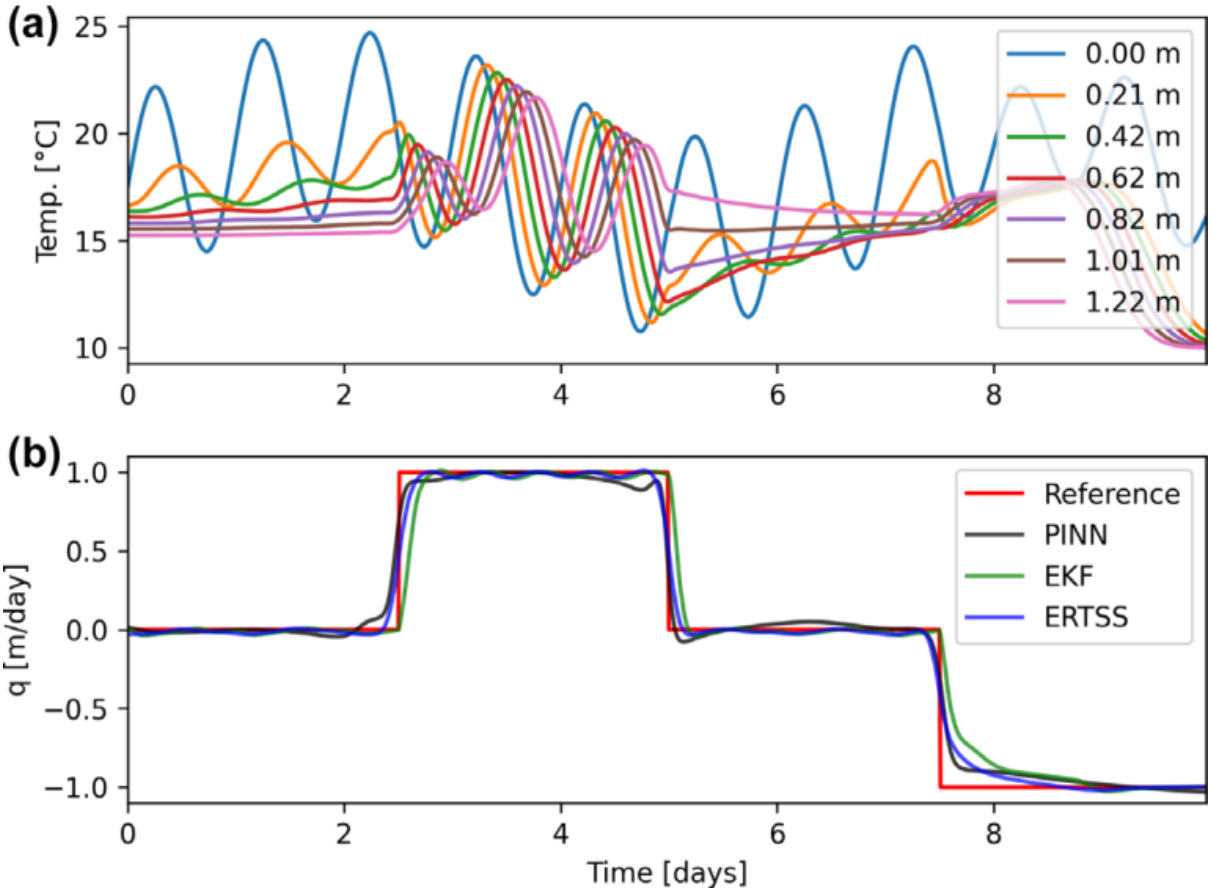


Figure 4.3. Observed temperature timeseries at the observation depths and predicted variations of the Darcy flux in time in comparison to the known reference flux. Positive fluxes: infiltration of surface water into the subsurface; Negative fluxes: groundwater discharge.

Table 4.3. Root Mean Squared Error (RMSE) and Mean Absolute Error (MAE) between estimated and observed Darcy flux. PINN = Physics-Informed Neural Network; EKF = Extended Kalman Filter; ERTSS = Extended Rauch–Tung–Striebel Smoother. Hatch/Kerry and McCallum/Luce denote two methods implemented in VFLUX2.

	RMSE [m/d]	**MAE [m/d]**
PINN	0.08	0.05
EKF	0.15	0.07
ERTSS	0.09	0.04
Hatch/Keery	0.69	0.5
McCallum/Luce	N/A	N/A

4.3.3 Case Study 2: Tidal pumping

The tidal pumping scenario is based on a synthetic dataset published in LeRoux et al. (2021). For generating the synthetic data, LeRoux et al. (2021) used the process-based heat transport and flow model SUTRA (Voss and Provost 2002). SUTRA is a numerical finite-element groundwater model developed by the United States Geological Survey (USGS). It simulates water flow, energy transport, and chemical transport, including variable-density flow. Due to these capabilities, SUTRA is commonly used for modeling coastal groundwater systems. In LeRoux et al. (2021), SUTRA was configured to simulate vertical heat propagation into marine sediments. In LeRoux et al. (2021), a constant temperature boundary condition was set at 100 m depth representing the thermal inertia of the deep subsurface, while the diurnal and semi-diurnal surface temperature ($z = 0$ m) variations mimic the influence of solar radiation and tidal mixing in shallow coastal waters. These boundary conditions provide a realistic yet controlled environment to test the PINN's capability to learn heat propagation influenced by tidal settings. For the PINN, the 12.25-h tidal period (M2 tidal constituent) scenario was chosen, representing macro-tidal conditions with a 2.5 m amplitude (LeRoux et al. 2021). For training the PINN, we used the dynamic temperature profiles at depths of $z = 0$, 0.05, 0.10, 0.15, 0.20, 0.30, 0.40, and 0.50 m, obtained from the supplementary material of LeRoux et al. (2021). For these macro-tidal settings, exchange fluxes varied dynamically between 0.35 and -0.52 m/d, following a sinusoidal pattern (Fig.

4.5). This setup allowed the PINN to learn periodic Darcy flux variations, capturing the tidal pumping dynamics with a high temporal resolution (14-min intervals). For the PINN, time-dependent Dirichlet boundary conditions were used at $z = 0$ and $z = 0.5$ m, while the initial condition was derived from the simulated SUTRA temperature field $T(z,t = 0)$. Thermal properties and PINN hyperparameters used for this case are listed in Table 4.4. The loss terms were evaluated at 368,800 collocation points, which coincide with the observed values, including boundary and initial conditions.

Table 4.4. Thermal properties, training parameters and data for Case Study 2.

	Case: Tidal pumping	**Unit**
Thermal properties		
k_e	2.63	J s^{-1} m^{-1} °C^{-1}
C_w	4.182×10^6	J m^{-3} °C^{-1}
C_s	2.814×10^6	J m^{-3} °C^{-1}
PINN training		
ADAM iterations	3.5×10^6	—
L-BFGS-B iterations	104	—
Learning rate	0.0001	—
λ_{PDE},λ_{GRAD},λ_{OBS}	1, 1, 100	—
ϵ for L_{OBS}	10^{-5}	°C^2
Collocation points	368,800	—
Training data		
Length	7.47	d
Resolution	14	min
Depths	0, 0.05, 0.10, 0.15, 0.20, 0.30, 0.40, 0.50	m
BC	T(z = 0 m,t); T(z = 0.5 m,t)	°C
IC	T(z,t = 0)	°C

The PINN was trained using the hybrid optimization approach, and the threshold criteria for L_{OBS} was reached after 3.5×10^6 iterations. The total loss function L_{TOTAL} initially was dominated by L_{OBS} due to the high initial discrepancies between the predicted and reference temperatures (Fig. 4.4). However, as training progressed, L_{PDE} became more dominant in the total loss function. Final total loss of $L_{TOTAL} = 1.93 \times 10^{-3}$ was achieved with the contributions of $L_{PDE} = 1.39 \times 10^{-3}$, $L_{GRAD} = 5.36 \times 10^{-4}$

and $L_{OBS} = 1.00 \times 10^{-6}$ (MSE for predicted and observed temperatures). The temperature time series (Fig. 4.5A) exhibits a clear periodic signal corresponding to the daily (day–night) cycle, with amplitudes decreasing with depth and further modulated by the M2 tidal cycle. The PINN demonstrated good performance in capturing the 12.25-h M2 tidal period with an MSE of 0.06 m/d (Table 4.5; Fig. 4.5B) compared to the reference Darcy flux timeseries. Although minor deviations in phase shift and amplitude were observed for certain tidal cycles, the overall performance was very good. Compared to the other tested methods, the PINN more closely represents reality than either the spectral approaches (Hatch/Keery, McCallum/Luce) or the process-based methods (1DTempPro, EKF, and ERTSS) (Table 4.5; Fig. 4.5B,C). The spectral methods and 1DTempPro failed to reproduce the periodic variations in Darcy flux associated with tidally driven flow reversals. While the EKF and ERTSS methods capture these periodic patterns, their predicted amplitudes are damped relative to the reference flux, and their phases are shifted.

Table 4.5. Root Mean Squared Error (RMSE) and Mean Absolute Error (MAE) between estimated and observed Darcy flux. PINN = Physics-Informed Neural Network; EKF = Extended Kalman Filter; ERTSS = Extended Rauch–Tung–Striebel Smoother. Hatch/Kerry and McCallum/Luce denote two methods implemented in VFLUX2.

	RMSE [m/d]	**MAE [m/d]**
PINN	0.06	0.05
Hatch/Keery*	0.18	0.15
McCallum/Luce*	0.16	0.14
1DTempPro*	0.16	0.14
EKF	0.19	0.17
ERTSS	0.11	0.09

*Based on data from LeRoux et al. (2021).

4.3.4 Case Study 3: Tidal creek system

The third case study utilizes an unpublished temperature time series collected from the tidal creek system “De Slufter” on Texel, a barrier island off the coast of the Netherlands. De Slufter was historically artificially closed to the sea by a dam. However,

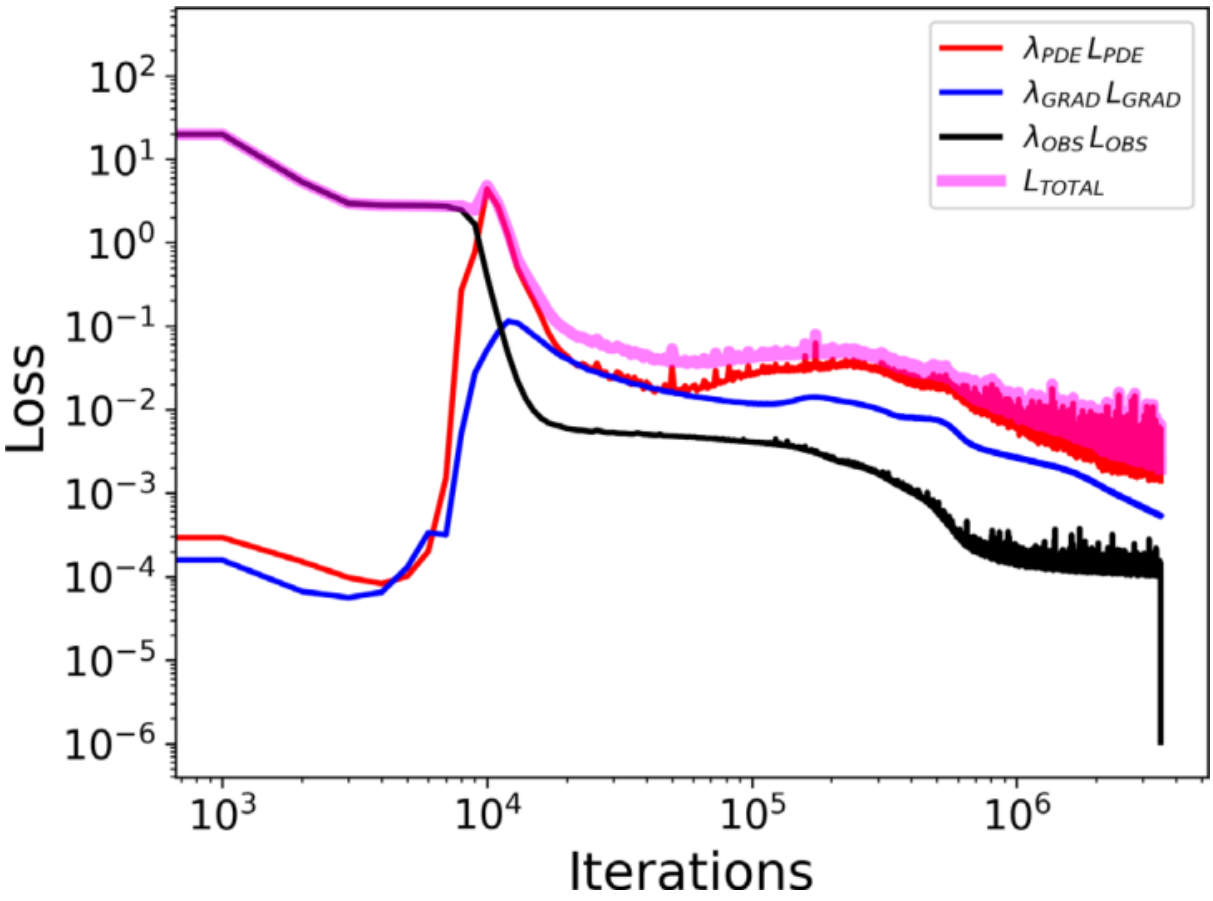


Figure 4.4. Training progress for Case Study 2 represented by the loss function and its contributions from λ_{PDE}, λ_{GRAD}, and λ_{OBS}.

it has been open to the sea and strongly influenced by tides since this dam broke in 1858. Since then the tidal creek system has belonged to the Dutch national park "Duinen van Texel". The area surrounding the national park is used for crop farming and pasture. Temperature measurements were conducted in a small side branch of the creek over a 15-d period in June 2024 using a temperature lance equipped with thermistors positioned at multiple depths (z = 0.00, 0.04, 0.08, 0.12, 0.16, 0.20, and 0.24 m). The precision of the measurements was estimated at 0.003°C and measurements were made with a temporal resolution of 15 min. Time-dependent Dirichlet boundary conditions were used at $z = 0$ and $z = 0.24$ m, while the initial condition was derived from the observed temperature field $T(z,t = 0)$. Thermal properties of the water-saturated sediments were determined in the laboratory using soil samples extracted from the study site (Table 4.6). To evaluate how parameter uncertainty influences the PINN predictions of Darcy

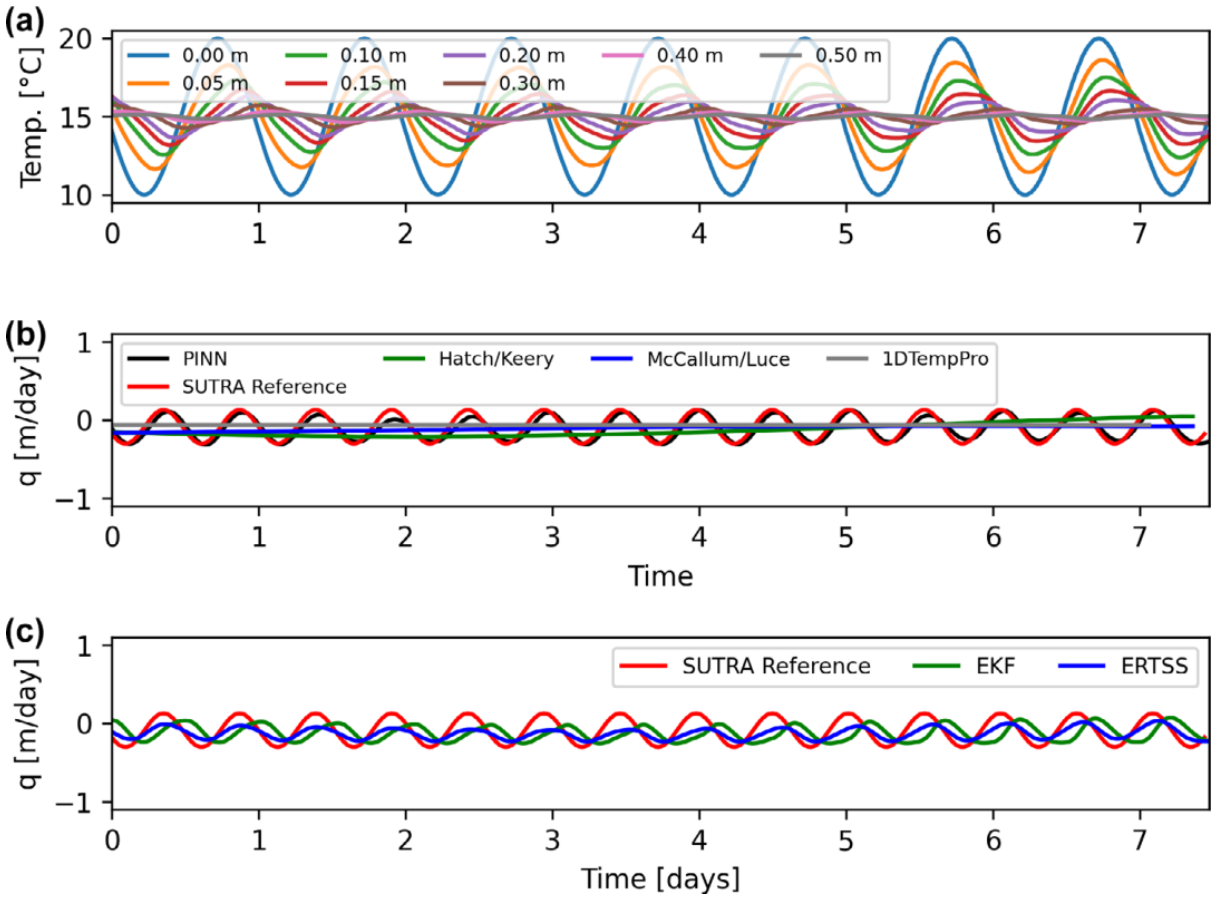


Figure 4.5. Observed temperature timeseries at the observation depths and predicted variations of the Darcy flux in time in comparison to the known reference flux. Positive fluxes: infiltration of surface water into the subsurface; Negative fluxes: groundwater discharge.

fluxes, the thermal conductivity of the saturated sediments (k_e) was lowered/increased from the measured value from 1.85 to 1.5 and 2.5 J s^{-1} m^{-1} $°C^{-1}$ as part of separate PINN runs. This range of thermal conductivities is consistent with reported values for water-saturated sand (Midttømme et al. 1998). The loss terms were evaluated at 604,800 collocation points, which coincide with the observed values, including boundary and initial conditions.

Table 4.6. Thermal properties, training parameters and data for Case Study 3.

	Case: Step-function	**Unit**
Thermal properties		
k_e	1.85 (1.5 and 2.5)	J s^{-1} m^{-1} $°C^{-1}$
C_w	4.11×10^6	J m^{-3} $°C^{-1}$
C_s	2.77×10^6	J m^{-3} $°C^{-1}$
PINN training		

Continued on next page

	Case: Step-function	**Unit**
ADAM iterations	3.5×10^6	—
L-BFGS-B iterations	12	—
Learning rate	0.0001	—
λ_{PDE},λ_{GRAD},λ_{OBS}	1, 1, 100	—
ϵ for L_{OBS}	10^{-5}	$°C^2$
Collocation points	604,800	—
Training data		
Length	15	d
Resolution	15	min
Depths	0.00, 0.04, 0.08, 0.12, 0.16, 0.20, 0.24	m
BC	T(z = 0 m,t); T(z = 0.24 m,t)	°C
IC	T(z,t = 0)	°C

The PINN was trained using the hybrid optimization approach, and the threshold criteria for L_{OBS} was reached after 3.5×10^6 iterations. Similar to the other cases, the total loss (L_{TOTAL}) was initially dominated by the observation loss (L_{OBS}) due to discrepancies between the predicted and reference temperatures (Fig. 4.6). Final loss terms are $L_{TOTAL} = 1.82 \times 10^{-2}$, $L_{PDE} = 7.15 \times 10^{-3}$, $L_{GRAD} = 1.11 \times 10^{-2}$ and $L_{OBS} = 7.00 \times 10^{-6}$ (MSE for predicted and observed temperatures). Figure 4.7A presents the simulated temperature time series, the predicted Darcy fluxes (Fig. 4.7B), and the relative tidal water levels (Fig. 4.7C) obtained from Rijkswaterstaat (https://waterinfo.rws.nl/publiek/astronomische-getij) from the northern part of the island. The predicted Darcy fluxes were compared (Fig. 4.7B) to those estimated using the Kalman filter-based methods proposed by McAliley et al. (2022).

The PINN predicted Darcy fluxes exhibited a periodic pattern, with high infiltration into the sediments (positive fluxes) occurring during high tides, and lower infiltration rates or even flow reversal from infiltration to exfiltration during low tide. This pattern is consistent with the tidal dynamics, and previous literature on tidal pumping (LeRoux et al. 2021) as the increased pressure head during high tide (up to 1 m) enhances the hydraulic gradient, influencing both the magnitude and direction of flow at the water–

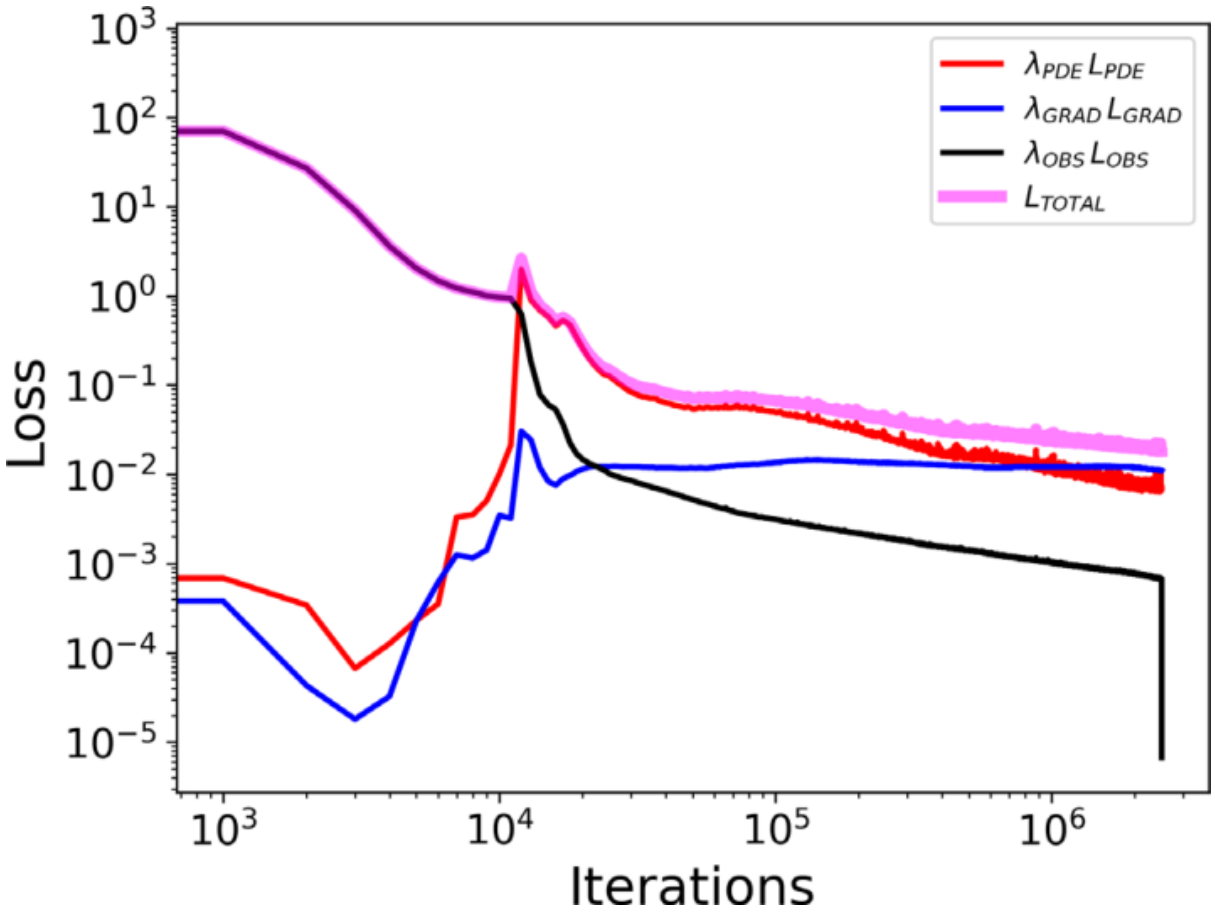


Figure 4.6. Training progress for Case Study 3 represented by the loss function and its contributions from λ_{PDE}, λ_{GRAD}, and λ_{OBS}.

sediment interface. During high tide, the hydraulic gradients reach their maximum, resulting in high infiltration rates, while during low tide, the gradients diminish or even reverse, leading to reduced infiltration or exfiltration.

A spectral analysis calculated for the modeled Darcy fluxes and the relative tidal heights indicates similar dominant frequencies (f) in both datasets. Dominant frequencies in the water level time series (Fig. 4.8) were found at approximately $f = 1$ and 2 d^{-1}, corresponding approximately to daily and sub-daily (12-h) cycles. These cycles can be attributed to the M2 (12 h 25 min) and K1 (23 h 56 min) tidal constituents. However, the time series was too short to identify spring tides (14-d cycle). Both the daily and sub-daily cycles associated with the M2 and K1 tidal constituents were also present in the predicted Darcy fluxes (Fig. 4.9). The M2 signal however was less pro-

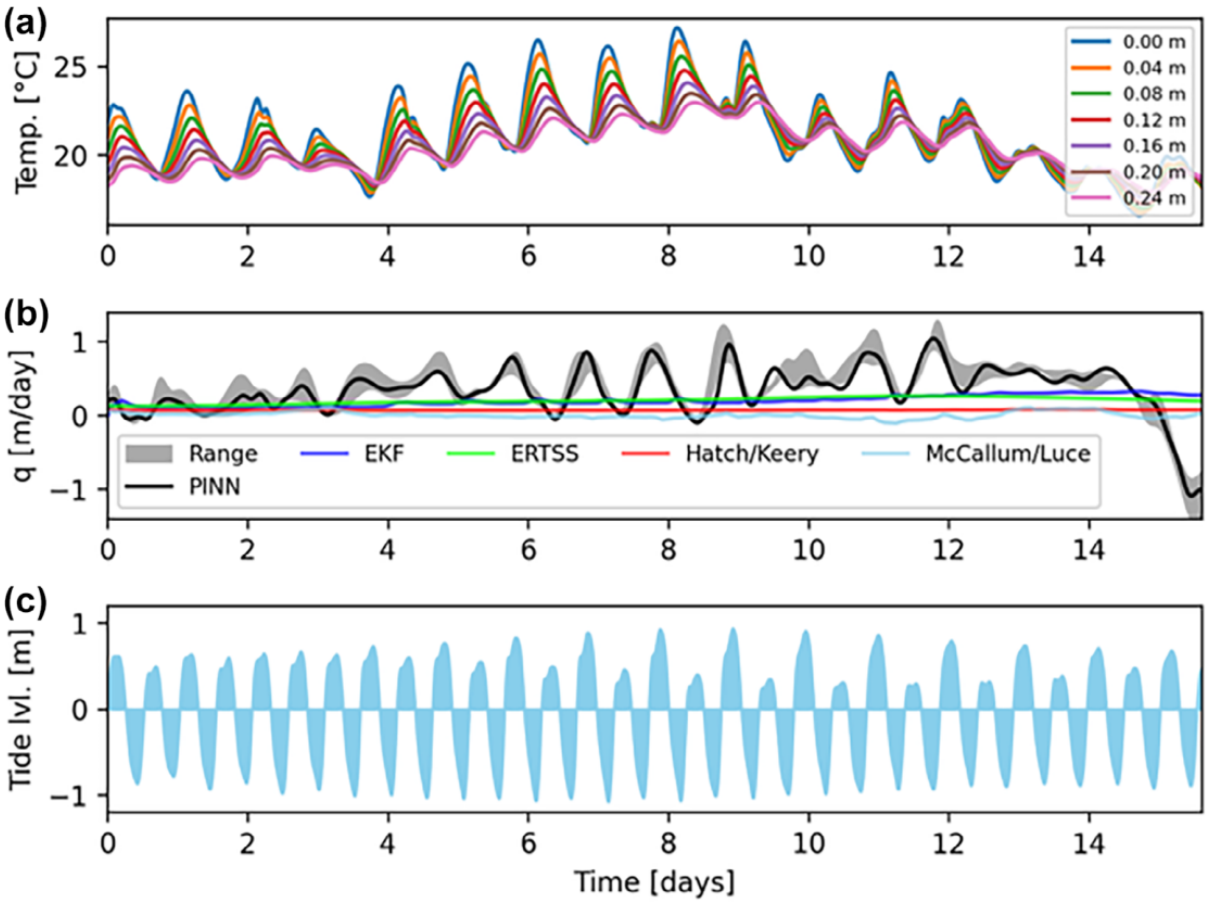


Figure 4.7. Measured temperature timeseries at the observation depths and predicted variations of the Darcy flux in time in comparison to the known reference flux. Tidal level variations are indicated in blue in the lower plot. Positive fluxes: infiltration of surface water into the subsurface; Negative fluxes: groundwater discharge. EKF: Extended Kalman Filter (McAliley et al. 2022). ERTSS: Extended Rauch–Tung–Striebel Smoother (McAliley et al. 2022).

nounced in the Darcy flux compared to the tidal water levels, as indicated by a lower relative power in the spectra compared to the K1 constituent.

When compared to the Darcy fluxes estimated using the Kalman filter methods (EKF and ERTSS) of McAliley et al. (2022), the PINN-derived fluxes clearly captured the influence of tidal forcing. Fluxes estimated with the method of McAliley et al. (2022) do not show the tidal-induced variations in Darcy fluxes. It should be noted, however, that the method by McAliley et al. (2022) utilizes different strategies to identify covariance models in the inverse simulation (i.e., the discrepancy principle and L-curve criterion), and neither approach provided a clear identification for this case. For the spectral method of McCallum/Luce, some fluctuations in Darcy flux

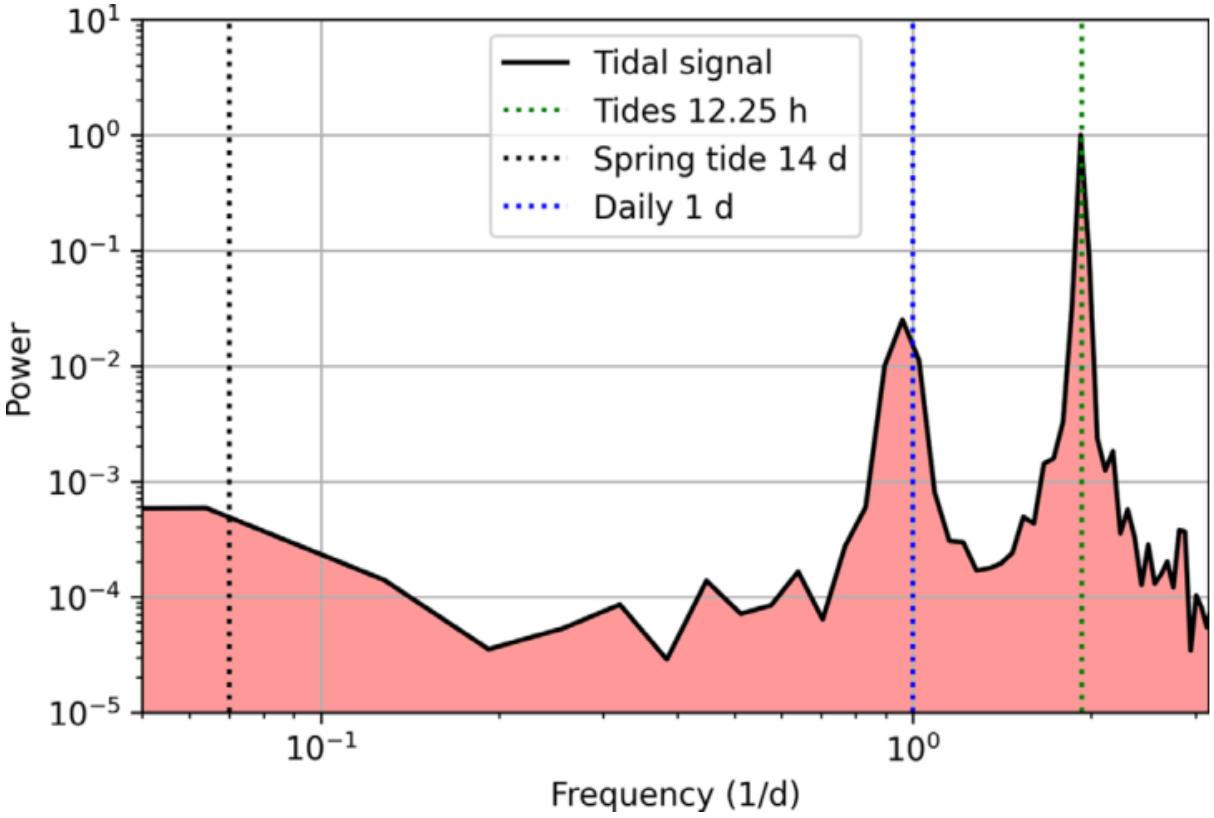


Figure 4.8. Power spectra of the tidal level variations observed for the study area and shown in Fig. 4.7.

are visible that reflect tidal influence; however, the amplitudes are much smaller than those predicted by the PINN, and the fluxes remain predominantly negative, indicating persistent groundwater discharge to the tidal creek.

In general, the PINN predictions of Darcy fluxes obtained using the measured value of the saturated thermal conductivity fall between those derived from the tested range of k_e values (1.5–2.5 J s^{-1} m^{-1} °C^{-1}), as shown in Fig. 4.7B. Increasing k_e to 2.5 J s^{-1} m^{-1} °C^{-1} results in lower Darcy fluxes, which is consistent with theory: higher heat conduction reduces the need for advective flux to explain the observed temperature signals. Conversely, decreasing k_e to 1.5 J s^{-1} m^{-1} °C^{-1} yields higher predicted Darcy fluxes, since lower conduction requires stronger advection to match the measurements. This demonstrates that the PINN responds in a physically plausible manner. However, some flux peaks appear slightly out of phase across the different simulations. Also, toward the end of the time series ($t > 15$ d), the predicted fluxes for all cases diverge

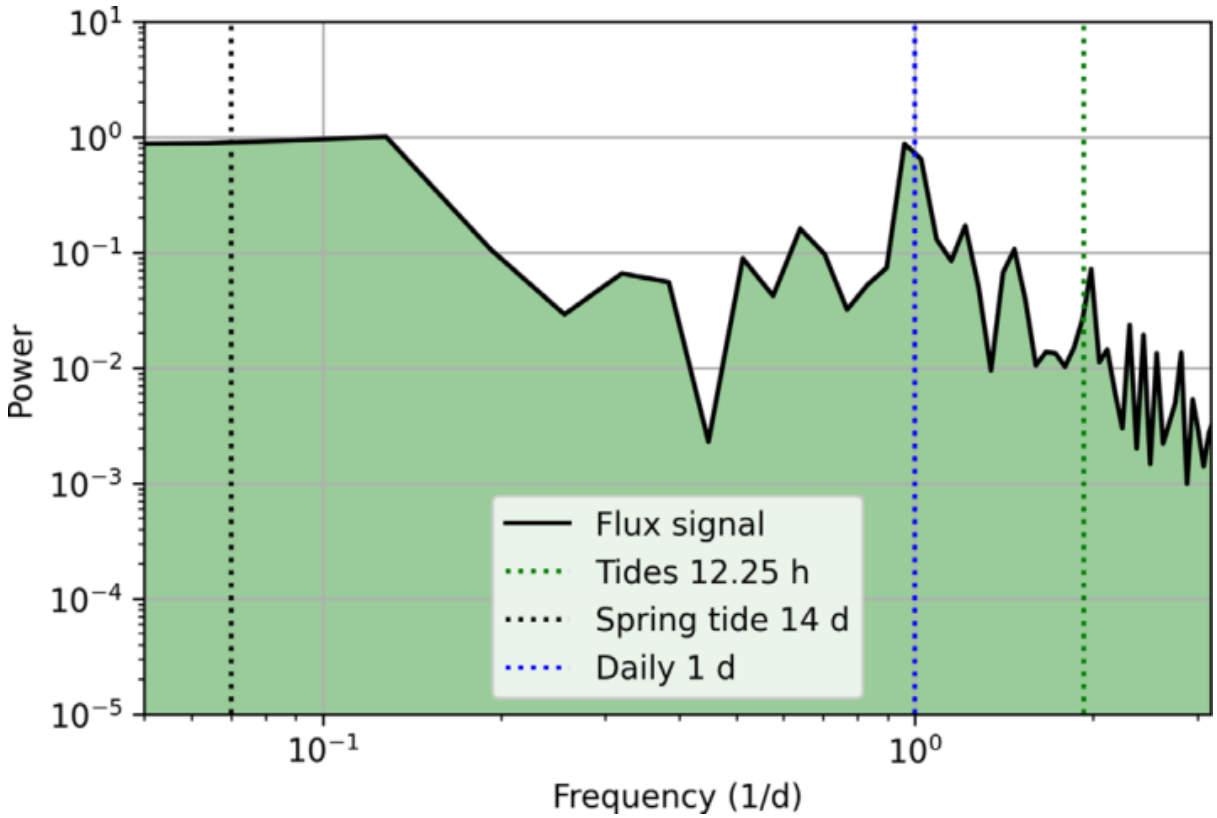


Figure 4.9. Power spectra of the Darcy fluxes predicted by the PINN for the Texel data set.

into unrealistically high negative fluxes (Fig. 4.7B). This suggests that the PINN may struggle to provide reliable flux predictions close to the end of the time series.

4.4 Discussion

The primary aim of this study was to investigate whether a PINN is able to overcome the limitations of analytical and numerical methods in the inverse estimation of Darcy fluxes using temperature data, especially at sub-daily resolution. We used three different scenarios to validate if (1) the PINN is able to accurately capture sharp transitions in Darcy fluxes (Case Study 1: Step Function) and (2) if it can be used to perform inverse estimation of Darcy fluxes under highly dynamic forcing conditions, such as those found in tidal systems (Case Study 2 + 3: Tidal Pumping and Tidal Creek).

For both synthetic cases, where Darcy fluxes were known a priori, the PINN demonstrated excellent performance in representing observed temperature variations, achieving MSE values on the order of 10^{-6} $(°C)^2$. The Darcy fluxes predicted by the PINN closely matched the reference values for both the step-function and tidal pumping scenarios often outperforming spectral and process-based methods. For all the test cases, the sub-net architecture in combination with constraining loss functions and the sine activation function proved to be highly efficient. For the step-function scenario (Case Study 1), the PINN performed comparably well to the Kalman filter-based methods (McAliley et al. 2022). In the tidal pumping scenario (Case Study 2), the PINN successfully reconstructed the M2 tidal cycle using temperature time series alone—a capability that, to our knowledge, has not been achieved by any other heat inversion method to date. Traditional approaches such as VFLUX2 and 1DTEMPRO could only accurately estimate Darcy fluxes in the absence of tidal signals (LeRoux et al. 2021) and with a time delay of approximately 2.5 d, which accounts for the time required to remove edge effects in signal processing (Hatch et al. 2006; Irvine et al. 2015). Once M2 tidal fluctuations were introduced, neither VFLUX2 nor 1DTEMPRO could reliably capture the temporal dynamics of Darcy fluxes through inverse modeling (LeRoux et al. 2021). An accurate representation could only be achieved by incorporating both temperature and hydraulic gradient data into the inversion process of 1DTempPro (LeRoux et al. 2021).

However, vertical hydraulic gradient data is typically unavailable or very difficult to collect accurately during measurements. The EKF and ERTSS methods introduced by McAliley et al. (2022) were able to estimate periodic shifts in the Darcy flux, but only with reduced amplitude and a phase delay compared to the known reference flux.

For the field case scenario (Case Study 3), where the hydraulic forcing includes more than a single tidal cycle, spectral analysis revealed the presence of M1 and K1 cycles in the inverted Darcy flux data as well as the tidal height data. The tidal creek conditions can be classified as net-losing, with high exchange rates during K1 high tides (daily cycle) and occasional flow reversals from infiltration to exfiltration during low tides. This agrees with field-based pore water sampling that shows saline water within the first 20 cm of the creek sediments. To our knowledge, no other inversion method has been able to provide such highly detailed insights into how tidal cycles control SGD using temperature. This highlights a unique advantage of combining vertical temperature measurements with a PINN architecture.

Beyond coastal and marine systems, water bodies in terrestrial environments—such as rivers, streams, or lakes—also are prone to rapid changes in water level such as during floods, or sub-daily fluctuations in hydraulic forcing similar to tidal dynamics (e.g., Seiches). Diurnal variations in snowmelt (Caine 1992; Kurylyk and Hayashi 2017), glacier melt (Condom et al. 2012), evapotranspiration (Cadol et al. 2012), or water management cycles of reservoirs (Smith et al. 2016) may generate a similar influence on surface-groundwater interactions compared to tides. Here PINNs also offer a novel method to gain further insights in groundwater–surface water interactions. Also storm events can serve as significant recharge mechanisms for both local and regional aquifers. However, quantifying these fluxes using temperature-based methods and standard models available to date has proven challenging (McCallum et al. 2012; Rau et al. 2014). The PINN could potentially capture these short-term variations and assist with predicting accurate water fluxes during those extreme events.

The PINN framework, in its current form, faces several limitations. First, scalability remains a challenge, as the proof-of-concept simulations were restricted to relatively short datasets (up to 15 d). Second, the efficiency of the learning process is still suboptimal: in our implementation, training requires about 2–3.5 million ADAM iterations to reach an acceptable loss, corresponding to roughly 1.5–3 h on a GPU server. Future improvements could significantly reduce runtimes by adopting more efficient activation functions or novel network architectures. Preprocessing the temperature time series with autoencoders may further simplify the input data, decrease the number of trainable parameters, and thus accelerate training. Finally, the method currently depends on the availability of substantial computational resources, particularly GPUs, which are not always available to every researcher. Cloud-based GPU platforms such as Google Colab can help overcome this limitation by both enabling efficient training and improving scalability for larger datasets, while also broadening access to researchers without dedicated GPU infrastructure.

4.5 Comments and Recommendations

In conclusion, this study successfully demonstrated the potential of PINNs to overcome the limitations of traditional methods in estimating Darcy fluxes, especially under high temporal resolution and dynamic forcing conditions. The PINN model proved highly effective in accurately capturing sharp transitions in Darcy fluxes, as well as reconstructing tidal dynamics using temperature data alone —something process-based as well as spectral methods have struggled with. The ability to accurately estimate exchange fluxes under varying tidal conditions, such as those observed in tidal pumping or tidal creek systems, highlights the unique capabilities of PINNs in providing detailed insights into SGD and surface-groundwater interactions.

Furthermore, the application of PINNs could extend beyond coastal and marine systems to other environments experiencing rapid water level changes, such as rivers, streams, or lakes during floods or snowmelt. The PINN's potential to capture short-

term variations in water fluxes, particularly during tidal or tidal-like dynamics, could be invaluable for future applications. The use of cloud-based GPU computing resources further supports the scalability of the PINN, allowing researchers with limited access to computational infrastructure to leverage this technology. Overall, the results from this study open exciting new avenues for improving our understanding of water flux dynamics in both coastal and terrestrial environments.

Author Contributions

S. Frei developed the model framework and wrote the manuscript. A. M. Seiverth conducted fieldwork to collect the temperature time series used in this study. M. U. Munir contributed to coding the PINN framework in Python. B. S. Gilfedder was the lead scientist for the field campaign and contributed to writing and revising the manuscript.

Acknowledgments

We want to thank J. Gleiß for her help during the field work on Texel and the anonymous reviewers for their valuable feedback, which helped improve the manuscript.

Conflicts of Interest

None declared.

Data Availability Statement

All datasets and source codes used for running the PINN framework in the study are available at https://github.com/saluisto/PINN_HEAT_WRR and Zenodo (https://doi.org/10.5281/zenodo.15230610) with open license conditions.

References

Anderson, M. P. 2005. "Heat as a Ground Water Tracer." *Groundwater* 43, no. 6: 951–968.

Beusen, A. H. W., C. P. Slomp, and A. F. Bouwman. 2013. "Global Land–Ocean Linkage: Direct Inputs of Nitrogen to Coastal Waters Via Submarine Groundwater Discharge." *Environmental Research Letters* 8, no. 3: 034035.

Burnett, W. C., P. K. Aggarwal, A. Aureli, et al. 2006. "Quantifying Submarine Groundwater Discharge in the Coastal Zone Via Multiple Methods." *Science of the Total Environment* 367, no. 2–3: 498–543.

Cadol, D., S. Kampf, and E. Wohl. 2012. "Effects of Evapotranspiration on Baseflow in a Tropical Headwater Catchment." *Journal of Hydrology* 462: 4–14.

Caine, N. 1992. "Modulation of the Diurnal Streamflow Response by the Seasonal Snowcover of an Alpine Basin." *Journal of Hydrology* 137, no. 1–4: 245–260.

Chen, K., X. Chen, X. Song, et al. 2022. "Using Ensemble Data Assimilation to Estimate Transient Hydrologic Exchange Flow Under Highly Dynamic Flow Conditions." *Water Resources Research* 58, no. 5: e2021WR030735.

Condom, T., M. Escobar, D. Purkey, et al. 2012. "Simulating the Implications of Glaciers' Retreat for Water Management: A Case Study in the Rio Santa Basin, Peru." *Water International* 37, no. 4: 442–459.

Diaz, R. J., and R. Rosenberg. 2008. "Spreading Dead Zones and Consequences for Marine Ecosystems." *Science* 321, no. 5891: 926–929.

Duarte, C. M. 1995. "Submerged Aquatic Vegetation in Relation to Different Nutrient Regimes." *Ophelia* 41, no. 1: 87–112.

Duarte, C. M., and J. Cebrián. 1996. "The Fate of Marine Autotrophic Production." *Limnology and Oceanography* 41, no. 8: 1758–1766.

Dulaiova, H., R. Camilli, P. B. Henderson, and M. A. Charette. 2010. "Coupled Radon, Methane and Nitrate Sensors for Large-Scale Assessment of Groundwater Discharge and Non-point Source Pollution to Coastal Waters." *Journal of Environmental Radioactivity* 101, no. 7: 553–563.

Eivazi, H., M. Tahani, P. Schlatter, and R. Vinuesa. 2022. "Physics-Informed Neural Networks for Solving Reynolds-Averaged Navier–Stokes Equations." *Physics of Fluids* 34, no. 7: 075117.

Gilfedder, B. S., H. Waska, F. Wismeth, and S. Frei. 2021. "Using Heat as a Tracer to Map and Quantify Water Infiltration and Exfiltration along a Complex High Energy Beach Face." *Estuarine, Coastal and Shelf Science* 250: 107140.

Glibert, P. M., J. M. Burkholder, and T. M. Kana. 2012. "Recent Insights About Relationships Between Nutrient Availability, Forms, and Stoichiometry, and the Distri-

bution, Ecophysiology, and Food Web Effects of Pelagic and Benthic Prorocentrum Species." *Harmful Algae* 14: 231–259.

Gordon, R. P., L. K. Lautz, M. A. Briggs, and J. M. McKenzie. 2012. "Automated Calculation of Vertical Pore-Water Flux From Field Temperature Time Series Using the VFLUX Method and Computer Program." *Journal of Hydrology* 420: 142–158.

Grzelak, K., J. Tamborski, L. Kotwicki, and H. Bokuniewicz. 2018. "Ecostructuring of Marine Nematode Communities by Submarine Groundwater Discharge." *Marine Environmental Research* 136: 106–119.

Hatch, C. E., A. T. Fisher, J. S. Revenaugh, J. Constantz, and C. Ruehl. 2006. "Quantifying Surface Water–Groundwater Interactions Using Time Series Analysis of Streambed Thermal Records: Method Development." *Water Resources Research* 42, no. 10: W10410.

He, Q., and A. M. Tartakovsky. 2021. "Physics-Informed Neural Network Method for Forward and Backward Advection-Dispersion Equations." *Water Resources Research* 57, no. 7: e2020WR029479.

Howarth, R. W., and R. Marino. 2006. "Nitrogen as the Limiting Nutrient for Eutrophication in Coastal Marine Ecosystems: Evolving Views Over Three Decades." *Limnology and Oceanography* 51, no. 1part2: 364–376.

Irvine, D. J., L. K. Lautz, M. A. Briggs, R. P. Gordon, and J. M. McKenzie. 2015. "Experimental Evaluation of the Applicability of Phase, Amplitude, and Combined Methods to Determine Water Flux and Thermal Diffusivity From Temperature Time Series Using VFLUX 2." *Journal of Hydrology* 531: 728–737.

Ji, Y., Y. Zha, T.-C. J. Yeh, L. Shi, and Y. Wang. 2024. "Groundwater Inverse Modeling: Physics-Informed Neural Network With Disentangled Constraints and Errors." *Journal of Hydrology* 640: 131703.

Karniadakis, G. E., I. G. Kevrekidis, L. Lu, P. Perdikaris, S. Wang, and L. Yang. 2021. "Physics-Informed Machine Learning." *Nature Reviews Physics* 3, no. 6: 422–440.

Koch, F. W., E. B. Voytek, F. D. Day-Lewis, et al. 2016. "1DTempPro V2: New Features for Inferring Groundwater/Surface-Water Exchange." *Ground Water* 54, no. 3: 434–439.

Kotwicki, L., K. Grzelak, M. Czub, et al. 2014. "Submarine Groundwater Discharge to the Baltic Coastal Zone: Impacts on the Meiofaunal Community." *Journal of Marine Systems* 129: 118–126.

Kurylyk, B. L., and M. Hayashi. 2017. "Inferring Hydraulic Properties of Alpine Aquifers From the Propagation of Diurnal Snowmelt Signals." *Water Resources Research* 53, no. 5: 4271–4285.

Landsberg, J. H. 2002. "The Effects of Harmful Algal Blooms on Aquatic Organisms." *Reviews in Fisheries Science* 10, no. 2: 113–390.

Lecher, A. L., and K. R. M. Mackey. 2018. "Synthesizing the Effects of Submarine Groundwater Discharge on Marine Biota." *Hydrology* 5, no. 4: 60.

LeRoux, N. K., B. L. Kurylyk, M. A. Briggs, D. J. Irvine, J. J. Tamborski, and V. F. Bense. 2021. "Using Heat to Trace Vertical Water Fluxes in Sediment Experiencing Concurrent Tidal Pumping and Groundwater Discharge." *Water Resources Research* 57, no. 2: e2020WR027904.

Lirman, D., B. Orlando, S. Maciá, et al. 2003. "Coral Communities of Biscayne Bay, Florida and Adjacent Offshore Areas: Diversity, Abundance, Distribution, and Environmental Correlates." *Aquatic Conservation: Marine and Freshwater Ecosystems* 13, no. 2: 121–135.

Lu, L., X. Meng, Z. Mao, and G. E. Karniadakis. 2021. "DeepXDE: A Deep Learning Library for Solving Differential Equations." *SIAM Review* 63, no. 1: 208–228.

Luijendijk, E., T. Gleeson, and N. Moosdorf. 2020. "Fresh Groundwater Discharge Insignificant for the World's Oceans But Important for Coastal Ecosystems." *Nature Communications* 11, no. 1: 1260.

McAliley, W. A., F. D. Day-Lewis, D. Rey, M. A. Briggs, A. M. Shapiro, and D. Werkema. 2022. "Application of Recursive Estimation to Heat Tracing for Groundwater/Surface-Water Exchange." *Water Resources Research* 58, no. 6: e2021WR030443.

McCallum, A. M., M. S. Andersen, G. C. Rau, and R. I. Acworth. 2012. "A 1-D Analytical Method for Estimating Surface Water–Groundwater Interactions and Effective Thermal Diffusivity Using Temperature Time Series." *Water Resources Research* 48, no. 11: W11532.

McGlathery, K. J. 2001. "Macroalgal Blooms Contribute to the Decline of Seagrass in Nutrient-Enriched Coastal Waters." *Journal of Phycology* 37, no. 4: 453–456.

Midttømme, E., P. Roaldset, and K. Aagaard. 1998. "Thermal Conductivity of Selected Claystones and Mudstones From England." *Clay Minerals* 33, no. 1: 131–145.

Munz, M., and C. Schmidt. 2017. "Estimation of Vertical Water Fluxes From Temperature Time Series by the Inverse Numerical Computer Program FLUX-BOT." *Hydrological Processes* 31, no. 15: 2713–2724.

Paerl, H. W. 2009. "Controlling Eutrophication Along the Freshwater–Marine Continuum: Dual Nutrient (N and P) Reductions Are Essential." *Estuaries and Coasts* 32, no. 4: 593–601.

Paerl, H. W., and T. G. Otten. 2013. "Harmful Cyanobacterial Blooms: Causes, Consequences, and Controls." *Microbial Ecology* 65, no. 4: 995–1010.

Paytan, A., G. G. Shellenbarger, J. H. Street, et al. 2006. "Submarine Groundwater Discharge: An Important Source of New Inorganic Nitrogen to Coral Reef Ecosystems." *Limnology and Oceanography* 51, no. 1: 343–348.

Rabalais, N. N., R. E. Turner, and W. J. Wiseman. 2002. "Gulf of Mexico Hypoxia, A.K.A. 'the Dead Zone'." *Annual Review of Ecology and Systematics* 33, no. 1: 235–263.

Raissi, M., P. Perdikaris, and G. E. Karniadakis. 2019. "Physics-Informed Neural Networks: A Deep Learning Framework for Solving Forward and Inverse Problems Involving Nonlinear Partial Differential Equations." *Journal of Computational Physics* 378: 686–707.

Rau, G. C., M. S. Andersen, A. M. McCallum, H. Roshan, and R. I. Acworth. 2014. "Heat as a Tracer to Quantify Water Flow in Near-Surface Sediments." *Earth-Science Reviews* 129: 40–58.

Santos, I. R., B. D. Eyre, and M. Huettel. 2012. "The Driving Forces of Porewater and Groundwater Flow in Permeable Coastal Sediments: A Review." *Estuarine, Coastal and Shelf Science* 98: 1–15.

Shanafield, M., C. Hatch, and G. Pohll. 2011. "Uncertainty in Thermal Time Series Analysis Estimates of Streambed Water Flux." *Water Resources Research* 47, no. 3: W03504.

Silbiger, N. J., M. J. Donahue, and K. Lubarsky. 2020. "Submarine Groundwater Discharge Alters Coral Reef Ecosystem Metabolism." *Proceedings of the Royal Society B: Biological Sciences* 287, no. 1941: 20202743.

Slomp, C. P., and P. Van Cappellen. 2004. "Nutrient Inputs to the Coastal Ocean Through Submarine Groundwater Discharge: Controls and Potential Impact." *Journal of Hydrology* 295, no. 1–4: 64–86.

Smith, C. G., R. M. Price, P. W. Swarzenski, and J. C. Stalker. 2016. "The Role of Ocean Tides on Groundwater–Surface Water Exchange in a Mangrove-Dominated Estuary: Shark River Slough, Florida Coastal Everglades, USA." *Estuaries and Coasts* 39, no. 6: 1600–1616.

Sohn, R. A., M. A. Briggs, and D. M. Rey. 2024. "Recent Advances in Vertical Temperature Profiler Instrumentation and Flux Estimation Methods Facilitate Groundwater–Surface Water Exchange Studies in Environments With Strong Discharge Zones." *Journal of Hydrology* 639: 131567.

Sun, Z., H. Du, C. Miao, and Q. Hou. 2023. "A Physics-Informed Neural Network Based Simulation Tool for Reacting Flow With Multicomponent Reactants." *Advances in Engineering Software* 185: 103525.

Taniguchi, M., H. Dulai, K. M. Burnett, et al. 2019. "Submarine Groundwater Discharge: Updates on Its Measurement Techniques, Geophysical Drivers, Magnitudes, and Effects." *Frontiers in Environmental Science* 7: 141.

Teichberg, M., S. Fox, C. Aguila, Y. Olsen, and I. Valiela. 2008. "Macroalgal Responses to Experimental Nutrient Enrichment in Shallow Coastal Waters: Growth, Internal

Nutrient Pools, and Isotopic Signatures." *Marine Ecology Progress Series* 368: 117–126.

Tsabaris, C., V. Zervakis, H. Georga, et al. 2021. "In Situ Characterization Using Natural Radio-Tracers in a Submarine Freshwater Spring, Kiveri, Greece." *Journal of Environmental Radioactivity* 233: 106583.

Valiela, I., J. McClelland, J. Hauxwell, P. J. Behr, D. Hersh, and K. Foreman. 1997. "Macroalgal Blooms in Shallow Estuaries: Controls and Ecophysiological and Ecosystem Consequences." *Limnology and Oceanography* 42, no. 5part2: 1105–1118.

Voss, C. I., and A. M. Provost. 2002. "SUTRA: A model for 2D or 3D saturated-unsaturated, variable-density ground-water flow with solute or energy transport." In Water-Resources Investigations Report 02-4231. U.S. Geological Survey.

Voytek, E. B., A. Drenkelfuss, F. D. Day-Lewis, R. Healy, J. W. Lane, and D. Werkema. 2014. "1DTempPro: Analyzing Temperature Profiles for Groundwater/Surface-Water Exchange." *Groundwater* 52, no. 2: 298–302.

Zhou, Y., A. H. Sawyer, C. H. David, and J. S. Famiglietti. 2019. "Fresh Submarine Groundwater Discharge to the Near-Global Coast." *Geophysical Research Letters* 46, no. 11: 5855–5863.

PART III

Appendix

List of Publications

Munir, M.U., Blaurock, K. & Frei, S. Understanding the vulnerability of surface–groundwater interactions to climate change: insights from a Bavarian Forest headwater catchment. Environ Earth Sci 83, 12 (2024). https://doi.org/10.1007/s12665-023-11314-2

Munir, M.U., Gilfedder, B.S. & Frei, S. Runoff Generation and Groundwater Interactions in a Central European Headwater Catchment: Using Process-Based Modelling and Radon-222 as a Natural Tracer. **Under review**

Frei, S., **Munir, M.U.,** Seiverth, A.M., Gilfedder, B.S., 2026. Using physics-informed neural networks to quantify submarine groundwater discharge under high-frequency tidal dynamics using heat as a tracer. Limnol. Oceanogr. Methods 24, e70015. https://doi.org/10.1002/lom3.70015

(Eidesstattliche) Versicherungen und Erklärungen

(§ 8 Satz 2 Nr. 3 PromO Fakultät)

Hiermit versichere ich eidesstattlich, dass ich die Arbeit selbstständig verfasst und keine anderen als die von mir angegebenen Quellen und Hilfsmittel benutzt habe (vgl. Art. 97 Abs. 1 Satz 8 BayHIG).

(§ 8 Satz 2 Nr. 3 PromO Fakultät)

Hiermit erkläre ich, dass ich die Dissertation nicht bereits zur Erlangung eines akademischen Grades eingereicht habe und dass ich nicht bereits diese oder eine gleichartige Doktorprüfung endgültig nicht bestanden habe.

(§ 8 Satz 2 Nr. 4 PromO Fakultät)

Hiermit erkläre ich, dass ich Hilfe von gewerblichen Promotionsberatern bzw. –vermittlern oder ähnlichen Dienstleistern weder bisher in Anspruch genommen habe noch künftig in Anspruch nehmen werde.

(§ 8 Satz 2 Nr. 7 PromO Fakultät)

Hiermit erkläre ich mein Einverständnis, dass die elektronische Fassung der Dissertation unter Wahrung meiner Urheberrechte und des Datenschutzes einer gesonderten Überprüfung unterzogen werden kann.

(§ 8 Satz 2 Nr. 8 PromO Fakultät)

Hiermit erkläre ich mein Einverständnis, dass bei Verdacht wissenschaftlichen Fehlverhaltens Ermittlungen durch universitätsinterne Organe der wissenschaftlichen Selbstkontrolle stattfinden können.

. . . . . .

Ort, Datum, Unterschrift